

MODEL FOR SUSPENDED GATE FIELD EFFECT TRANSISTORS USED IN
LABORATORY ANIMAL CAGE MONITORING

By

KAREN E. SUPAN

A DISSERTATION PRESENTED TO THE GRADUATE SCHOOL
OF THE UNIVERSITY OF FLORIDA IN PARTIAL FULFILLMENT
OF THE REQUIREMENTS FOR THE DEGREE OF
DOCTOR OF PHILOSOPHY

UNIVERSITY OF FLORIDA

2005

Copyright 2005

by

Karen E. Supan

This document is dedicated to my parents, Mary Jo and Fred Timm.

ACKNOWLEDGMENTS

First, I would like to thank my advisor, Dr. Herbert Ingley, for his constant support and encouragement of this work. From our first meeting, he has been a great mentor to me in engineering, teaching, and life in general. I thank him for the countless words of wisdom he imparted to me. I acknowledge my appreciation to Dr. David Hahn for the generous amount of time he devoted to this project by providing technical assistance on the experimental portion of this project, offering his expertise in a new area to me and for serving on my committee. I also express gratitude to Dr. Sherif Sherif, Dr. Bill Lear, and Dr. Jason Weaver for being committee members and providing guidance in their area of proficiency.

I am grateful to Osman Ahmed of Siemens Building Technology for the inception and financial support for this project. *Danke schön* to Roland Pohle, Peter Gulden, and many others who made the trek across the Atlantic from Siemens Core Technology in Munich, Germany, to collaborate on this project. Special thanks go to Dr. Gus Battles and Mike Cormier from Animal Care Services for opening their facilities for this project and answering many questions along the way.

It is impossible to forget all the friends and colleagues I have met at UF who have made the time here so enjoyable.

Above all, I express thanks to my parents and family for creating an environment where education was a high priority and paving the way for me to follow in their tracks. My deepest gratitude goes to my husband, Brian, for providing encouragement to pursue

this degree. I will be forever indebted to him for the distances he went to help me achieve this accomplishment.

TABLE OF CONTENTS

	<u>Page</u>
ACKNOWLEDGMENTS	iv
LIST OF TABLES	ix
LIST OF FIGURES	x
ABSTRACT	xiii
CHAPTER	
1 BACKGROUND	1
Comparison of Static Isolator Cages to Ventilated Caging Systems	4
The Macroenvironment	7
The Microenvironment	9
Ammonia	10
Carbon Dioxide	14
Other Contaminants	16
Contact Bedding	17
Relative Humidity	19
Ventilation	20
Additional Environmental Factors	21
Previous Environmental Studies	22
Cost Analysis for Current Husbandry Practices	29
Air Sampling Techniques	30
Semiconductors	31
Field Effect Transistors	33
Gas Sensing	35
Summary	40
2 EXPERIMENTAL FACILITIES AND METHODS	42
Experimental Setup	42
Experimental Procedures	48
Carbon Dioxide Sensor	48
Ammonia Sensor	49

3	THEORETICAL MODELING	54
	Gibbs Free Energy	54
	Adsorption	58
	Surface Reaction Rate Expressions	60
	Langmuir Adsorption Isotherm	60
	Dissociative Adsorption	62
	Competitive Adsorption	63
	Proposed Mechanisms	64
	Ammonia and Hydroxide	64
	Ammonia Dissociation	66
	Molecular Adsorption	72
	Reaction Kinetics	74
	Summary	77
4	RESULTS AND DISCUSSION	78
	Drift Tests	78
	Ammonia Sensor Results	79
	Sensor Response and Mechanism	80
	Diffusion	87
	Temperature Effects	89
	Sensor Performance	91
	Gradual ramping tests	94
	Cross-sensitivity to humidity and carbon dioxide	96
	Carbon Dioxide Sensor Results	99
	Summary	104
5	SUMMARY AND CONCLUSIONS	106
	Summary of Results	106
	Ammonia Sensor	106
	Sensor response and mechanism	106
	Performance and feasibility	107
	Carbon Dioxide Sensor	108
	Recommendations	109
	Future Work	110
APPENDIX		
A	ENVIRONMENTAL STUDIES	112
B	DETAILS OF FIELD EFFECT TRANSISTOR	116
C	ANALYSIS OF EXPERIMENTAL UNCERTAINTY	122

LIST OF REFERENCES.....	125
BIOGRAPHICAL SKETCH.....	131

LIST OF TABLES

<u>Table</u>	<u>page</u>
1-1. Recommended space for lab mice	22
1-2. Ammonia concentration levels after seven days in static isolator cages	23
1-3. Gas sampling pumps used in environmental studies	30
2-1. Sensor testing equipment.....	43
2-2. Ammonia and carbon dioxide concentrations	47
2-3. Ammonia concentrations used for ramping tests	50
2-4. Experimental parameters for time response tests	52
3-1. Infrared (IR) and XPS measurements and assignments for adsorbed species of ammonia on surface catalysts.....	66
4-1. Rates of baseline signal drift for the carbon dioxide and ammonia sensor	79
4-2. Curve fit coefficients, R-squared values, and rate constants for desorption and adsorption of 100 ppm ammonia on sensor.	83
4-3. Adsorption and desorption time constants for the ammonia sensor using forced and diffusion flow regimes.	90
4-4. Curve fit coefficients, R-squared values, and rate constants for desorption and adsorption of ammonia on sensor at varying surface temperatures.	91
4-5. Slopes for ramp down and ramp up curves completed in diffusion box.	96
4-6. Magnitude of signal response for changes in ammonia concentration and relative humidity.	98
4-7. Adsorption time constants	104
4-8. Desorption time constants	104

LIST OF FIGURES

<u>Figure</u>	<u>page</u>
1-1. A static microisolator cage	4
1-2. Equipment used to ensure a healthy microenvironment in an animal laboratory	6
1-3. When excited, electrons move from the valence band to the conduction band across the energy gap.	32
1-4. Schematic of field effect transistor.....	34
1-5. Classical FET configuration	35
1-6. Suspended Gate FET configuration.....	35
1-7. Photograph of a hybrid flip chip FET sensor device.....	36
2-1. Schematic of experimental facilities.....	42
2-2. Humidification section of experimental facilities	44
2-3. Mixing section of experimental facilities	44
2-4. Two flow regimes used in sensor testing.....	45
2-5. Carbon dioxide sensor	46
2-6. Signal from DC power supply.....	48
2-7. Graphical depiction of experimental parameters used to test the carbon dioxide sensor for cross-sensitivity to humidity.	49
2-8. Graphical depiction of ammonia concentrations used in ramping tests.	50
2-9. Graphical depiction of experimental parameters used to test the ammonia sensor for cross-sensitivity to humidity while ammonia was present.....	51
2-10. Graphical depiction of experimental parameters used to test the ammonia sensor for cross-sensitivity to humidity and carbon dioxide.....	52

3-1. Diffuse Reflectance Infrared Fourier Transform Spectra (DRIFT-spectra) for a TiN screen-printed film	65
3-2. Mechanism for the reduction of NO by NH ₃ over a V ₂ O ₅ sensing layer in the presence of oxygen.....	65
3-3. The XPS N(1s) core-level spectra for ammonia.....	67
3-4. The XPS N(1s) core-level spectra for ammonia on (a) Si(100)-(2x1) and (b) Si(111)-(7x7)	68
3-5. Surface species and desorption products from ammonia on Si(100)	69
3-6. Ball and stick models for the adsorption geometry for -NH ₂ and -H on two different surfaces.....	70
3-7. The XPS N 1s spectra of Ti/Si (100) surface	71
4-1. Long-term drift test results	79
4-2. Average desorption data and curve fit for 100 ppm desorption tests	82
4-3. Average adsorption data and curve fit for 100 ppm adsorption tests	83
4-4. Actual 50 ppm average (<i>N</i> =5) desorption curve plotted along with the predicted curve	84
4-5. Actual 50 ppm average (<i>N</i> =6) adsorption curve plotted along with the predicted curve.....	85
4-6. The slope of the Gibbs energy changes as the reaction proceeds.....	87
4-7. Diffusion of ammonia in a semi-infinite region.....	88
4-8. Average (<i>N</i> =6) desorption curve for the diffusion case compared with the forced curve fit for 100 ppm data	89
4-9. Average (<i>N</i> =6) adsorption curve for the diffusion case compared with the forced curve fit for 100 ppm data.....	89
4-10. Average desorption and adsorption curves at 50 ppm ammonia for heater voltages of (a) – (b) 2 V (<i>N</i> =10) and (c) – (d) 3 V (<i>N</i> =7 and <i>N</i> =8).....	91
4-11. Single analyte test results (<i>N</i> =1) for the ammonia sensor.....	93
4-12. Calibration curve and linear fit for ammonia sensor	93
4-13. Ammonia concentration ramped up and down with ammonia sensor in diffusion box.....	95

4-14. Ammonia sensor tested for cross-sensitivity to humidity	96
4-15. Ammonia sensor tested for cross-sensitivity to humidity with ammonia in the system.....	97
4-16. Average ($N = 6$) ammonia sensor response to humidity, carbon dioxide, and ammonia concurrently.....	100
4-17. Raw data ($N=1$) from carbon dioxide single analyte test.....	101
4-18. Calibration curve for carbon dioxide sensor.....	101
4-19. The average ($N=4$) response time and respective curve fits of the carbon dioxide sensor.....	103
4-20. Carbon dioxide sensor tested for cross-sensitivity to humidity.....	105
B-1. Schematic section through a hybrid flip chip field effect transistor	116
B-2. Schematic cross-section of a suspended gate field effect transistor	117
B-3. Scanning electron microscope cross-section of a hybrid flip chip field effect transistor	117
B-4. Printed circuit board for the suspended gate field effect transistor.	118
B-5. Schematic for one channel of the suspended gate field effect transistor control board, where the drain to source voltage is indicated by UDS.	119
B-6. Detailed drawing of the suspended gate field effect transistor control board.....	120
B-7. Simple drawing of the suspended gate field effect transistor control board.....	121

Abstract of Dissertation Presented to the Graduate School
of the University of Florida in Partial Fulfillment of the
Requirements for the Degree of Doctor of Philosophy

MODEL FOR SUSPENDED GATE FIELD EFFECT TRANSISTORS USED IN
LABORATORY ANIMAL CAGE MONITORING

By

Karen E. Supan

December 2005

Chair: H.A. Ingley III

Major Department: Mechanical and Aerospace Engineering

Over the past century, great advances in medicine have been achieved through the use of laboratory animals, specifically rodents. The quality of the animal environment is important to the rodent's health and welfare, and their well-being directly affects the quality of research involving their use. There can be significant variability in air quality between cages depending on a number of factors such as population size and air flow. A way to accommodate for the variability between cages is to monitor environmental quality indicators within the cage, such as ammonia, carbon dioxide, temperature, and relative humidity. Since rodent cages are approximately the size of a shoebox, commercially available sensors would be too large for this application. Therefore, micro-sensors, or field effect transistors, were investigated for application in a rodent cage. Since these sensors were on the forefront of technology, a theoretical model was developed for the ammonia sensor to further understand the chemical reaction taking place on its surface.

The sensors were tested in a controlled environment, where the air quality was known. The magnitude and time of the response to different levels of contaminants (e.g., ammonia and carbon dioxide) were determined. The study showed that the sensors can detect changes in air quality in a sufficiently short amount of time (5 minutes) so that corrective action could be taken to prevent the rodents from overexposure to harmful levels of air contaminants. At the present development stage, the sensors used for this investigation will require further improvements before implementation in a laboratory animal cage. These improvements include but are not limited to eliminating drift of baseline signal, increasing sensitivity of sensor, amplifying signal output, and coupling each gas sensor with a humidity sensor.

The reaction mechanism selected for the model which was best supported by the literature and the experiments was molecular adsorption of ammonia on a titanium nitride surface. The experimental results were fitted to the model to obtain the adsorption and desorption rate constants, the equilibrium concentration constant, equilibrium constant, and Gibbs free energy, which respectively were 6.28 L/mol*s , $6.43 \times 10^{-3} \text{ s}^{-1}$, 976.7 L/mol, 39.04, and -9.25 kJ/mol. Based on these values, it was determined that the forward reaction, or adsorption, occurs spontaneously. There was good correlation between the theoretical model and the experimental results, indicating that the theoretical model was sufficient for this application.

CHAPTER 1 BACKGROUND

Nearly every medical breakthrough in the last century has come as a result of research with animals (1). In the nineteenth century, animals contributed to the treatments for rabies, smallpox, and anthrax. The early 1900's saw breakthroughs in cardiac catheterization techniques, treatment for rickets, and the discovery of insulin. In the 1930s research with dogs contributed to the development of modern anesthesia, while horses aided in the prevention of tetanus. The 1940s saw treatment of rheumatoid arthritis and whooping cough, prevention of diphtheria, and development of antibiotics. In the 1950s a cure for polio was found through the use of rabbits, monkeys, and rodents. That decade also saw the development of open-heart surgery, cancer chemotherapy, and tranquilizers. In the past 50 years, animals have helped find treatments for diseases such as rubella, measles, and Hansen's disease. They have also further advanced research on organ transplants, breast cancer, cystic fibrosis, multiple sclerosis, and Lou Gehrig's disease. While much of this research was done with large animals, such as dogs, monkeys, or sheep, today's medical research mainly utilizes rodents.

Mice have been utilized in a wide array of medical research. For example, mice have been used in cancer research since 1894 (2). In 1921 inbred strains, which were susceptible to tumors, were created. More strains were developed in 1929 with the founding of one of the first animal laboratories, Jackson Laboratories. In 1962, a mutant mouse with low immunity was discovered which led to human tumor transplantations.

The late 1980's saw a boom in mice research with the development of a transgenic mouse whose genes were altered to produce a desired characteristic. From this research, oncogenes, a gene that can cause a normal cell to become cancerous, could then be studied. Genetically engineered mice are also used today to determine Vitamin C's role in health and illness (3). Today, research is ongoing in such diverse areas as diabetes, hearing loss, ovarian cancer, and glaucoma (4).

Mice are valuable for medical research because of their genetic similarity to humans (1). Laboratory mice, *Mus domesticus*, belong to the family *Muridae* and are a domesticated variant of the house mouse, *Mus musculus* (5). Adult mice are adapted to live in groups and generally live no longer than two years. They typically weigh 20-40 grams (0.7-1.4 ounces), have a length of 12-15 centimeters (5-6 inches), and when standing on hind legs achieve a height of 10-12 centimeters (4-5 inches).

The quality of the environment is imperative to the rodent's health and welfare, and their well-being directly affects the quality of research collected from them (5). Rodent cages have evolved over the years to better suit the needs of the animals.

Lisbeth Kraft, in the late 1950's, was the first to separate mice into isolator cages to prevent the spread of communicable diseases through direct contact, specifically epidemic diarrhea of infant mice (6).

Filter-top covers were added to Kraft's isolator system to prevent the transmission of airborne diseases as well as to eliminate the exchange of feces, soiled bedding, and hair between adjacent cages (7). Robert Sedlacek developed the modern filter top while working with a large gnotobiotic mouse colony used in radiation biology research at Massachusetts General Hospital. The filter top was a polycarbonate frame fitted with a

polyester filter medium held in place by a perforated aluminum plate. The rim at the bottom of the filter top, where it fit over the underlying cage, formed a lip. One of the first static isolator cages consisted of a cylindrical cage with a solid galvanized bottom and a tight-fitting lid with metal mesh sides wrapped with fiberglass insulation that filtered the incoming air. The contemporary static isolator caging system has given institutions the ability to keep rodents “clean” while housing contaminated and clean rodents simultaneously (6).

Further improvements were made to the static isolator cages with the onset of ventilated caging systems (VCS). These systems were developed to improve intracage ventilation and to increase housing capacity. The first ventilated cages were developed under the direction of Dr. Ed Les at Jackson Laboratories in 1960, around the same time as the filter-top cages. The earliest version deposited mouse odors and allergens out into the room. Jackson Laboratories and Thoren Caging Systems collaborated to further improve upon this design in the late 1970s by filtering the incoming and exhaust air. The first systems were commercially available in the early 1980s. By the early 1990s VCS had gained widespread popularity (6). Meanwhile, other companies such as Hazelton Systems were developing a ventilated rack system to help reduce allergies of staff members (8). In Hazelton’s system, air was blown into each shelf row of cages or each individual cage at a low velocity and removed by a main exhaust system.

In a modern VCS, high efficiency particulate arresting (HEPA) filtered air is blown into cages through a manifold under positive-pressure. Air is either exhausted directly from the cage or filtered before sending it to the room or venting outside (9).

In addition to the VCS, HEPA filtered flow work areas were developed for use when changing the bedding or restocking food and water in a cage. The work area helps maintain the microbial barrier created by the static isolator cage and VCS. Ambient air is drawn into the station, moved through a pre-filter and HEPA filter, and is then blown horizontally or vertically across the workstation.

Comparison of Static Isolator Cages to Ventilated Caging Systems

Static microisolator cages are still used in many animal laboratories. Isolator cages are cost effective and allow containment at the cage level without expensive ventilation (10). They are a proven technology for protecting valuable mice from microbial contamination (5). Isolator caging systems provide a separate microenvironment and aid in the development and upkeep of disease-free rodents for use in research. Static cages are useful for studies where containment at the cage level is desirable, for example, in vivo administration of hazardous agents (6). Photographs of static microisolator cages are depicted in Figure 1-1.



Figure 1-1 A static microisolator cage (a) side view and (b) top view.

While static cages may be cost effective, there are drawbacks that must be considered. The use of these cages can be labor intensive depending on how often the

bedding is changed. Changing and handling of the cages is physically intensive potentially leading to back or hand injuries. Due to frequent cage changing a large supply of bedding is required. The cages must be washed frequently which uses a significant amount of water and electricity and can accelerate the degradation of the cage (9).

The static cages in use today are advantageous because they are durable, transparent, and have a replaceable filter top and tight-fitting lid, which is not easy to dislodge (11). When the filter top was first introduced, the advantage of containment outweighed the effects on the air quality inside the cage. Research soon revealed that the filter top was a barrier to air and moisture exchange increasing the intracage relative humidity in one study by 38% compared to the macroenvironmental humidity (6). The filter top impedes air exchange between the micro and macro environments. The only ventilation in static cages comes from the rodents breathing patterns (8).

Individually ventilated caging systems (IVCS) have addressed the problem of little to no air exchange between the micro and macro environments. The IVCS combines the static cages with individual ventilation. The whole package, as depicted in Figure 1-2, should include a microisolation cage, ventilated cage rack, and a Class 100 or Class II change cabinet, which helps rodents remain disease-free in a healthy microenvironment (5).

Microenvironmental air quality is better and the variability in air quality between cages is reduced when using ventilated cages. Intracage ammonia, carbon dioxide, and relative humidity are also lower. In addition, the day on which ammonia is first detected can be delayed (6, 12, 13). One study revealed that direct ventilation, 23 air changes per

hour (ACPH) to each cage, improved the microenvironmental conditions in comparison with a static isolator cage. The relative humidity, ammonia, and carbon dioxide in the ventilated cages were 8% lower, 240 parts per million (ppm) lower, and 2900 ppm lower, respectively (11). Ventilated systems also help prevent mouse urinary protein (MUP) from spreading. A study showed that less than 0.05 ng/m^3 (5×10^{-7} ppb) was detected in a room with IVCS, whereas a high level, 4.6 ng/m^3 (4.6×10^{-6} ppb), of MUP was measured when mice were housed in open cages (14).



(a)



(b)

Figure 1-2 Equipment used to ensure a healthy microenvironment in an animal laboratory should include (a) a cage changing station and (b) a ventilated cage rack.

Operational savings can also be achieved with IVCS. With the improved air quality, cage changing can be delayed to weekly or longer, which translates into labor savings. The time spent sanitizing cages and the quantity of bedding used are reduced as well. Due to the decreased cage changing intervals the service life of the cages and caging systems is increased. The stocking density per room can be increased, thereby

allowing more efficient use of space in a laboratory animal facility (6). Overall, an improved microenvironment leads to lower operational costs.

Despite the improvements in micro and macro environmental air quality and savings in operational costs, IVCS are not used in every laboratory animal facility. To begin with, IVCS are expensive to acquire. Despite the advantages of IVCS, a new system is decidedly capital intensive (6). Other costs accrue from electricity for operating the system, maintenance, and replacement of filters. The IVCS are also more difficult to sanitize than a standard rack holding isolator cages. Blowers, shelves, and access panels must be removed before placing the IVCS in a rack washer. Extensive washing by hand is required and access to all plenums and ducts may not be feasible. The heat gain in the housing room may be increased due to the supply and exhaust blowers. If stocking density is increased the heat gain due to the mice will rise causing an increase in the total cooling load. Noise generation from the IVCS exhaust and supply blowers may be an issue for employees working in the room and mice in the microenvironment. Finally, excess intracage ventilation can cause chilling and dehydration, especially with neonates and hairless mutants. Whichever system a laboratory animal facility chooses to use, the most important issue is the health and welfare of the animals and laboratory personnel.

The Macroenvironment

To better meet the needs of the animals and personnel, the environment in which they work or reside must be examined. The overall facility or building is known as the megaenvironment, the items in an animal's room are considered the macroenvironment, and the items in an animal's cage or immediate surroundings are the microenvironment (15). Each environment can be treated separately, but the couplings between each system

must also be considered. For example, a high-level exhaust system can improve thermal ventilation efficiency for the mega and macro environments. This high-level exhaust system may not provide enough circulation to properly ventilate the individual static isolator cages and thereby does nothing to decrease the ammonia and carbon dioxide concentrations in the microenvironment (6). Therefore improvements for the macroenvironment will not necessarily improve the microenvironment.

One of the main reasons laboratory animal facilities are concerned with the condition of the macroenvironment is for laboratory animal personnel. According to the National Institute for Occupational Safety and Health (NIOSH), 33% of animal handlers have allergic symptoms and 10% have symptoms of animal-induced asthma (5). Laboratory workers can have laboratory animal allergies (LAA) to prealbumin and albumin, which are derived from mouse urine and skin (16). Aeroallergens from mice are highest during cage changing, while handling male mice on an unventilated table, and while dumping the bedding from the cage without a dumping station.

A study by Sagakuchi et al. (16) revealed that using female mice, filter-top covers, and corncob bedding could reduce LAA. Prealbumin and albumin levels were reduced by 90% and 40%, respectively, when using female mice versus male mice. Using a filter-top cover rather than no cover reduced prealbumin by 90% and albumin by 60%. When wood shavings were replaced by corncob bedding prealbumin dropped 57% and albumin by 77%. Other studies have shown that using IVCS and carrying out animal husbandry and research procedures in ventilated cabinets can reduce exposure to aeroallergens (5).

A healthy macroenvironment is imperative for the overall facility. The environmental conditions in the cage and room directly affect how an animal will

respond to laboratory procedures (17). Apposite housing and management are critical to animal welfare, the quality of research data and teaching or testing programs where animals are used, and the health and safety of employees (18).

The Microenvironment

The microenvironment should meet the various needs of the mice. First, the primary enclosure should allow for normal physiological and behavioral needs of the animals. These include allowing for maintenance of proper body temperature, urination, defecation, normal movement, and postural adjustments. The cage should be large enough so that the mouse can turn around and make typical movements. Second, the primary enclosure should allow for social interaction and hierarchical development. In addition, the cage should provide a clean, dry, safe area with adequate food, water, and ventilation. Lastly, the personnel should be able to view the animal with minimal disturbance (15). Taking into account all of these measures can help ensure a healthy microenvironment.

The microenvironment's condition has been observed scrupulously due to the advent of the filter-top. Before the filter-top, observations of the macroenvironment were sufficient to maintain the health and well-being of the animals. In today's animal facility it is inadequate to supply the macroenvironment with 15 ACPH, keep the temperature and relative humidity at the recommended levels, and then completely disregard the conditions in the microenvironment (11). This is because air exchange occurs at the junction of the lid with the cage and not through the filter medium. A study by Keller et al. showed that the lid reduced the air exchange rates within the cages to one ACPH while the room was ventilated at 12 ACPH (19).

With such an airtight environment the cage can easily become contaminated. There are four major environmental quality indicators within the cage. The first is ammonia, which is produced from the urea found in the animal's excrement. Second is carbon dioxide, which is generated as a metabolic waste product. Third is moisture, indicated by relative humidity, from respiration, excrement, and the drinking water for the mice. Additionally, thermal loads from metabolic activity can contribute to a rise in cage temperature (11). In general, ammonia, carbon dioxide, relative humidity, and temperature are used to assess the microenvironmental conditions.

The level of air quality is dependent on a number of factors, which include but are not limited to population size, strain and stock of animal, location of a cage on the rack, type of filter, airflow within the room, and relative humidity (12). Lipman identifies four ways to address poor microenvironmental air quality (6):

1. Change cages at sufficient frequencies.
2. Use contact bedding with desirable performance characteristics.
3. Reduce the macroenvironmental relative humidity.
4. Increase the macroenvironmental temperature (dry-bulb) without altering the moisture content in the air.

Choi et al. determined that restricting the number of animals per cage, regularly changing soiled bedding, and increasing ventilation were techniques to prevent relative humidity and concentrations of carbon dioxide and ammonia from increasing in static cages (12).

Ammonia

The build-up of intracage ammonia concentrations is the primary reason for ventilating a microisolation cage (5). Above a certain moisture threshold the urease-positive bacteria grows, leading to ammonia production (15). The moisture threshold is

dependent on the type of bedding used, for example, pine shavings, recycled pulp, or corncob bedding.

Enteric bacteria produce ammonia through two possible mechanisms of enzymatic activity. In the first mechanism, bacterial urease acts as a catalyst for the hydrolysis of urea to ammonia and carbamate:



For the second mechanism, D- and L-amino acid oxidases remove the amino group from amino acids to form keto acid and ammonia (12).

Ammonia levels. The human ammonia threshold limit value (TLV) used by NIOSH of 25 ppm was established through the work of Gamble and Clough (20). A TLV is the concentration to which humans can be exposed to for 8 hours a day 5 days a week without any harmful effects (21). The Occupational Health and Safety Administration (OSHA) standards for ammonia are 50-ppm time-weighted average (TWA) and 35-ppm short-term exposure. The human TLV is accepted for animals, although for mice the concentration capable of reducing respiratory rate by 50% (RD₅₀) is approximately 300 ppm (22).

Effects of ammonia. Ammonia acts as an irritant and can alter or destroy the tracheal epithelium. More specifically, when the epithelium becomes irritated, the cilia are paralyzed, mucus flow is altered, and the surface layers of the epithelial lining are destroyed (20). The epithelial thickness also changes, which increases the airflow and deposition of airborne particles to that area (21). The abnormal increase in the tracheal epithelium is dependent on the amount of ammonia and how long the animals are exposed to it.

Gamble and Clough documented the effects of ammonia on the rat tracheal epithelium (20). After four days of exposure at 200 ± 50 ppm, there was a transitional-stratified appearance to the epithelium and irregularities were noticeable. Some gross changes were noted after eight days; the cilia disappeared, stratification increased, folds formed on the surface of the lumen, and the amount of mucus increased. At twelve days of exposure, the epithelial thickness increased and there was an acute inflammatory reaction with increased cellularity and alteration of cell types.

Few studies showing long-term effects on mice exposed to ammonia exist and the amount, which causes harmful effects, seems to vary for different studies done on rats. For example, rats exposed to ammonia at 180 ppm for 90 days did not show any problems, while in other studies a level greater than 25 ppm promoted growth of infective agents in the respiratory tract (5).

Coon et al. completed rat inhalation studies on ammonia for both repeated and continuous exposure (23). Repeated exposure (30 repeated exposures, 8 hours/day, 5 days/week) to 0.155 ppm of ammonia produced no adverse effects. At 0.770 ppm of repeated exposure there were nonspecific inflammatory changes in the lungs of rats. Under continuous 90-day exposure, 0.040 ppm led again to nonspecific inflammatory changes in the lungs. At 0.127 and 0.262 ppm the same changes were seen in the kidneys and lungs. At 0.455 ppm, 32 of 51 rats died by day 25 of exposure and 50 by day 65, when the experiment was terminated. The rats showed mild signs of dyspnea and nasal irritation. At 0.479 ppm, 13 of 15 rats died and the following conditions were found:

- Focal or diffuse interstitial pneumonitis
- Calcification of renal tubular and bronchial epithelia
- Proliferation of renal tubular epithelium
- Myocardial fibrosis and fatty changes of liver plate cells

Ammonia can also be harmful for rats that already have a weakened immune system. For example, Broderson et al. found that ammonia plays an important role in increasing natural murine respiratory mycoplasmosis (MRM) in rats infected with *Mycoplasma pulmonis* (24).

Despite the limited number of studies of chronic exposure on mice, ammonia has been monitored in experiments where other parameters were the independent variable. In an early experiment, ammonia concentrations were 400% higher in a cage with a punched lid than one with a wire mesh lid (21). White and Mans (25) found that at low ammonia concentrations in their experiments, there was little to no systemic accumulation of environmental ammonia in the animals. After four days of exposure with an ammonia concentration greater than 200 ppm, histological changes in the respiratory tract were visible. Ammonia levels greater than 500 ppm were considered lethal. Choi et al. (12) investigated the effect of population size on intracage ammonia levels and did not detect ammonia in the ventilated cages for the duration of the study, 32 days.

According to NIOSH, mice exposed to ammonia for 6 hours/day for 5 days showed signs of nasal lesions including hypertrophy, hyperplasia, epithelial erosion, ulceration, and necrosis (22).

Ammonia production. The production of ammonia is affected by a number of factors (21, 25):

- Number of animals in a cage
- Frequency of bedding changes
- Ambient temperature
- Relative humidity
- Time of day
- Type of caging
- Ventilation rate and air flow

Improving cage-washing procedures and animal room cleanliness can reduce the concentrations of ammonia producing bacteria. Choosing a different strain of mice can also help reduce ammonia concentration, as the formation of ammonia is strain dependent. Using female mice instead of males can also lower ammonia levels. One study showed that males produce noticeably more ammonia than females when housed on vermiculite, pulp, and pine shaving beddings (21).

Carbon Dioxide

Carbon dioxide is a metabolic byproduct of respiration and is generally used as a metric to determine whether there is enough fresh air in a conditioned space. The carbon dioxide concentration in atmospheric air is roughly 300 to 350 ppm, so comparably low levels are not harmful (26). The activity level of animals, population density, and air exchange rate with the macroenvironment influence formation and accumulation of carbon dioxide (12).

Carbon dioxide generation. A 25 g (0.88 oz) resting mouse consumes 1.65 ml (0.06 fluid oz.) of oxygen per gram of bodyweight per hour and converts 1 ml (0.06 in³) of oxygen to 1 ml of carbon dioxide. Five 30 g (1.05 oz.) mice housed in a filter-topped Type II cage, 350 cm² (54 in²) and 19 cm (7.5 in) high, generated 250 ml (15.26 in³), approximately 37,000 ppm, if unventilated or undiluted, in one hour (27). In a study by Krohn and Hansen (26), mice housed in a static filter top cage with a stocking density of 20 g/L stabilized at a carbon dioxide level of 5000 ppm after two hours. They also measured carbon dioxide concentrations in IVCS cages without ventilation. The level reached values between 20,000 and 80,000 ppm within two hours.

Carbon dioxide recommended levels. There are currently no official limits for acceptable exposure of rodents to carbon dioxide. The guideline for humans of 5000

ppm is applied most often to rodents (26). However, since rodents are adapted to live in tunnels where carbon dioxide levels can reach 14,000 ppm, higher values have been investigated (5). It is recommended that intracage carbon dioxide for IVCS and static cages not exceed 5,000 and 30,000 ppm, respectively (5). Lipman states that carbon dioxide levels can be up to 4,000 ppm higher than those observed in the macroenvironment when housing the maximum number of mice (6). It is also advised that if animals are exposed to a level above 15,000 ppm, which is significantly higher than the atmosphere, they should be used for experimental purpose with caution and allowed a few days of recovery after exposure (27). Levels less than 30,000 are acceptable for studies involving physiological or biochemical parameters, while when between 30,000-50,000 ppm animals should be given ample time to recover. Exposures greater than 50,000 ppm should not be accepted because the impact on the animals may be harmful and irreversible (26).

Carbon dioxide effects. The reaction of animals exposed to carbon dioxide mimics a stress reaction, with elevated serum corticosterone levels, increased respiration, reduced numbers of eosinophils and lymphocytes, and a fight-or-flight reaction along with the release of adrenaline. Humans exposed to less than 10,000 ppm showed only minor effects, which then normalized after 10-15 days. Animals and humans exposed to higher concentrations, 10,000-15,000 ppm, experienced the stress reaction described above. Rodents exposed to levels greater than 30,000 ppm had elevated respiration rates and high levels of circulating corticosterone, indicating physiological and hormonal changes (27).

Other Contaminants

Ammonia and carbon dioxide are only two of many contaminants in laboratory animal cages. Other contaminants found in cages include acetic acid, sulfur dioxide, formaldehyde, dimethylamine, ethanol, ethylene glycol, methane, and hydrogen sulfide. Experiments have found uncharacterized air contaminants in isolator cages (6).

Acetic acid. Perkins and Lipman in their comparison study of bedding materials, detected acetic acid (mean = 0.86 ppm) in static isolator cages with and without mice containing corncob bedding (10). Acetic acid was off-gassed, presumably from the decay of vegetative material related with the corncob bedding, rather than from bacteria associated with the mice (6).

Acetic acid, while not always present in static cages, has a low threshold limit value. The permissible exposure limit was set by OSHA for acetic acid at 10 ppm for an 8-hour TWA. A 10 ppm 8-hr TWA was also set by NIOSH, as well as a 15 ppm short-term exposure limit (15 minutes). Exposure can occur through inhalation, ingestion, eye or skin contact, and absorption through the skin. The vapors cause eye, skin, mucous membrane, and upper respiratory tract irritation. Mice exposed to 1,000 ppm of acetic acid vapor had eye and upper respiratory irritation (28). Decreased lung mechanics were observed in guinea pigs exposed to 5 to 500 ppm of airborne acetic acid for one hour (10).

Sulfur dioxide. Perkins and Lipman found sulfur dioxide (mean = 0.42 ppm) in static isolator cages, but only in the presence of mice and corncob bedding (9). The OSHA standard for sulfur dioxide is 5 ppm averaged over an 8-hour work shift, while NIOSH recommends that the limit be reduced to 0.5 ppm for the TWA for up to a 10-hour work shift for a 40-hour week (29). Sulfur dioxide can affect the body if it is

inhaled or comes in contact with the eyes or skin. As a gas it is a severe irritant of eyes, mucous membranes, and skin. It rapidly forms sulfurous acid on contact with moist membranes (16).

Other contaminants. Mild inflammatory changes, primarily in the lungs, were noted when rats were exposed continuously to formaldehyde (0.0046 ppm), dimethylamine (0.009 ppm), and ethanol (0.086 ppm). When exposed repeatedly to ethylene glycol at 0.010 and 0.057 ppm no changes were seen. After 8 days of continuous exposure to 0.012 ppm of ethylene glycol, two out of fifteen rats suffered corneal damage with apparent blindness (23). Methane and hydrogen sulfide concentrations were evaluated in static isolator cages. Methane levels were greater than 500 ppm after seven days, while no increase in hydrogen sulfide was detected. The physiological relevance and effects of these two gases on mice are still unclear (6).

The aforementioned contaminants are a sampling of what could be present in a laboratory animal housing environment. The presence of any one of these contaminants is dependent on the combination of factors such as type of bedding, cage type, and strain of mice. A well-monitored cage is a key step to ensure a healthy and safe environment for all involved.

Contact Bedding

Bedding in animal cages is a controllable environmental parameter, which can influence animal welfare and research data (18). Beddings should be chemically and biologically inert, contaminant free, highly absorptive, nontoxic, dust-free, compatible with the research study, easily disposable, and inexpensive (10,15). Additionally, the ideal contact bedding should enhance the physical and psychological well-being of the animal, while not influencing it biologically (21).

Bedding materials produce environmental pollutants, such as ammonia. Ammonia production is influenced by the following properties of bedding: particle size, absorption properties, and the presence of urease or a urease activator. The particle size plays an important role in desiccating fecal pellets and thus reducing ammonia production.

Potgieter and Wilke state that because large particles have a larger exposure area they may dry faster (21). Smaller particles, however, have greater surface to volume ratio and it seems they would dry faster. Urease, an enzyme that catalyzes the hydrolysis of urea, is widely distributed in plants, which are the source for most bedding materials (21).

Ammonia build-up in cages can be controlled by the frequency of bedding changes, as the two are inversely related (21). The Guide for the Care and Use of Laboratory Animals, henceforth referred to as The Guide, recommends that soiled bedding should be removed as often as is necessary to keep animals clean and dry. The frequency and intensity of cleaning and disinfection should depend on what is needed to provide a healthy environment for an animal (18).

The kind of contact bedding chosen can affect air contaminants such as ammonia (18). Common contact beddings include recycled paper, ground corncob, cellulose, and wood chips. Perkins and Lipman evaluated several contact beddings in static isolator caging, with 15 room ACPH, and four mice per cage (10). The beddings in the study were ranked from lowest to highest mean ammonia concentration as follows:

- Corncob
- Virgin cellulose pelleted
- Recycled paper
- Hardwood chip
- Virgin pulp loose
- Reclaimed wood pulp
- Pine shavings
- Aspen shavings

Corncob proved to be the best bedding under these conditions as no ammonia was detected after seven days of exposure. Corncob bedding is among the most popular beddings currently used.

Relative Humidity

Relative humidity is the ratio of the partial pressure of water vapor, p_v , in a given moist air sample to the partial pressure in a saturated moist air sample, p_g , at the same temperature and total pressure,

$$\phi = \frac{p_v}{p_g} \Big|_{T,p} . \quad (1.2)$$

At room temperature, 25°C (77°F), the pressure of saturated water vapor is 3.2 kPa (0.5 psi).

Monitoring relative humidity is another way to help control the microenvironment. Higher macroenvironmental relative humidity leads to higher intracage relative humidity, which increases ammonia production within the cage (10, 30). The Guide recommends a relative humidity range from 30-70% (18).

A relative humidity threshold has been found where above this level ammonia production is independent of contact bedding. The threshold, however, varies with contact bedding (30). For example, when the macroenvironmental relative humidity was greater than 70%, the ammonia generation curve for a static isolator cage was similar between pine shavings and corncob bedding. When the relative humidity was reduced to 60% the slope of the corncob reduced to zero for seven days while there was no change in the pine shavings curve (6). Potgieter and Wilke discovered in their experiments that

when relative humidity and temperature reached 50% and 21°C (70°F) ammonia production increased (21).

Ventilation

An average mouse (25-30 g) inhales approximately 35 liters (45 g) of air in a 24-hour period, which is more than the total weight of its food and water. The quality, quantity, and distribution of air are more directly associated with the animal's health, comfort, and overall well-being than other environmental factors (7). In addition, air associated pollutants can negatively affect the animals quality of life and general welfare (21).

The Guide states that the purpose of ventilation is to (18):

- Supply adequate oxygen
- Remove thermal loads caused by animal respiration, lights, and equipment
- Dilute gas and particulate contaminants
- Adjust moisture content of room and cage air
- Create static-pressure differential between adjoining spaces

Ten to fifteen fresh ACPH are recommended for secondary enclosures and have been the standard for many years. This guideline does not take into account possible heat loads, species, size, number of animals, type of bedding or frequency of cage changing, room dimensions, or efficiency of air distribution (18).

For individually ventilated cages, cage air change rates should be adjustable from 30 to 100 ACPH depending on the number of mice and changing frequency. The air velocity at the inlet to the cage should be less than 15 m/min. (50 ft/min.), which is consistent with still air. This reduces the risk of high-velocity air-cooling and dehydration of cage occupants (5).

Reeb et al. (31) studied the impact of room ventilation rates on microenvironmental parameters for static isolator cages. The study found that the microenvironment maintained adequate levels of ammonia, carbon dioxide, and relative humidity at low (5 ACPH) room ventilation rates. They also discovered that increasing the room ventilation rate had minimal effect on intracage ventilation except for cages on the highest row just below the fresh air supply. Increased room ventilation did, however, decrease the humidity in the room and cages. For example, with 5 room ACPH the relative humidity was at 50%, but dropped to 22% as the room ACPH increased to 20.

Ventilation rate can be an important factor for controlling environmental ammonia concentration. However, studies indicate that changes in ammonia concentration and ventilation rate are not linear. White and Mans (25) found that the mean ammonia concentration in unventilated cages did not vary in direct proportion to the room air exchange rate. In a study by Besch (32), doubling and tripling the room ventilation rate did not produce proportional decreases in ammonia concentration. Serrano also found that increasing the ventilation rate did not proportionally decrease the ammonia concentration (7). The lack of linearity is most likely correlated to physical limitations placed on air motion patterns within a room, which is a function of the type of air diffusion system and the face velocity of air from the diffuser at varying room air exchange rates (25).

Additional Environmental Factors

In addition to the environmental factors previously described there are a few others, which create a suitable living environment for mice. These include temperature, cage space, noise, and light levels.

Temperature. Since rodents are warm-blooded animals, they must maintain their body temperature within normal variation for their overall well-being (18).

Recommended dry-bulb temperatures for mice are 18-26°C (64-79°F). The cage temperature may be higher than the macroenvironment due to animal heat load, heat transferred from fan motors, and inefficient cage ventilation rates (5).

Cage space. The recommended cage space for lab mice as defined by the Guide is listed in Table 1-1. Solid-bottom caging, with bedding is suggested as it is preferred by rodents (18). It is important to follow the recommended space guidelines as the number of animals in a cage positively influences ammonia production, carbon dioxide levels, temperature, and relative humidity (12, 21).

Table 1-1 Recommended space for lab mice

Weight, g	Floor Area/Animal, in ²	Height, in.
<10	6	5
Up to 15	8	5
Up to 25	12	5
>25	>15	5

Noise and light levels. The control of noise and light levels is primarily for the comfort of the mice. Mice can hear frequencies ranging from 80 to 100 kHz, but are most sensitive to 15 to 20 kHz and 50 kHz. They hear high frequency and ultrasound, which is why intracage ultrasound should be minimized. Mice have adapted to low light levels of approximately 40-60 lux (3.7-5.6 candles). In comparison, ordinary office lighting is less than 500 lux (46 candles) (5).

Previous Environmental Studies

There are many factors that contribute to the animal's environment as depicted in the previous section; and different combinations offer varying results. For example, one combination of contact bedding, bedding change frequency, and ventilation rate may

provide a suitable environment, while altering one of those factors may allow ammonia production to occur earlier. The following is a review of previous environmental studies illustrating the numerous combinations that have been tried to improve the animals' environment.

Ammonia concentrations in filter-top cages. Serrano (7) was influential in the evolution of the modern cage with his study on static isolator cage types in 1971. Through his study he determined the effect of different types of covers on the distribution of gases in cages with varying population sizes. Four types of filter tops were used: fiberglass, molded laminated polyester, and two types of steel-wire mesh (40 by 40 and 20 by 20). In one experiment, eight mice were housed per cage with corncob bedding and contaminant gas levels were measured after seven days. Carbon dioxide concentration levels were less than 4000 ppm for all types of filter tops. For the polyester type filter, which is similar to present day filter tops, the mean concentration on the seventh day for cages with 4, 8, and 16 mice were <2 , 21 ± 18 , and 90 ± 28 ppm, respectively. Ammonia concentrations varied significantly from cage to cage as seen in Table 1-2 with the 40 by 40 mesh having the highest concentration.

Table 1-2 Ammonia concentration levels after seven days in static isolator cages

Filter Top	[NH ₃] (ppm)
Fiberglass	63 ± 33
Molded Laminated Polyester	21 ± 18
40 by 40 Mesh	177 ± 64
20 by 20 Mesh	35 ± 35

Comparison between macro- and microenvironment. Murakami (17) in 1971, compared the environment within the cage to the ambient air. He found that changes in temperature and relative humidity within the cage paralleled changes in the ambient air,

with negligible difference between the internal and external temperature. Relative humidity and ammonia concentrations, however, were notably higher than in the room.

Decreases in room relative humidity. Lipman (11) conducted an environmental study on filter-top cages, specifically Sedlacek-type. First, microenvironmental parameters were measured while the room was held constant at 50% relative humidity. Then, the room relative humidity was decreased to 20% and the same parameters were measured.

Below 50% relative humidity, the cage relative humidity was 20% higher, ammonia concentrations were 150 ppm higher, and carbon dioxide concentrations were 2300 ppm higher than in a cage without a lid. Ammonia was detected in the cages on day 4. When the room relative humidity was decreased to 20%, there was a 15% decrease in cage humidity, the mean weekly relative humidity was 58%, and ammonia was less than 20 ppm and not detected until day 7.

Static isolator cages and strains of mice. Hasenau et al. (33) compared four different static isolator cages for microenvironmental temperature, relative humidity, and ammonia concentrations. Three cages had polycarbonate bases and lids with Reemay 2024 filter material, while the fourth was used as a control without a filter. Comparisons were made of BALB/c and CD-1 same sex mice at four and two per cage under varying microenvironmental conditions. The following parameters were used in the study:

Room ACPH:	20
Room Temp:	22.8±1.7°C (standard RH) 24.1±0.7°C (<40% RH)
Relative Humidity:	51.5±8.2% (standard) 22.7±7.7% (below normal)
Bedding:	Autoclaved hardwood bedding
Bedding Change Frequency:	Every 7-9 days

Under standard relative humidity (40-70%) conditions in the macroenvironment, the relative humidity in the filter-top cages, each housing 4 mice, ranged from 17-28% higher than the room levels. At below normal relative humidity (<40%) levels, the cage humidity ranged from 25-38% higher than the room.

Ammonia concentrations varied significantly between strains of mice and cage types. In the first study, where 4 BALB/c mice per cage were utilized, all cages accumulated less than 5 ppm by day 9. With two mice per cage the concentrations dropped to less than 3 ppm on day 9. When the CD-1 mice were housed 4 per cage under standard relative humidity levels, ammonia concentrations after 8 days ranged from 1.9 ppm (control) to 117.1 ppm. The ammonia levels dropped significantly for all cages when the macroenvironmental relative humidity dropped to below 40%; ammonia levels varied from 0.1 to 8.7 ppm. At a stocking density of two mice per cage, all cages had an ammonia concentration of less than 5 ppm at day 8.

In conclusion, Hasenau et al. (33) determined a number of factors that could be altered to improve the environment. They found that reducing the macroenvironmental relative humidity reduced the ammonia production in the cages. Also, reducing the stocking density from 4 to 2 mice decreased ammonia levels more than decreasing the room relative humidity. There was also a significant difference in ammonia levels depending on the strain of mice.

Population size and cage type. Choi et al. (12) studied the effect of population size on the buildup of ammonia and relative humidity in static and ventilated cages over time. The pressurized individually ventilated cages received 50-60 ACPH, while the room received 15 ACPH.

Environmental parameters varied between the static and individually ventilated cages. Ammonia levels were less than 1 ppm throughout the 32-day study for the individually ventilated cages housing both 2 and 4 mice. Relative humidity increased slightly with the number of mice. In the static cages, no ammonia was detected in cages with 1 or 2 mice after 8 days. The relative humidity increased with the number of mice, which in turn increased the ammonia levels. Levels with 3 and 4 mice were 5.5 ppm after 8 days. For all the cages, the corncob bedding appeared dry throughout the study and there were no wet areas in one spot, indicating that the mice did not have one spot to urinate.

Comparison of contact beddings. Potgieter and Wilke (21) investigated three different contact beddings for dust content, dust generation, moisture absorption properties, and ammonia production. The contact beddings: vermiculite, pine shavings, and unbleached eucalyptus pulp were chosen because they were readily available in South Africa, the location of the study. The room was kept at $24.7 \pm 1.1^\circ\text{C}$ (76.5°F) and $51.3 \pm 5.3\%$ RH and received eight ACPH. One hundred forty-four adult inbred conventional BALB/c mice were divided among the three bedding types and housed in static isolator breeding cages that were changed weekly.

Ammonia concentrations were surprisingly low throughout the study and never exceeded 3.5 ppm. The lowest ammonia level (≤ 1 ppm) measured on day 7 was from the eucalyptus pulp. Potgieter and Wilke (21) do not recommend using the vermiculite as contact bedding due to the quantity of dust it produced. They advise using the eucalyptus pulp due to its moisture absorption properties and low levels of ammonia and dust.

IVCS and absorbent bedding. Huerkamp and Lehner (9) characterized and compared microenvironments of three IVCS and a static isolator cage with ammonia-inhibiting contact bedding to a standard static isolator cage containing corncob bedding. The cage ACPH for the three IVCS were 74, 106, and 112, respectively. Each IVCS was changed every 14 days, while the static cages were changed weekly. The room was held constant at $22.4 \pm 0.3^{\circ}\text{C}$ (72°F) and $42 \pm 6\%$ relative humidity with 15 ACPH.

With the use of five and ten percent of the absorbent bedding in the static isolator cages, the ammonia detection was delayed by one day. However, over the course of six days the ammonia production was not altered. Ammonia was not detected in the three IVCS after seven days and after 14 days the levels were still low. Conversely, ammonia was detected after four days in the static cages and exceeded 100 ppm after seven days. Carbon dioxide was reduced in the IVCS (1050 – 1650 ppm) compared to an average of 2050 ppm in the static cages. Methane was detected in all cages at an excess of 500 ppm, while hydrogen sulfide was not detected.

Comparison of individually ventilated cages. Hoglund and Renström (34) evaluated two different IVCS (BioZone VentiRack and Tecniplast Sealsafe) for ammonia concentrations after two weeks, carbon dioxide build-up during a one-hour simulated power failure, and the ability to maintain a positive or negative pressure differential for long periods of time. Male mice, 10 weeks old, were used in the study, housed three per cage. Aspen wood shavings were used for the contact bedding. The room was held at $22 \pm 1^{\circ}\text{C}$ (71.6°F) and $55 \pm 5\%$ RH and received 17 ACPH.

The VentiRack from BioZone provided a more uniform and balanced differential pressure, but the systems exhibited similar behavior in all other areas. Under either the

negative or positive pressure differential the ammonia content in the cages was less than 10 ppm after 10 days when the bedding was not soaked. If the bedding was soaked, the ammonia concentration remained high regardless of the ventilation rate.

Carbon dioxide did not build up to harmful concentration levels in the one-hour simulated power failure due to the filter-top cages that were used with the IVCS.

Ventilation and frequency of bedding changes. Reeb et al. (13) evaluated the microenvironment in pressurized individually ventilated (PIV) cages under two different conditions: varying cage air change rates and reduced frequency of bedding changes. Cage ventilation rates were held constant for 1 week at 30, 40, 60, 80, and 100 ACPH. Bedding was not changed for 26 days. Two groups of mice were evaluated: 9-11 week old males and trio groups for mating with pups less than 14 days old. The bedding was autoclaved white pine shavings. The microenvironmental parameters measured were temperature, relative humidity, ammonia, and carbon dioxide.

The results from increased cage ventilation show that the environment improves with more circulation. Ammonia and carbon dioxide decreased significantly with increased ventilation rates. For all ventilation rates the ammonia level was less than 3 ppm. Relative humidity was significantly higher at 30 and 40 ACPH, while it was not significantly different for 60, 80, and 100 ACPH. For less than 60 ACPH the temperature was $25.0 \pm 0.02^\circ\text{C}$ and dropped significantly at 80 ACPH to 23.3°C .

Higher ventilation rates could reduce frequency of bedding changes to once every two weeks. Mean ammonia concentrations stayed low for 21 days and increased to 12 ppm between days 21 and 26. The relative humidity was highest at day 21 (45%) and

decreased by day 26. Carbon dioxide and temperature fluctuated, but did not increase in relation to the number of days with soiled bedding.

In a similar study, Reeb-Whitaker et al. (35) compared three different cage-changing frequencies (7, 14, and 21 days) at three different cage ACPH (30, 60, and 100). Twelve breeding pairs and twelve breeding trios were evaluated for general health over seven months. Pressurized individually ventilated cages with white pine shavings were used to house the mice. Ammonia was greater than 25 ppm at 30 ACPH at all frequencies of bedding changes and at 60 ACPH after 21 days. The pup mortality rate was higher when cages were changed every seven days. Reduced frequency of cage changes had no effect on the following health areas: weanling weight, animal growth, plasma corticosterone concentrations (important for carbohydrate and protein metabolism), immune function, breeder mortality, and breeder productivity.

It is evident that many environmental studies have been done which combine a wide range of environmental parameters. Appendix A includes a comprehensive matrix classified by the dependent variables in each study.

Cost Analysis for Current Husbandry Practices

Besides maintaining a healthy environment, many of the previous studies were driven by economics. One of the major cost savings areas is the frequency of bedding changes. For example, at the University of Florida Animal Care Services static microisolator cages are changed twice a week and not autoclaved, which translates into \$116 per cage per year. Agrawal (36) recommends decreasing the frequency from 3.5 days to 7 days and autoclaving the bedding, which will reduce the cost to \$76, a savings of \$40 per cage per year. Likewise for individually ventilated cages, if the bedding change frequency can be extended from 14 to 21 days a cost savings of \$16 per cage per

year could be realized. Considering the Animal Care Services current housing needs, \$100,300 could be saved per year.

With real-time monitoring of cages, the bedding change frequency could be reduced and savings realized without compromising the health and welfare of the animals and laboratory personnel. The goal of this work was to explore the possibilities of continuous monitoring of laboratory animal cages through the use of field effect transistors.

Air Sampling Techniques

Presently, there is no standardized sampling method for rodent aeroallergens nor is there a uniform procedure for measuring and quantifying rodent allergen exposure in rooms with IVCS systems (5). Current husbandry practices rely on environmental measurements taken in studies and regulated by the Guide (18) to control aeroallergens. Environmental measurements in studies were typically taken with a gas-sampling pump as seen in Table 1-3. While these sampling pumps have low measurement error, $\pm 2.5\%$ (35), sampling is often done on an infrequent basis due to cost and time restraints. For example, in one study measurements were taken three times between 1:00 pm and 5:00 pm on days 6, 13, and 20 of a 21-day cage changing cycle. Both experiments and husbandry practice would benefit through continuous or more frequent monitoring of cages.

Table 1-3 Gas sampling pumps used in environmental studies

Type	Manufacturer	Reference
Gas Analyzer, Model 1302 and 1303	Brüel and Kjær	(35)
Aspirating Pump #8014-400A	Matheson Gas Products	(12)
Multi Gas Detector	Dräger	(21)
Toxic Gas Monitor, Model SC-9	Riken Keiki	(34)

One way to provide continuous monitoring in an animal cage is through low-power miniaturized gas sensors offered as field effect transistors (FET). For background purposes, the following section includes general information on semiconductor properties, field effect transistors, and surface reactions between sensing films and ammonia or carbon dioxide.

Semiconductors

In general FETs operate on the principle of electrical manipulation of fields. The field manipulation is controlled by a gate, which acts on the conduction of carriers in a semiconductor channel (37).

Semiconductors are materials consisting of elements from group IV of the periodic table with electrical properties lying somewhere between insulating and conducting materials. Conducting material is characterized by a large number of conduction band electrons that have a weak bond with the basic structure of the material. Therefore an electric field easily transmits energy to the outer electrons and allows the flow of electric current (38).

Semiconductors act as conductors when the electrons possess enough energy to exceed the energy gap, E_g , between the valence band, the energy level filled by electrons in their lowest energy state, and conduction band, the unfilled energy level into which electrons can be excited to provide conductivity as seen in Figure 1-3 (39).

Semiconductors have a lattice structure, which is characterized by covalent bonding. Whenever a free electron leaves the lattice structure, it creates a positive charge or hole. Electrons move to fill the holes, consequently creating more holes. When voltage is applied electrons move towards the positive band, while holes shift towards the

negative band. The movement of electrons and holes conducts current. The number of electron-hole pairs determines the conductivity according to the following relationship,

$$\sigma = n_e q \mu_e + n_h q \mu_h, \quad (1.3)$$

where n_e and n_h are the number of electrons in the conduction and valence bands, respectively, μ_e and μ_h are the mobility of electrons and holes, respectively, and q is the charge (39).

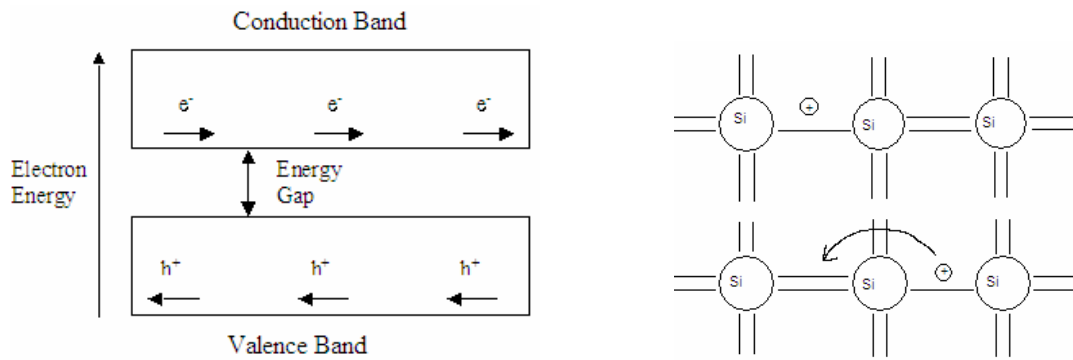


Figure 1-3 When excited, electrons move from the valence band to the conduction band across the energy gap.

The number of charge carriers in semiconductors is controlled by temperature. At absolute zero, all the electrons are in the valence band, while the conduction band is empty. As the temperature increases it is more likely that an energy level in the conduction band will be occupied. The number of electrons in the conduction band is equal to the number of holes in the valence band and is related to temperature, T by

$$n = n_e = n_h = n_o \exp\left(\frac{-E_g}{2kT}\right) \quad (1.4)$$

where k is Boltzmann's constant and n_o is a constant (39).

If the voltage source or exciting energy is removed, the holes and electrons will recombine over a period of time, designated as,

$$n = n_o \exp\left(\frac{-t}{\tau}\right) \quad (1.5)$$

where t is the time after the field is removed and τ is a constant known as the recombination time (39).

The behavior of an intrinsic semiconductor cannot be accurately controlled due to its sensitivity to slight variations in temperature. Therefore adding impurities or dopants that determine the number of charge carriers can create an extrinsic semiconductor. An n-type has an extra electron that lowers the energy level, whereas a p-type does not have enough electrons and a hole is created (39).

Field Effect Transistors

A transistor is a three-terminal semiconductor device, which performs two functions: amplification and switching (38). Transistors have three connections, where the voltage on (current into/out of) switch has the effect of controlling the ease with which current can flow between the other two terminals (40). The effect is to make a resistance whose value can be altered by the input signal. The patterns of signal fluctuation can be transferred from a small input signal to a larger output signal. Specifically for a metal oxide semiconductor-FET (MOSFET), there are three terminals: gate, drain, and source (Figure 1-4). The gate is a metal film layer that is separated from the bulk by a thin oxide layer. When a voltage is applied to the gate an electric field is created which repels positive charge carriers away from the surface of the bulk in which the negative charge carriers dominate and are available for conduction. By increasing the gate voltage, the depth of the channel can subsequently be increased.

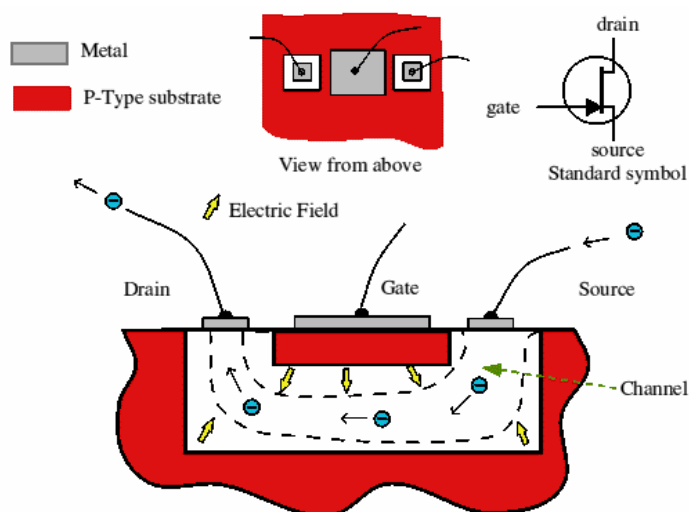


Figure 1-4 Schematic of field effect transistor (FET) (40).

Upon gas exposure, the surface of the sensing film registers a work function change^a, which is seen electronically as a gas sensitive potential. This potential is then added to the gate voltage and operates the transistor (41).

There are two basic types of FETs used in gas sensing: a classical FET and a suspended gate FET (SGFET) or hybrid flip-chip FET (HFCFET). In the classical FET the sensing layer lies directly on the gate surface, whereas in the SGFET the sensing film is separated from the gate surface by an air gap (Figure 1-5 and Figure 1-6). In order to ensure adequate capacitive coupling the air gap must be no larger than a few micrometers, but at least one micrometer to allow for sufficient gas diffusion through the channel. There must be no contact between the sensitive material and channel-insulating layer (41).

An FET consists of two parts: an alumina substrate that contains the conducting structures for the flip-chip contacts and a sensitive layer on a separate electrode (Figure

^a The smallest amount of energy, measured in electron volts, required to remove an electron from the boundary of an element.

1-7). The sensor film is applied to a designated area using a freely selectable deposition process. If a heater element is needed, it is on the backside of the alumina substrate. For an HFCFET the etching steps in thin-film technology ensure that a defined air gap for gas diffusion is formed when the FET is mounted. An advantage of using an air gap is that the same substrate design can be used for all types of transducers because the geometry does not change (41, 42). Additional schematics and detailed electrical drawings can be found in Appendix B.

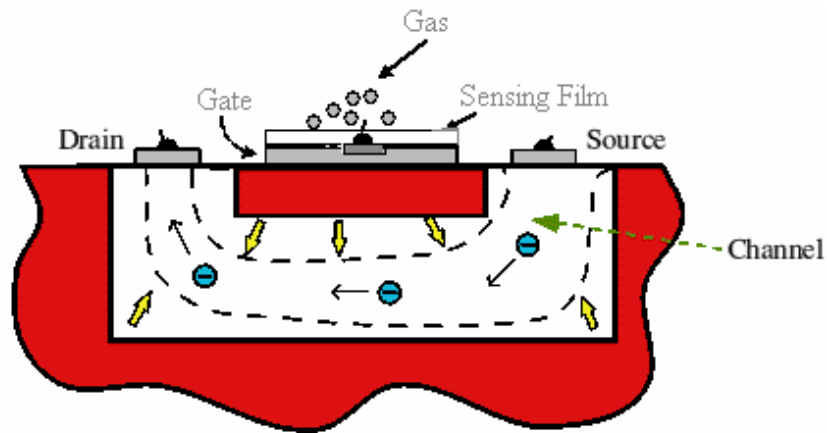


Figure 1-5 Classical FET configuration where the sensing film lies in the same plane as the gate.

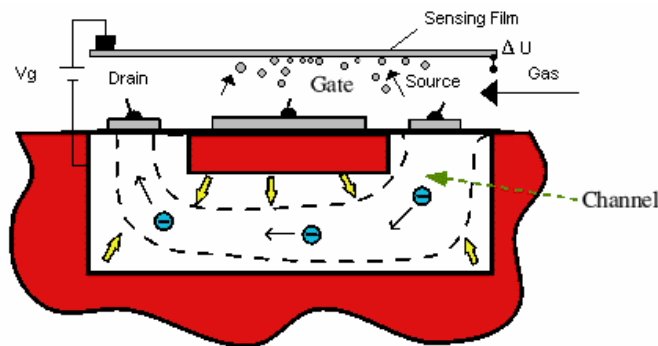


Figure 1-6 Suspended Gate FET configuration where the sensing film is separated from the gate by an air gap.

Gas Sensing

Field effect transistors can be used to detect a wide variety of gases by choosing the sensing layer that reacts with or catalyzes the specific gas. The reaction mechanism,

adsorption, and desorption rates will vary for each combination and creates a challenge to the designer to find the best combination.

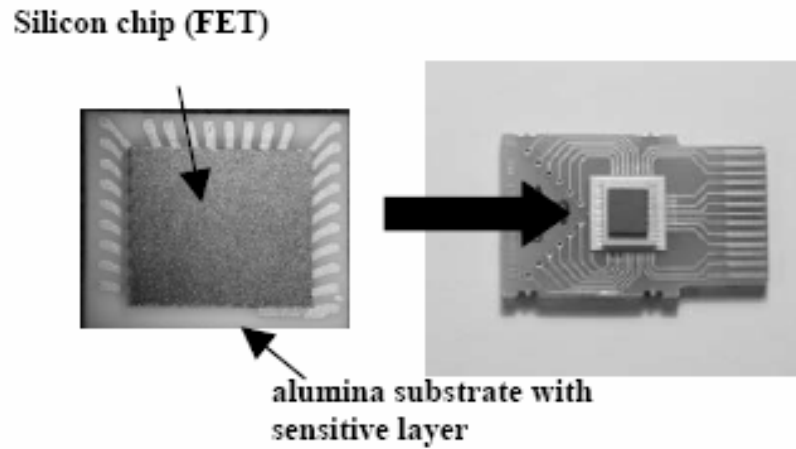


Figure 1-7 Photograph of a hybrid flip chip FET sensor device (left) mounted on a printed circuit board (right). (Data of Simon et al. (46))

Hydrogen detection is the most basic reaction and aids in understanding more complex reactions involved with ammonia and carbon dioxide sensing. For sensing of hydrogen the reaction occurs in three steps. First, the hydrogen molecules dissociate on the catalytic metal surface of the device. Secondly, the hydrogen atoms are transported through the metal film. Lastly, adsorption of hydrogen occurs at the interfacial layer between the metal and insulator where a dipole layer forms. The adsorbed hydrogen disrupts the electric fields across the device structure and is detected through changes of the electrical characteristics of the device (43).

Ammonia reactions. For ammonia detection, one surface that is used is titanium nitride (TiN). Ostrick et al. (44) claim that water and ammonia adsorb on the TiN film and change the work function of the film. The TiN surface is covered with hydroxide (OH) and water and upon exposure to ammonia the OH species is reduced and compounds related to ammonia are formed. Two reaction mechanisms are possible for

ammonia adsorption. In the first, the ammonia removes OH from its binding site. The second mechanism proposes that the OH groups become binding sites for the ammonia, as seen here



The change of the work function, $\Delta\Phi$, is due to the difference of dipoles on the surface of OH and ONH₄, given by,

$$\Delta\Phi \sim (d_{ONH_4} - d_{OH})\Theta \quad (1.7)$$

where Θ is the coverage of ONH₄ and d is the dipole moment (44).

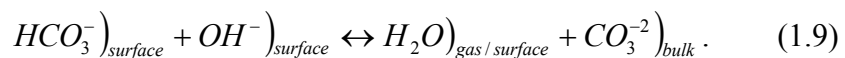
Ostrick et al. (44) found that the reaction of ammonia on TiN occurred reversibly at room temperature and was not hindered by pre-adsorption. No cross sensitivities to the following gases were found: carbon monoxide (30 ppm), carbon dioxide (3000 ppm), nitrogen dioxide (1 ppm), hydrogen (10 ppm), methanol (10 ppm), and acetone (10 ppm).

Sensitivity to ammonia was found to be independent of relative humidity (5-80%). At room temperature ammonia solves almost completely in water under formation of NH₄⁺ and OH⁻ ions. Since the ammonia concentration is low (<100 ppm) compared with the surface water concentration (>5000 ppm), all of the ammonia reacts with the water. In the next reaction step, the ammonia ions may react directly with the surface or with adsorbed hydroxide ions. Due to the excess of water molecules, the found ammonia sensitivity may be independent of the water concentration. At higher temperatures, however, the sensitivity to ammonia decreases. The solubility of ammonia in water decreases at higher temperatures as well as the amount of water on the surface. The amount of ammonia on the TiN surface is also reduced, therefore the ammonia is less likely to react with adsorption sites and the sensitivity decreases.

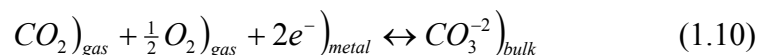
A reaction mechanism proposed for ammonia detection in metal-insulator-semiconductor (MIS) field effect devices is that adsorbed NH_4^+ is detected on the oxide surface in the holes and cracks of the metal film. Another proposed mechanism is that ammonia dissociates on the catalytic surface and reacts similarly to hydrogen. The SGFET and MIS devices differ in that, for an SGFET the response results from adsorption of the detectable species on the surface, whereas in an MIS it occurs by adsorption in the interface between metal and oxide. Results from Abom et al. (43) imply that when a porous TiN film is used for an SGFET, no NH_3 response is seen. Even when the surface is covered with NH_4^+ , the molecules cannot reach the reactant surface SiO_2 and produce a response. However, it was found that NH_3 is dissociated if Pt is present and the resulting atomic hydrogen can be detected.

Carbon dioxide reactions. Ostrick et al. (45) outlined the temperature dependent reaction mechanisms for barium carbonate (BaCO_3) as the sensing film used to detect CO_2 . At 50°C the reaction of CO_2 is dependent on water and occurs only if water is present, yet it is independent of the partial pressure of oxygen. When the temperature increases, above 200°C , the reaction is more complicated and is dependent on oxygen and humidity.

The reaction mechanisms at low temperatures are predicted as follows,



At high temperatures, for CO_2 in O_2 as the dry carrier gas, the reaction of formation of the carbonate appears as,



which results in an electromotive force (emf) change of

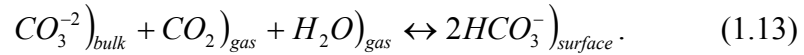
$$E = E_o + k_B T / 2e \ln(p_{CO_2}) + k_B T / 4e \ln(p_{O_2}) \quad (1.11)$$

where k is the reaction rate constant, e is the elementary charge, and p_i is partial pressure.

In terms of work function change, the reaction appears as,

$$\Delta\Phi = \Delta\Phi_o + S_{CO_2} \log(p_{CO_2}) + S_{O_2} \log(p_{O_2}) \quad (1.12)$$

where S is the sensitivity. When humidity is present, the sensitivity to oxygen is reduced and another reaction dominates, possibly the formation of hydrogen carbonate from carbonate, carbon dioxide, and water,



The work function equation for this reaction is

$$\Delta\Phi = \Delta\Phi_o + S_{CO_2} \log(p_{CO_2}) + S_{H_2O} \log(p_{H_2O}) \cdot \quad (1.14)$$

Another surface layer used to detect CO₂ is barium titanate (BaTiO₃) (46). This compound can exist with a low excess quantity of barium. The excess of barium is not compensated by Ti- or O- vacancies or by forming low amounts of a new barium titanate phase with a higher stoichiometry of barium. A mixture of BaTiO₃ with CuO has been reported as a highly sensitive material for CO₂ sensing using the capacitance change in a temperature range of 200-1000°C. Kelvin probe measurements of BaTiO₃ indicate that it has a fast response time, less than one minute, and a sufficient sensitivity to CO₂ (20 mV/decade). Similar to the BaCO₃ surface, the sensitivity of CO₂ is dependent on the presence of humidity. The sensor showed significant cross-sensitivity to NO₂ and drift effects tended to increase.

Ostrick et al. (47) also investigated the different reactions occurring in a multi-layer system, Pt/NiO/BaCO₃, used to detect CO₂. It was found that besides the CO₂

reaction, a separate reaction to NO_2 could occur at the NiO interface. Inserting inert metal oxide layers stopped this reaction.

Summary

As developed in this chapter, there is an evident need for continuous environmental monitoring in laboratory animal cages. By continuously monitoring the cages, laboratory animal personnel can determine when a cage needs to be changed so that the mice are disrupted only when necessary. Prolonged cage changing intervals also translate into labor savings for the animal care facility. Through real-time monitoring, individually ventilated cages can be properly ventilated; increased ventilation during active times and reduced ventilation if the mice are inactive and air contaminant levels are low. Field effect transistors provide a way to achieve continuous monitoring of ammonia, carbon dioxide, temperature, and relative humidity in a laboratory animal cage. Most imperatively, continuous monitoring can provide a better environment for the animals and laboratory personnel.

As a prelude to the following chapters, the goals of this project were to:

- Assess feasibility of applying field effect transistors for monitoring laboratory animal cages through the following tests
 - Single analyte in air
 - Time-response
 - Cross-contamination
- Theoretically model the chemical kinetics and catalysis between the sensing film and contaminant gases and more specifically,
 - Define reaction mechanisms
 - Determine adsorption and desorption rates
 - Find position of chemical equilibrium

- Determine equilibrium constants
- Explore the role of diffusion

CHAPTER 2 EXPERIMENTAL FACILITIES AND METHODS

The purpose of the experimental portion of this study was to assess the feasibility of applying field effect transistors for monitoring microenvironments in laboratory animal cages used in animal research facilities; specifically the work focused on ammonia and carbon dioxide sensors.

Experimental Setup

The experimental facilities included humidification, mixing, and sensor-testing regions as seen in the schematic in Figure 2-1.

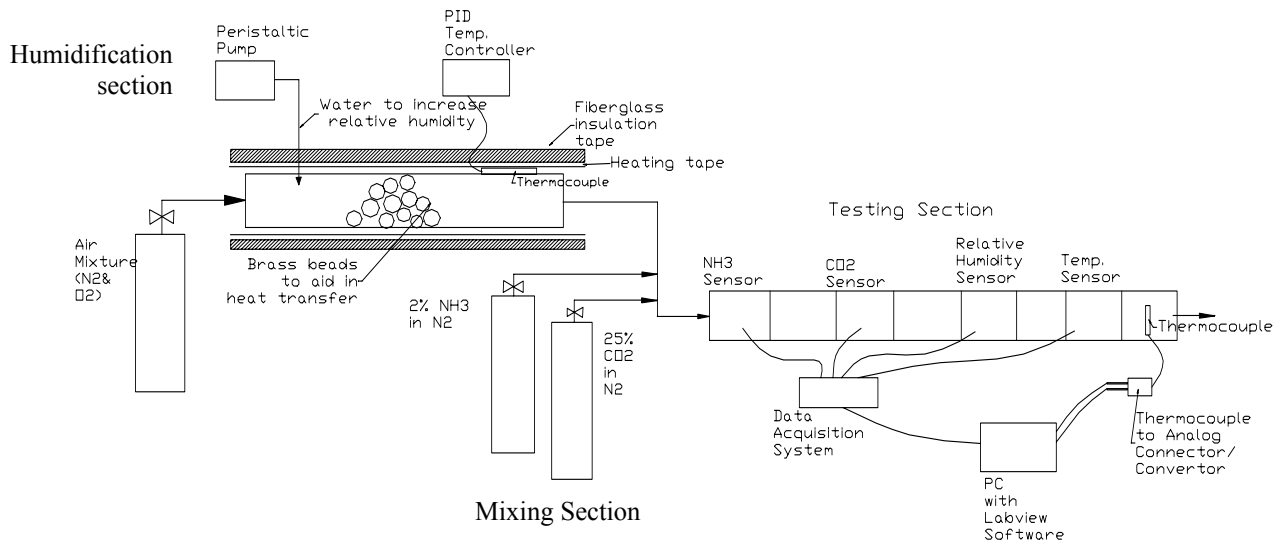


Figure 2-1 Schematic of experimental facilities, which included a mixing, humidification, and sensor-testing region.

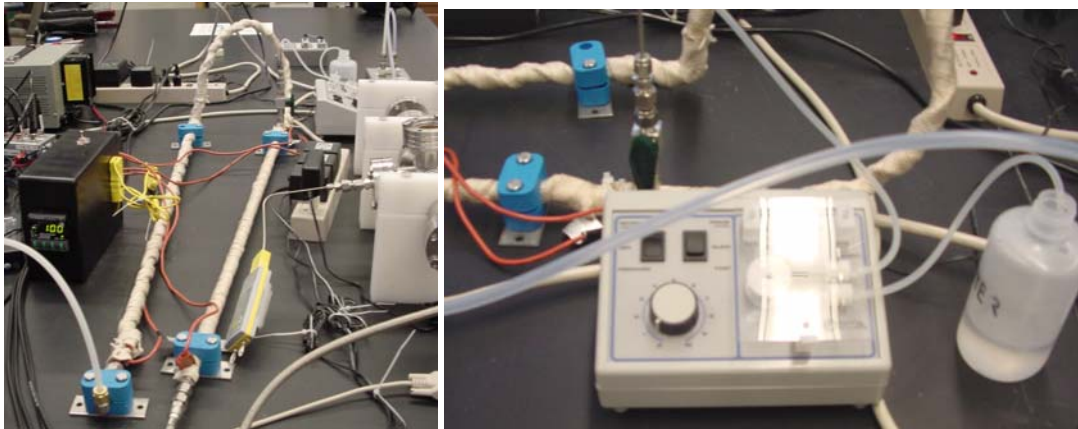
In general, the desired gas mixture (e.g., air, ammonia, carbon dioxide, and water vapor) was prepared by mixing the desired gases (see Table 2-1 for stock gas) and then passing through the test chamber. Table 2-1 provides a comprehensive list of the equipment for the experiments. If humidification was necessary, compressed synthetic

air (Praxair) was preheated to 100°C, and then water was added through a variable flow pump (Fisher Scientific, Model No. 13-876-4), pictured in Figure 2-2. Once humidified, ammonia or carbon dioxide (Praxair) was added to the air system through flow controllers (Alicat Scientific, MC Series) as pictured in Figure 2-3.

Table 2-1 Sensor testing equipment

Sensor Testing Equipment	Manufacturer	Part No.
Vacuum Piping	-----	-----
Flow meters	Alicat Scientific	-----
Fiberglass Cloth Tape Insulation	Fisher Scientific	01-472A
Variable Flow Peristaltic Pump	Fisher Scientific	13-876-4
Laptop	Gateway	-----
Data Acquisition System	National Instruments	NIDAQPad-6020E
Labview Software	National Instruments	Labview 7.1
Controller	Omega	CN1A-TC-24V
Handheld Thermometer	Omega	HH-26K
Heating Tape, 1/2"x4'	Omega	SRT-051-040
Heating Tape, 1/2"x6'	Omega	SRT-051-060
Multimeter	Omega	HHM-11
T/C TO ANALOG CONVERTER, "K"	Omega	SMCJ-K
Type K Connector	Omega	OST-K-MF
Type-K ex. Wire, 100'	Omega	EXPP-K-20-100
Type-K Probe	Omega	KQIN-116G-12
2% Ammonia in Nitrogen	Praxair	-----
75% Nitrogen, 25% Carbon Dioxide	Praxair	-----
Synthetic Air	Praxair	-----
DC Power Supply	Protek	303

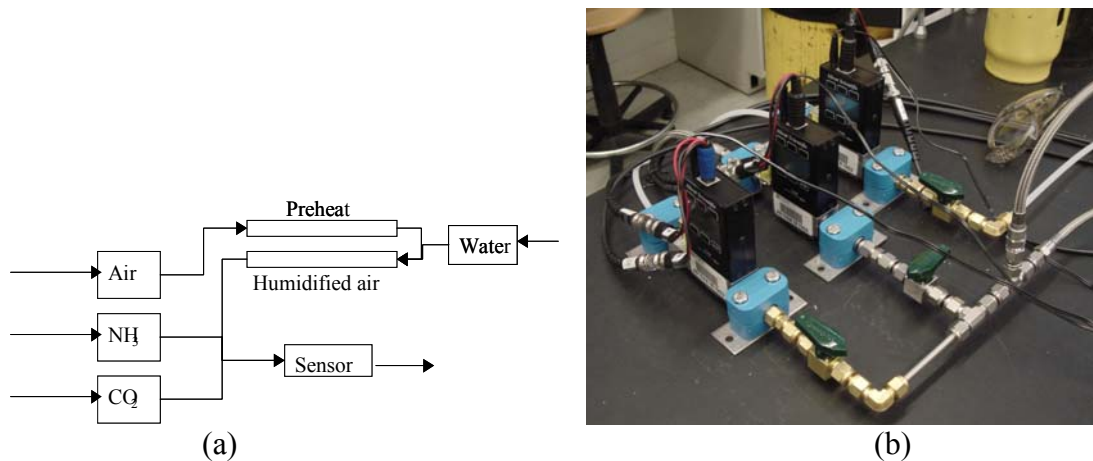
The combined gas stream flowed either directly over the sensor, Figure 2-4a, or into a Plexiglas box, Figure 2-4b. The Plexiglas box was used to simulate cage conditions where diffusion would be the main mode of mass transfer to the sensor. When the gas stream flowed directly over the sensor, the flow rate was limited to between 1 to 2 L/min as specified by the sensor developers. Higher flow rates could induce baseline drift and add noise to the signal. At a flow rate of 2 L/min the Reynolds number was 460, which indicates the flow was laminar.



(a)

(b)

Figure 2-2 Humidification section of experimental facilities: (a) PID temperature controller heats the air before and after adding water, (b) Variable flow pump adds water to the air stream.



(a)

(b)

Figure 2-3 Mixing section of experimental facilities: (a) Schematic of mixing section (b) Flow meters used to control flow rate of air, ammonia, and carbon dioxide

In the diffusion case, the relevant flow rates for the calibration gases were determined based on the air exchange rates and velocity of air leaving an individually ventilated mouse cage. In a typical cage, air enters the cage through a small tube and exits the cage by way of a small gap between the lid and cage bottom. The flow rate calculations were based on the following cage parameters:

Cage air changes per hour	60
Volume of cage	7.067 L (431.25 in ³)

Cage width	12.7 cm (5 in.)
Gap opening	1.27 cm (0.5 in.)
Area of gap	16.1 cm ² (2.5 in ²)

$$V_{cage} = \frac{Q}{A} = \frac{7.067 L/min}{16.129 cm^2} = 4.38 m/min \quad (2.1)$$

where Q is the volumetric flow rate, A is the cross-sectional area, and V_{cage} is the velocity of air leaving the cage.

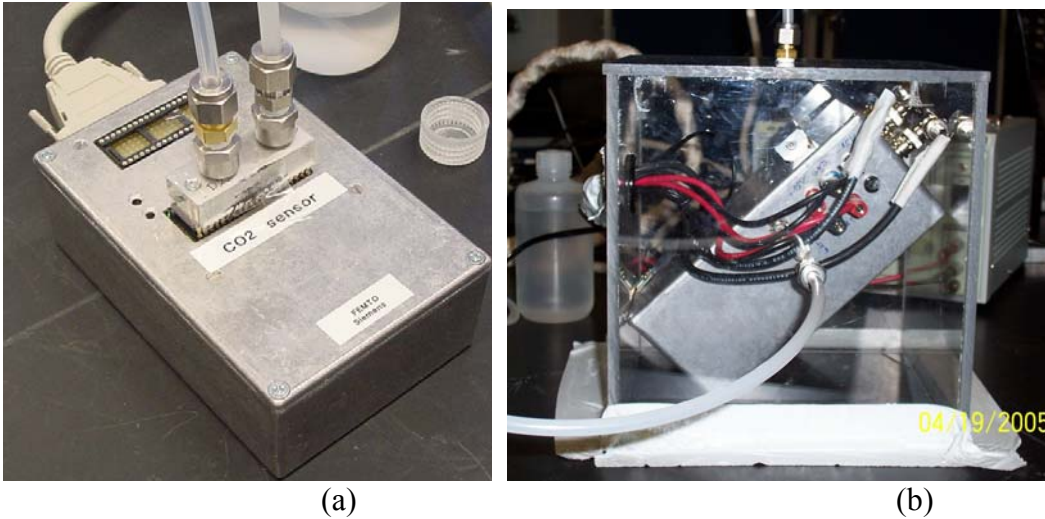


Figure 2-4 Two flow regimes used in sensor testing: (a) Gas stream flowed directly over the sensor or (b) Gas stream diffused onto the sensor mounted in a Plexiglas box used to simulate the cage environment.

The volumetric flow rate in the test section was calculated based on the velocity of air leaving the cage. With a cross-sectional area of 9.62 cm² (1.5 in²) the volumetric flow rate was calculated as follows,

$$Q_{gas} = 9.62 cm^2 \times 4.38 \frac{m}{min} = 4.21 L/min . \quad (2.2)$$

In keeping with this value, the air flow rate was set to 5 L/min in the diffusion test section. The stock ammonia and carbon dioxide were suspended in nitrogen with concentrations of 2% and 25% by volume, respectively (see Table 2-1). The ammonia and carbon dioxide streams were then diluted to the desired concentrations by the pure air

stream. The desired analyte concentration was entered into a Labview program (National Instruments (2004) Labview 7.1), which subsequently calculated the necessary flow rates and used analog output channels to control the flow controllers (Alicat Scientific). The accuracy specification for the flow controllers was $\pm 1\%$ of the full scale, where the full scales for the air, ammonia, and carbon dioxide controllers were 5 L/min, 50 cc/min, and 100 cc/min, respectively. The accuracy for the compressed gas cylinders was $\pm 2\%$ and $\pm 1.25\%$ for the ammonia and carbon dioxide cylinders, respectively. The uncertainty associated with the ammonia and carbon dioxide concentrations for each experimental condition is listed in Table 2-2. Detailed uncertainty calculations can be found in Appendix C.

The actual sensor was on a micro-scale as depicted in Figure 2-5. For ease of use in the laboratory, the sensor was mounted on a larger box housing the electrical connections, as shown in Figure 2-4b. In actual field operation, the sensor would be mounted in a cage with wireless feedback to the electrical board. To prevent the signal from drifting, the surface of the sensor was heated by means of an internal heater. The internal heater was powered by voltage from an external regulated DC power supply (Protek, Model No. 303).

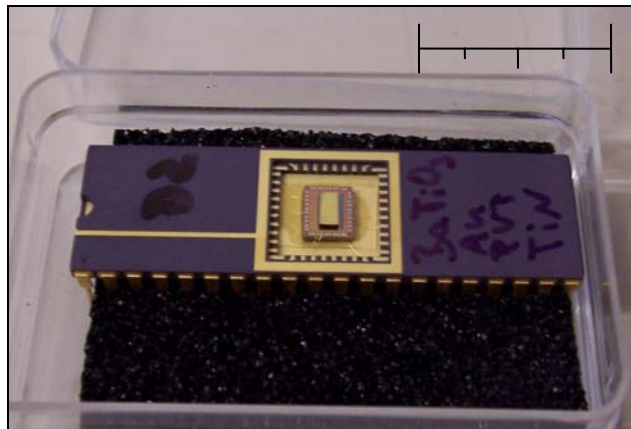


Figure 2-5 Carbon dioxide sensor. (Scale bar = 1 inch (2.54 cm)).

Table 2-2 Ammonia and carbon dioxide concentrations and their associated uncertainties for each experimental condition.

Flow regime	Air flow rate (L/min)	NH ₃ conc. (ppm)	NH ₃ uncertainty (±%)	CO ₂ conc. (ppm)	CO ₂ uncertainty (±%)
Diffusion	5	5	40.0		
	5	10	20.1		
	5	15	13.5		
	5	20	10.2		
	5	25	8.3		
	5	30	7.0		
	5	40	5.5		
	5	50	4.6		
	5	75	3.5		
	5	100	3.0		
	5	150	2.6		
	5	200	2.4		
Forced	2	50	10.5		
	2	100	5.9		
	2			300	41.9
	2			1000	13.6
	2			2500	7.4
	2			3000	6.9
	2			5000	6.1
	2			7000	5.8
Diffusion	5	50	4.5	3000	5.3
	5	50	4.5	4800	5.2
	5	100	3.0	3000	5.3

Signals from the sensors were collected through a data acquisition board (National Instruments, NIDAQPad-6020E) and processed using Labview software (National Instruments (2004) Labview 7.1). Inputting a two-volt signal from a regulated DC power supply (Protek, Model No. 303) directly into the board for a six hour time period tested the accuracy and precision of the board and software. The results of this test can be seen in Figure 2-6.

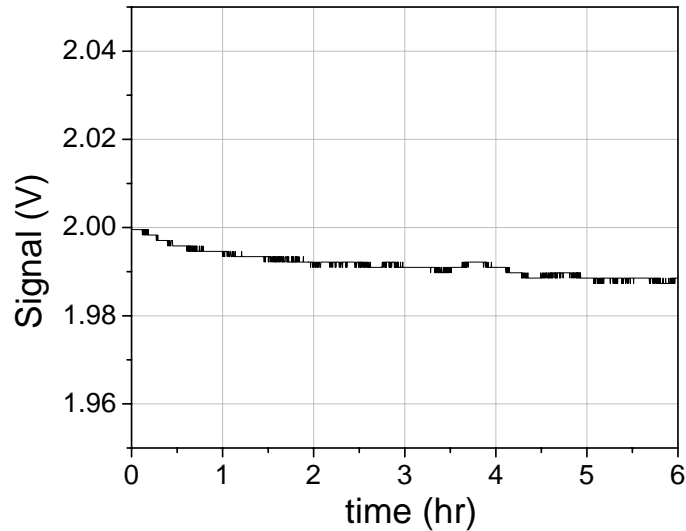


Figure 2-6 Signal from DC power supply as collected in Labview, which shows precision and accuracy of the data acquisition system over six hours.

Experimental Procedures

Before starting any of the other tests, the carbon dioxide and ammonia sensors were tested for drift of the baseline signal. Output signals were collected every 30 minutes for over 40 hours while air flowed over the sensor at a rate of 2.00 L/min. The sensors were not exposed to either ammonia or carbon dioxide during these tests.

Carbon Dioxide Sensor

Single analyte tests, where the sensor was only exposed to mixtures of air and carbon dioxide, were completed to establish a calibration curve. Since carbon dioxide levels should not exceed 5000 ppm; the measurable range was set to 300 to 7000 ppm. The sensor was exposed to concentrations between 300 and 7000 ppm carbon dioxide for 10 to 30 minutes at a time with a 10 minute purging cycle with air between exposures. These tests were all conducted using the forced flow regime.

The other experiment completed with the carbon dioxide sensor tested for cross-sensitivities to humidity. First, air flowed over the sensor for 30 minutes to establish a baseline. Then the sensor was exposed to 3000 ppm carbon dioxide for 30 minutes. The

relative humidity was then increased from dry (2%) to humid (50 – 60%). After humidifying the air, the sensor was again exposed to 3000 ppm carbon dioxide. A graphical depiction of this test can be seen in Figure 2-7.

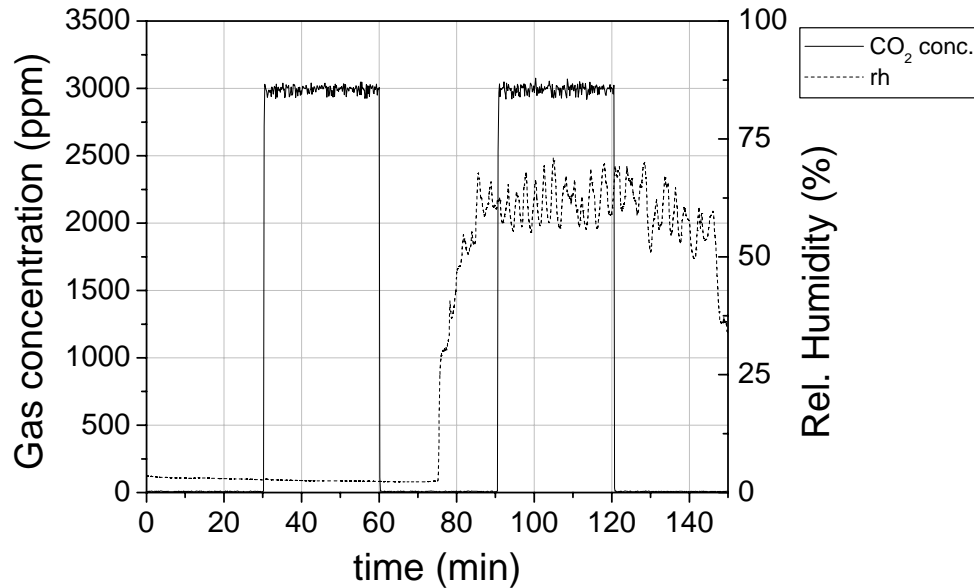


Figure 2-7 Graphical depiction of experimental parameters used to test the carbon dioxide sensor for cross-sensitivity to humidity.

Ammonia Sensor

A number of single analyte tests were conducted on the ammonia sensor in order to establish a calibration curve. Since the recommended threshold limit value (TLV) for ammonia is 25 ppm, the desired measuring range was 25 to 100 ppm. The sensor was exposed to concentrations of 25, 50, 75, and 100 ppm ammonia for 10 to 20 minutes at a time with a 10 minute purging cycle with air between exposures. These tests were all conducted using the forced flow regime.

In actual operation the sensor will not have a purging cycle after it has been exposed to air contaminants. Therefore, tests were conducted where the ammonia concentration was ramped up or down to simulate gradual changes that may be seen in the environment. The parameters used for the ramping tests are listed in Table 2-3, while

a graphical depiction is given in Figure 2-8. The ramping tests were completed using the diffusion box.

Table 2-3 Ammonia concentrations used for ramping tests.

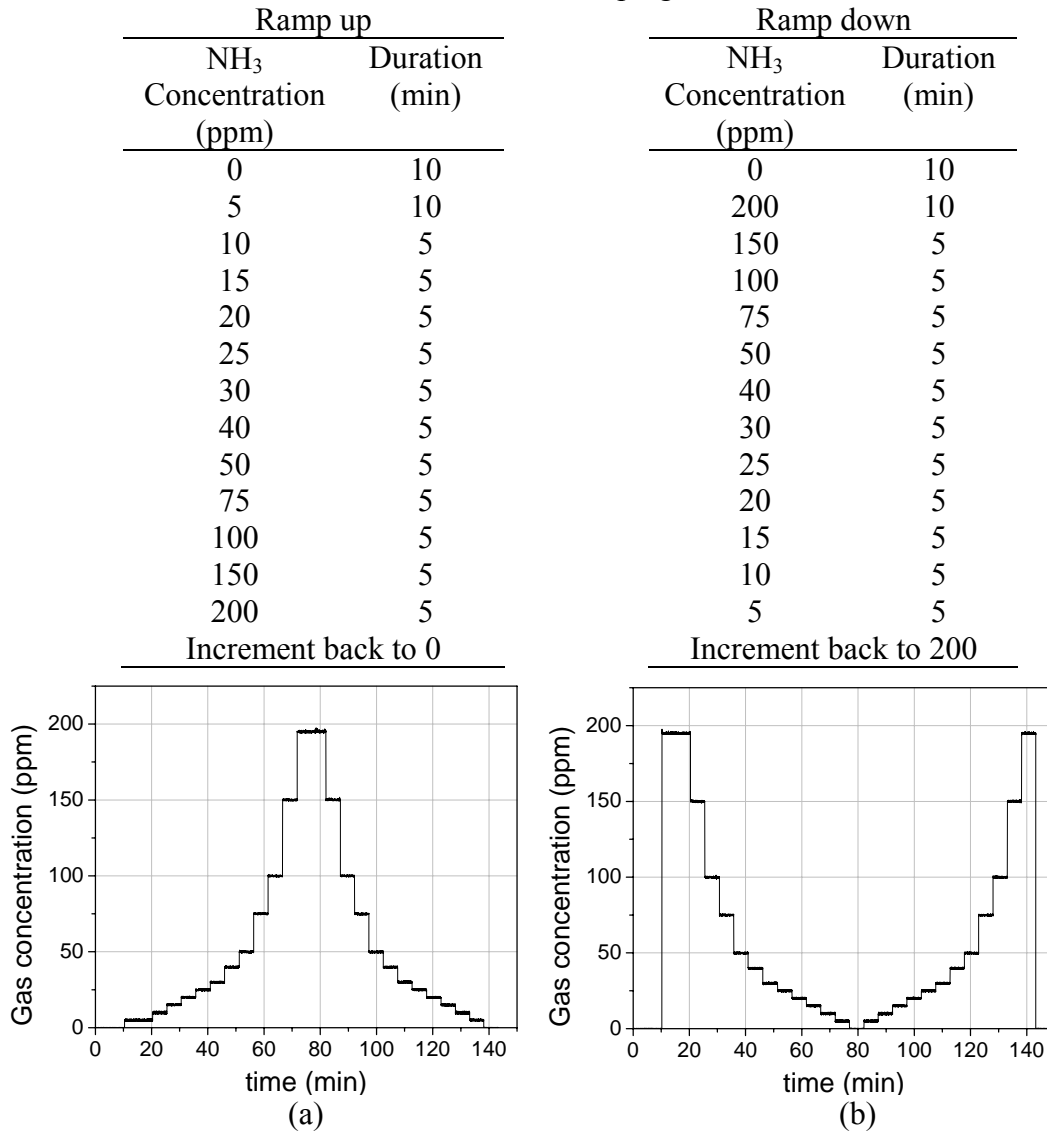


Figure 2-8 Graphical depiction of ammonia concentrations used in ramping tests.

Since the laboratory animal cage is not a homogeneous environment, the effects of other air quality factors were tested. First, the ammonia sensor was tested for cross-sensitivity to humidity. The sensor was exposed to air under dry conditions (2% rh) for 20 minutes, the relative humidity was increased to 40% rh for 20 minutes, and then this cycle was repeated twice. Six repetitions of this cycle were completed for the forced and

diffusion flow regimes. Second, the sensor was tested for cross-sensitivity to humidity while ammonia was present. The sensor was first exposed to ammonia for 30 minutes, followed by 30 minutes of air, then the relative humidity was increased, and lastly the sensor was exposed again to ammonia. A graphical depiction of the experimental parameters used for this test can be seen in Figure 2-9.

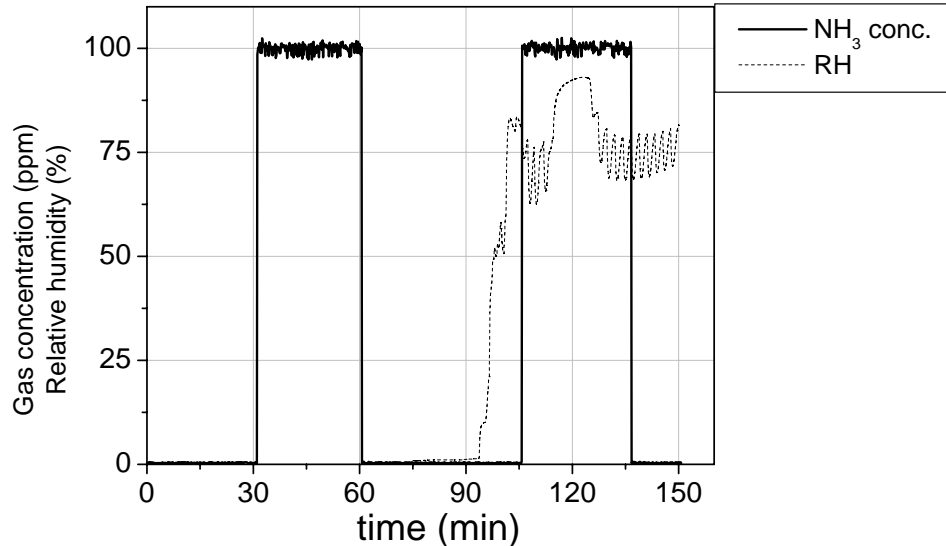


Figure 2-9 Graphical depiction of experimental parameters used to test the ammonia sensor for cross-sensitivity to humidity while ammonia was present.

Next the ammonia sensor was tested for cross-sensitivities to humidity and carbon dioxide with ammonia in the system. A graphical depiction of the combination of parameters used is shown in Figure 2-10. The introduction of each new parameter was at least 10 minutes after the last change in experimental conditions to ensure that the effect on the sensor was from the intended parameter. Six repetitions of this experiment were conducted.

Time response tests were completed to determine the amount of time required by the sensor to display 95% of a step change in gas concentration. This test also aided in determining adsorption and desorption rates of the analyte on the sensor. To complete this test, air flowed across the sensor for 10 minutes reaching steady state, and then

ammonia was added to the system for 10 minutes. The analyte stream was shut off and air again flowed over the sensor for 10 minutes. This cycle was repeated six times for each of the eight experimental conditions listed in Table 2-4.

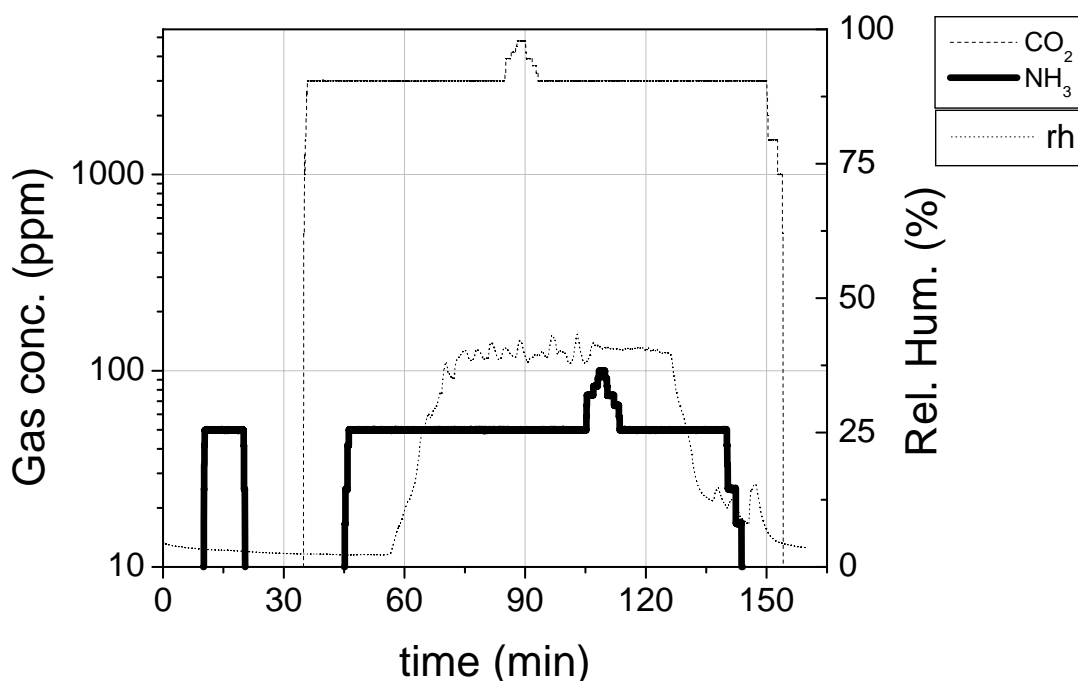


Figure 2-10 Graphical depiction of experimental parameters used to test the ammonia sensor for cross-sensitivity to humidity and carbon dioxide with ammonia in the system.

Table 2-4 Experimental parameters for time response tests (X indicates tests completed).

Flow	Humidity (%)	50 ppm NH ₃	100 ppm NH ₃
Forced	2	X	X
Diffusion	50	X	X
Forced	2	X	X
Diffusion	50	X	X

In the last set of experiments, the surface temperature of the sensor was varied to test for temperature effects on the response time of the sensor. The sensor was exposed to 50 ppm ammonia for 10 minutes at 31°C (1.0 V), 39°C (2.0 V) and 52°C (3.0 V). The temperature of the surface was controlled by an internal heater, which was powered by an external DC power supply (Protek Model No. 303). The output voltage was calibrated to

the above-mentioned temperatures. At each temperature, the experiment was repeated six times.

CHAPTER 3 THEORETICAL MODELING

The theoretical modeling of the reactions between the sensing film and analyte gases in the field effect transistors allowed for a number of questions to be investigated. The first topic of research dealt with the reaction mechanism for the ammonia gas on a titanium nitride surface. The second inquiry focused on the adsorption and desorption rates for each reaction. The goal was to model the time response for adsorption and desorption and then determine the position of chemical equilibrium. In the process of conducting these queries, the equilibrium constants for each reaction were explored. Diffusion was also investigated as it played an important role in transporting the molecules to and from the surface so that adsorption or desorption may take place. The experimental portion of the study was used to confirm the adsorption and desorption rates found through the theoretical modeling.

To determine the adsorption and desorption rates for each reaction, the position of chemical equilibrium, and the equilibrium constants, the following heterogeneous chemistry theory was reviewed and applied to the analysis.

Gibbs Free Energy

Gibbs free energy, G , is essential in determining the driving force or spontaneity of chemical reactions, the equilibrium constant, and the position of chemical equilibrium, where the equilibrium position of a reaction is said to lie far to the right if almost all reactants are used up and far to the left if scarcely any product is formed. Gibbs energy can be described by the following equation,

$$G = H - TS, \quad (3.1)$$

where H is enthalpy, T is the absolute temperature, and S is entropy. For an isothermal process, the change in free energy as the process proceeds can be written as,

$$\Delta G = \Delta H - T\Delta S. \quad (3.2)$$

A chemical process will continue in the direction that decreases the free energy. For example, if $\Delta G < 0$ then the forward reaction will continue spontaneously. Likewise, if $\Delta G > 0$ then the reverse reaction will occur spontaneously. The process continues in the direction to minimize the free energy of the system until $\Delta G = 0$, at which point equilibrium is achieved.

The free energy change can be related to the reaction equilibrium constant. First, consider the elementary reaction



If the reaction proceeds by a differential amount, $d\xi$, then the number of moles of each chemical species changes according to

$$dn_A = -ad\xi, \quad (3.4)$$

$$dn_B = -bd\xi, \quad (3.5)$$

$$dn_X = xd\xi, \quad (3.6)$$

$$dn_Y = yd\xi. \quad (3.7)$$

The total differential of mixture free energy is thus

$$dG = -SdT + Vdp + \sum_{k=1}^K \mu_k dn_k, \quad (3.8)$$

where μ is the chemical potential. At fixed temperature and pressure, this equation converts to

$$dG = \mu_A dn_A + \mu_B dn_B + \mu_X dn_X + \mu_Y dn_Y. \quad (3.9)$$

$$dG = -a\mu_A d\xi - b\mu_B d\xi + x\mu_X d\xi + y\mu_Y d\xi \quad (3.10)$$

$$dG = (x\mu_X + y\mu_Y - a\mu_A - b\mu_B) d\xi \quad (3.11)$$

$$\left(\frac{dG}{d\xi} \right)_{p,T} = (x\mu_X + y\mu_Y - a\mu_A - b\mu_B). \quad (3.12)$$

Equilibrium is reached when

$$\left(\frac{dG}{d\xi} \right)_{p,T} = 0. \quad (3.13)$$

Therefore at equilibrium,

$$x\mu_X + y\mu_Y - a\mu_A - b\mu_B = \Delta\mu_r = 0. \quad (3.14)$$

Considering the chemical potential at standard state, Eq. 3.12 can be written as,

$$x(\mu_X^\circ + RT \ln p_X) + y(\mu_Y^\circ + RT \ln p_Y) - a(\mu_A^\circ + RT \ln p_A) - b(\mu_B^\circ + RT \ln p_B) = 0. \quad (3.15)$$

With this result, a constraint is put on the pressures that the four gases can have at equilibrium. Rearranging Eq. 3.15 leads to

$$-RT \ln \left[\frac{(p_X)^x (p_Y)^y}{(p_A)^a (p_B)^b} \right]_{eq} = x\mu_X^\circ + y\mu_Y^\circ - a\mu_A^\circ - b\mu_B^\circ, \quad (3.16)$$

$$-RT \ln \left[\frac{(p_X)^x (p_Y)^y}{(p_A)^a (p_B)^b} \right]_{eq} = \Delta G_r^\circ. \quad (3.17)$$

Because the right hand side of Eq. 3.17 is constant for a given temperature, the logarithmic term must also equal a constant,

$$K_p = \left[\frac{(p_X)^x (p_Y)^y}{(p_A)^a (p_B)^b} \right]_{eq}, \quad (3.18)$$

known as the equilibrium constant. If K_p is greater than one, the products of reaction are favored over the reactants and the forward reaction proceeds.

Based on Eq. 3.17 and K_p , at equilibrium,

$$\Delta G_r^o = -RT \ln K_p, \quad (3.19)$$

where it can be rewritten with the help of Eq. 3.2 as

$$-\Delta H_r^o + T\Delta S_r^o = RT \ln K_p \quad (3.20)$$

or

$$\frac{-\Delta H_r^o}{T} + \Delta S_r^o = R \ln K_p. \quad (3.21)$$

When the reaction is exothermic, $-\Delta H_r^o/T$ relates to a positive change of entropy of the surroundings and favors the formation of the products. As the temperature increases, $-\Delta H_r^o/T$ decreases and the increasing entropy of the surroundings has a less powerful effect. Resultantly, the equilibrium lies less to the right. If the reaction is endothermic, the primary factor is the increasing entropy of the reaction system. The significance of the unfavorable change of the entropy of the surroundings is lessened as the temperature increases and the reaction can shift towards the products.

Looking at the forward and reverse rates of progress at equilibrium develops the equilibrium concentration constant, K_c . If the reaction is at equilibrium, then,

$$k_{f,i} \prod_{k=1}^K [X_k]^{v'_{ki}} = k_{r,i} \prod_{k=1}^K [X_k]^{v''_{ki}} \quad (3.22)$$

or

$$K_{c,i} = \frac{k_{f,i}}{k_{r,i}} = \prod_{k=1}^K [X_k]_e^{v_{ki}}, \quad (3.23)$$

where e indicates equilibrium, and ν_{ki} is the net stoichiometric coefficient for species k in reaction i . Concentration is related to pressure through the ideal gas law,

$$[X_k] \equiv \frac{n_k}{V} = \frac{p_k}{RT}. \quad (3.24)$$

Equation 3.23 now becomes,

$$K_{c,i} = \prod_{k=1}^K \left(\frac{p_k}{RT} \right)_e^{\nu_{ki}} \quad (3.25)$$

The equilibrium pressure constant for a general reaction is written as,

$$K_{p,i} = \prod_{k=1}^K \left(\frac{p_k}{p^\circ} \right)_e^{\nu_{ki}} \quad (3.26)$$

where p° is the standard-state pressure. The two equilibrium constants can be combined into one equation as follows,

$$K_{c,i} = K_{p,i} \prod_{k=1}^K \left(\frac{p^\circ}{RT} \right)_e^{\nu_{ki}}. \quad (3.27)$$

Gibbs free energy and associated thermodynamic terms were an essential part of examining the reaction of ammonia on a titanium nitride surface.

Adsorption

The reactions between the titanium nitride surface on the field effect transistor and ammonia occurred through adsorption, attachment of particles to the surface. The substance that adsorbs is called the adsorbate while the underlying material is the adsorbent. The reverse of adsorption is desorption. Adsorption can occur in two ways: physical adsorption, physisorption, or chemical adsorption, chemisorption.

Physical adsorption is due to van der Waals interactions between the adsorbate and the adsorbent. Van der Waals interactions have a long range, but are weak. The energy

released is on the same order of magnitude as the enthalpy of condensation, roughly 20 kJ/mol. These small energies are absorbed as vibrations of the lattice structure and dissipated as thermal motion. A molecule will bounce around and finally adsorb to the surface in a process called accommodation. The bonds do not break; therefore a physisorbed molecule retains its identity (48).

In chemical adsorption the molecules adhere to the surface by forming a chemical bond, typically covalent. In comparison with physisorption, the enthalpy of chemisorption is ten times greater at approximately 200 kJ/mol. The distance between the surface and closest adsorbate atom is shorter for chemisorption than for physisorption. A chemisorbed molecule may be torn apart at the demand of unsatisfied valences of surface atoms. The existence of molecular fragments on the surface is one reason why solid surfaces catalyze reactions.

Chemisorption is most often exothermic, which can be proven by examining the Gibbs equation, $\Delta G = \Delta H - T\Delta S$. For chemisorption to be a spontaneous process, $\Delta G < 0$ and because the translational freedom of the adsorbate is reduced when it is adsorbed, $\Delta S < 0$. Therefore, the enthalpy of adsorption, ΔH , must be negative, which indicates an exothermic nature. The enthalpy of adsorption, however, is dependent on the extent of surface coverage because the adsorbate particles interact with each other. For example, if the particles repel each other like CO on palladium, adsorption becomes less exothermic as the coverage increases. If the particles attract each other, such as O₂ on tungsten, the process becomes more exothermic as the particles cluster together.

The rate and extent to which a surface is covered are important when considering heterogeneous reactions. Molecules will quickly cover a surface exposed to a gas. The collision flux, Z_w , can be expressed as,

$$Z_w = \frac{P}{(2\pi mkT)^{1/2}} \quad (3.28)$$

As an example, air with molecular weight of 29 g/mol at 1 atm and 25°C, will have a collision flux of $3 \times 10^{27} \text{ m}^{-2}\text{s}^{-1}$. So for a one meter square metal surface containing 10^{19} atoms, each atom is struck approximately 10^8 times each second. The fractional coverage, Θ , is given by,

$$\Theta = \frac{\text{number of adsorption sites occupied}}{\text{number of adsorption sites available}} = \frac{V}{V_\infty} \quad (3.29)$$

where V_∞ is the volume of adsorbate corresponding to complete monolayer coverage.

The rate of adsorption, $\frac{d\Theta}{dt}$, is determined by observing the change of fractional coverage over time.

Surface Reaction Rate Expressions

A number of classic rate expressions can be used to typify heterogeneous reactions. These include adsorption isotherms, competitive adsorption, and dissociative adsorption.

Langmuir Adsorption Isotherm

The free gas and adsorbed gas are in dynamic equilibrium where the fractional coverage of the surface depends on the pressure of the overlying gas. The variation of the fractional coverage with pressure at a specified temperature is known as the adsorption isotherm.

The Langmuir adsorption isotherm describes the equilibrium between a single-component gas, A, and adsorbed species, A(s), at a surface. It is based on three assumptions (48):

- Adsorption cannot proceed beyond monolayer coverage.
- All sites are equivalent and the surface is uniform.
- Ability of a molecule to adsorb at a given site is independent of the occupation of neighboring sites.

The isotherm expression relates the fraction of surface, Θ_A , covered by the adsorbed species as a function of partial pressure, p_A , exposed to the surface and is given as follows,

$$\Theta_A = \frac{Kp_A}{1 + Kp_A}. \quad (3.30)$$

At low partial pressures, the coverage of adsorbed species increases linearly with the partial pressure. As the partial pressure of A increases, the amount of adsorbed A(s) begins to saturate, and the coverage Θ_A approaches unity. The monolayer has thus been completed and further adsorption cannot take place.

An equivalent expression for the isotherm can be developed using mass-action kinetics. For a gas molecule reacting with the surface, the adsorption process proceeds as follows,



where O(s) represents an open site on the surface and k_1 and k_{-1} are the equilibrium constants for the forward and reverse processes, respectively. At equilibrium the concentration of the surface adsorbed species is constant and can be represented by

$$\frac{d[A(s)]}{dt} = 0 = k_1[A][O(s)] - k_{-1}[A(s)]. \quad (3.32)$$

If the open site is related to the site density, Γ , by

$$[O(s)] = \Gamma - [A(s)], \quad (3.33)$$

then at steady-state,

$$k_1[A]\Gamma = (k_{-1} + k_1[A])[A(s)]. \quad (3.34)$$

The coverage Θ_A then becomes,

$$\Theta_A = \frac{[A(s)]}{\Gamma} = \frac{k_1[A]}{k_{-1} + k_1[A]} = \frac{K_c[A]}{1 + K_c[A]} \quad (3.35)$$

Using Eq. 3.2 the coverage can be expressed in terms of pressure as

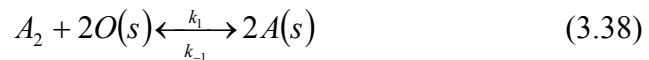
$$\Theta_A = \frac{K_p(p_A/p^o)}{1 + K_p(p_A/p^o)}. \quad (3.36)$$

Dissociative Adsorption

Some molecular species undergo dissociation upon adsorption, especially on metal surfaces. For example, H_2 dissociates on a metal surface into two surface adsorbed H(s) atoms. Likewise, methane dissociates into $CH_3(s)$ and H(s). Dissociative adsorption is assumed to require two open sites on the surface. The process of adsorption and dissociation are thought to occur in a single step. The site fraction is given by

$$\Theta_A = \frac{(Kp)^{1/2}}{1 + (Kp)^{1/2}}. \quad (3.37)$$

Mass-action kinetics provides a surface reaction of



and leads to the surface site fraction on a concentration basis:

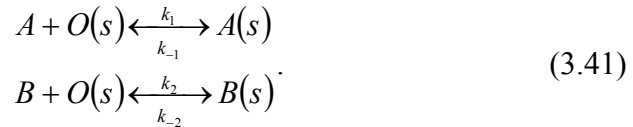
$$\Theta_A = \frac{K_{c,1}^{1/2}[A_2]^{1/2}}{1 + K_{c,1}^{1/2}[A_2]^{1/2}} \quad (3.39)$$

Competitive Adsorption

In competitive adsorption, two gases A and B are considered when modeling. Both gases are present above a surface and compete for available sites on the surface for adsorption. The coverage of Θ_A and Θ_B are represented as follows

$$\begin{aligned} \Theta_A &= \frac{K_A p_A}{1 + K_A p_A + K_B p_B} \\ \Theta_B &= \frac{K_B p_B}{1 + K_A p_A + K_B p_B} \end{aligned} \quad (3.40)$$

From mass-action kinetics the reaction rate expressions for A and B are



The steady state analysis, similar to the development of the Langmuir isotherm, leads to an expression for the surface coverage for both A and B:

$$\begin{aligned} \Theta_A &= \frac{K_{c,1}[A]}{1 + K_{c,1}[A] + K_{c,2}[B]} \\ \Theta_B &= \frac{K_{c,2}[B]}{1 + K_{c,1}[A] + K_{c,2}[B]} \end{aligned} \quad (3.42)$$

Adsorption of ammonia on the surface was assumed to occur by chemisorption. The Langmuir adsorption isotherm was used as the basis for the reaction mechanism. Competitive adsorption was important when considering ammonia in humid air, where both ammonia and water were competing for available surface sites.

Proposed Mechanisms

Due to the limited amount of testing that could be done with the carbon dioxide sensor, the model focused only on reactions occurring on the ammonia sensor. To detect ammonia a titanium nitride (TiN) film was used as the sensing layer. The change in ammonia concentration was detected by a change in the work function of the sensing layer. Several hypotheses for the reaction mechanism, which causes the change in the work function, were considered.

Ammonia and Hydroxide

The first reaction mechanism considered involved ammonia and hydroxide (OH). Previous work by Ostrick et al. (44) indicated that ammonia may bond to OH groups or OH-precovered sites on the sensing layer. Two mechanisms are possible, either the ammonia removes the OH from its binding sites or the ammonia binds directly to the OH groups already on the surface. The mechanism proposed was based on the following:

1. Peaks seen in Diffuse Reflectance Infrared Fourier Transform Spectra (DRIFT-spectra), Figure 3-1,
2. Sensitivity of the TiN sensing layer at room temperature versus at higher temperatures (120°C), and
3. Experiments by Takagi-Kawai et al. (49) where a similar mechanism was proposed.

Considering first the spectra of Figure 3-1, the peaks at 1450 cm^{-1} and between $3600 - 3800\text{ cm}^{-1}$ were attributed to OH groups, the deformation vibration and free or H-bridge-bonded valence vibration, respectively. Increases in signal were attributed to ammonia as follows: 1600 cm^{-1} , asymmetric deformation band of NH_3 , $2700 - 2800\text{ cm}^{-1}$, $\nu(\text{N-H})$ of ammonia ions, and $3000 - 3300\text{ cm}^{-1}$, NH stretching region.

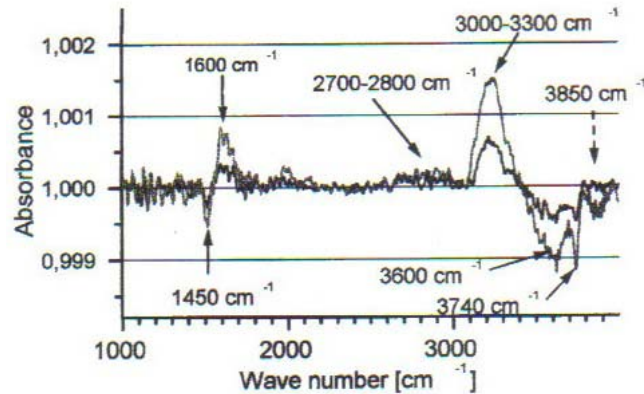


Figure 3-1 Diffuse Reflectance Infrared Fourier Transform Spectra (DRIFT-spectra) for a TiN screen-printed film, where absorbance was used to distinguish between the species. (Data of Ostrick et al. (44)).

Next Ostrick et al. (44) indicated that because of the high affinity between ammonia and water, the small concentration of ammonia molecules (<100 ppm) will react entirely with the high concentration of surface water (>5000 ppm). Also, in the second reaction step, the ammonia ions may react directly with the sensing layer or with adsorbed OH ions. When the temperature rises, the amount of water on the surface decreases along with the solubility of ammonia in water. Resultantly, the amount of ammonia on the TiN surface is reduced and the sensitivity decreases.

From Takagi-Kawai et al. (49) evidence of a reaction between ammonia and hydroxide on a surface is depicted in Figure 3-2.

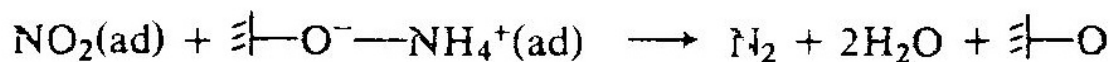
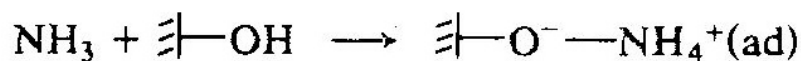
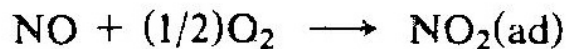


Figure 3-2 Mechanism for the reduction of NO by NH₃ over a V₂O₅ sensing layer in the presence of oxygen. (Data of Takagi – Kawai et al. (49).)

This mechanism was derived from infrared (IR) and x-ray photoelectron spectroscopy (XPS). The spectra from several surfaces were compared as seen in Table 3-1.

Table 3-1 Infrared (IR) and XPS measurements and assignments for adsorbed species of ammonia on surface catalysts. Degenerate deformation and symmetric deformation are indicated by δ_d and δ_s , respectively. (Data of Takagi – Kawai et al. (49).)

Surface	IR (cm^{-1})			XPS (ev)		
	$\delta_s\text{NH}_4^+$	$\delta_d\text{NH}_3$	$\delta_s\text{NH}_3$	$\delta_s\text{NH}_4^+$	$\delta_d\text{NH}_3$	$\delta_s\text{NH}_3$
V_2O_5	1413	-----	-----	400.9	-----	-----
$\text{V}_2\text{O}_5/\text{Al}_2\text{O}_3$	1410	1610	1275	401.0	400.2	400.2
Al_2O_3	-----	1610	1275	-----	400.0	400.0
$\text{V}_2\text{O}_5/\text{SiO}_2$	1435	1620	-----	401.0	-----	-----
$\text{V}_2\text{O}_5/\text{TiO}_2$	1424	1605	1238	401.0	399.4	399.4
TiO_2	-----	1605	1177	-----	399.6	399.6
NH_4VO_3	1410	-----	-----	400.9	-----	-----

By comparison, only one peak from Figure 3-1, at 1600 cm^{-1} , matches up with those in Table 3-1. Shimanouchi (50) has also reported this mode, degenerate deformation, with great certainty as 1627 cm^{-1} . Ostrick et al. (44) indicated there was a peak between $2700 - 2800\text{ cm}^{-1}$, which was evidence of NH_4^+ . Since this peak does not match up with the values for $\delta_s\text{NH}_4^+$ in Table 3-1, another look suggests that the absorbance in this region is not large enough to warrant it as a peak. For example, the absorbance seen in the region between $2700 - 2800\text{ cm}^{-1}$ is no greater than at wave number 2000 cm^{-1} , which was not considered by Ostrick et al. (44). With that in mind, NH_4^+ may not even be a product and therefore another mechanism should be considered.

Ammonia Dissociation

The second mechanism considered was dissociation of ammonia on the TiN surface. Several studies examining ammonia reactions on various surfaces have been done. The earliest studies evaluated the reaction of ammonia on silicon surfaces. Later

investigations examined ammonia on other transition metal surfaces such as titanium and silicon, titanium nitride and platinum, and nickel.

Hlil et al. (51) used x-ray photoemission spectroscopy (XPS) and ultra-violet photoemission spectroscopy (UPS) to study chemisorption of ammonia on a Si(100) surface at substrate temperatures from 100 to 700 K. When the surface was exposed to ammonia at low temperatures (100 K), a line appeared at 400.0 eV binding energy, curve (a) in Figure 3-3, which was attributed to molecular condensation on the substrate. At room temperature another line emerged at 398.5 eV, curve (b) in Figure 3-3, which correlates to NH_X ($X = 1,2$). Additionally, the presence of weak silicon to hydrogen bonds evidences partial dissociation and co-adsorption of NH_X radicals and atomic H.

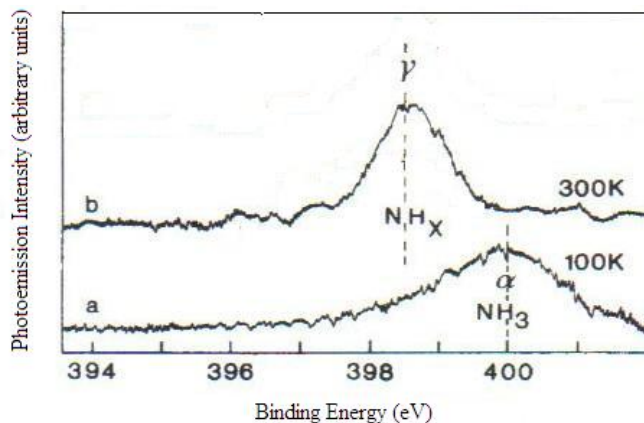


Figure 3-3 The XPS N(1s) core-level spectra for ammonia over the Si(100) surface as a function of substrate temperature. (Data of Hlil et al. (51)).

Bozso and Avouris (52) also studied reactions of two different silicon substrates with NH_3 and atomic nitrogen using XPS and UPS. On a Si(100)-(2x1) surface at 100 K a peak at 400.1 eV, physisorbed molecular ammonia, was visible. Another peak was evident at 398.5 eV, although not as clearly defined as the NH_3 peak. As the temperature increased to 300 K, this peak became more defined. Again this peak was most probably due to NH_2 or NH . Upon further annealing to higher temperatures, the peak broadened to

a lower binding energy indicating conversion of this species. When annealed to 950 K, a peak appeared at 397.7 eV, atomic nitrogen on the silicon surface, which resulted from complete dissociation of the NH_x intermediate at 398.5 eV. Both the molecular ammonia (400.1 eV) and N bonded to silicon (397.7 eV) species were also seen on the Si(111)-(7x7) surface. A surface species produced by dissociation was also apparent on this surface, but at a slightly higher binding energy of 398.8 eV. Figure 3-4 illustrates the transition from low to high temperature on both surfaces.

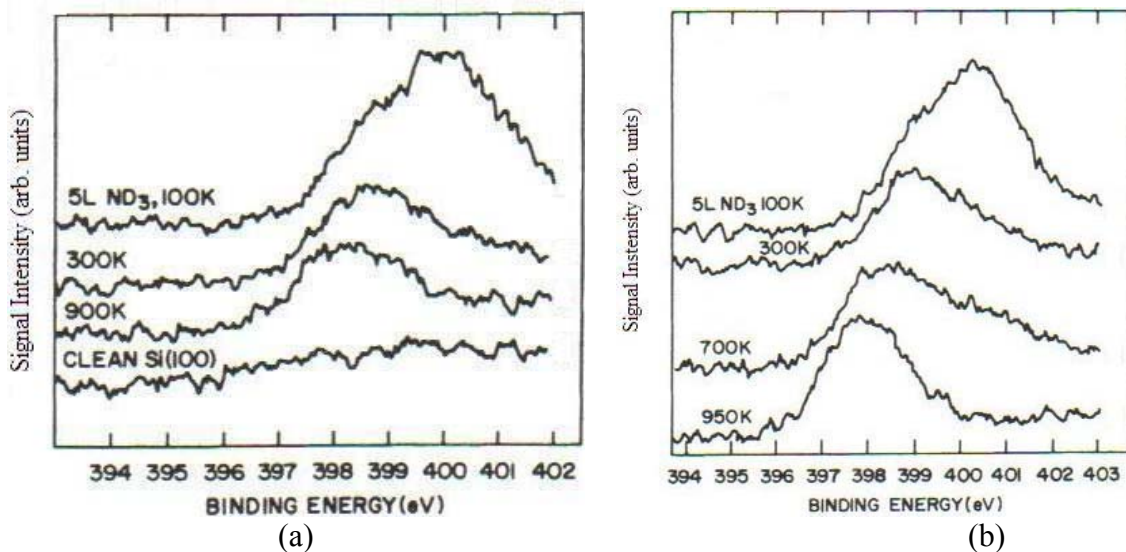


Figure 3-4 The XPS N(1s) core-level spectra for ammonia on (a) Si(100)-(2x1) and (b) Si(111)-(7x7) surfaces as a function of substrate temperature. (Data of Bozso and Avouris (52).)

Bischoff et al. (53) used ultra high vacuum (UHV) multilayer preparations, which combined the different species, to identify by XPS the nitrogen chemical environments in the Si/NH₃ system. The assignment of the binding energies was found as follows:

Nitride ($\text{Si}_3 \equiv \text{N}$)	397.4 eV
Imide ($\text{Si}_2 = \text{N} - \text{H}$)	398.0 eV
Amide ($\text{Si} - \text{N} = \text{H}_2$)	398.6 eV
NH ₃ physisorbed	400.1 eV

Zhou et al. (54) studied the decomposition of NH_3 on $\text{Si}(100)$ using static secondary ion mass spectroscopy (SSIMS). This procedure probed the surface directly and followed reaction intermediates in real time. At low temperatures, 100 K, adsorption of NH_3 on $\text{Si}(100)$ was dissociative and produced $\text{NH}_2(\text{a})$ and $\text{H}(\text{a})$. Some thermal decomposition of $\text{NH}_2(\text{a})$ to $\text{N}(\text{a})$ and $\text{H}(\text{a})$ occurred at 320 K, but most of the $\text{NH}_2(\text{a})$ was stable up to 630 K. $\text{NH}_2(\text{a})$ decomposed rapidly between 630-730 K, with no evidence of $\text{NH}(\text{a})$ at this temperature. Some $\text{NH}_2(\text{a})$ recombined with $\text{H}(\text{a})$ at 685 K to liberate $\text{NH}_3(\text{g})$. Temperature programmed desorption (TPD) was also completed and revealed that $\text{NH}_3(\text{g})$ was desorbed at room temperature. Figure 3-5 illustrates the surface species and desorption products found as the temperature increased from 100 to 1000 K.

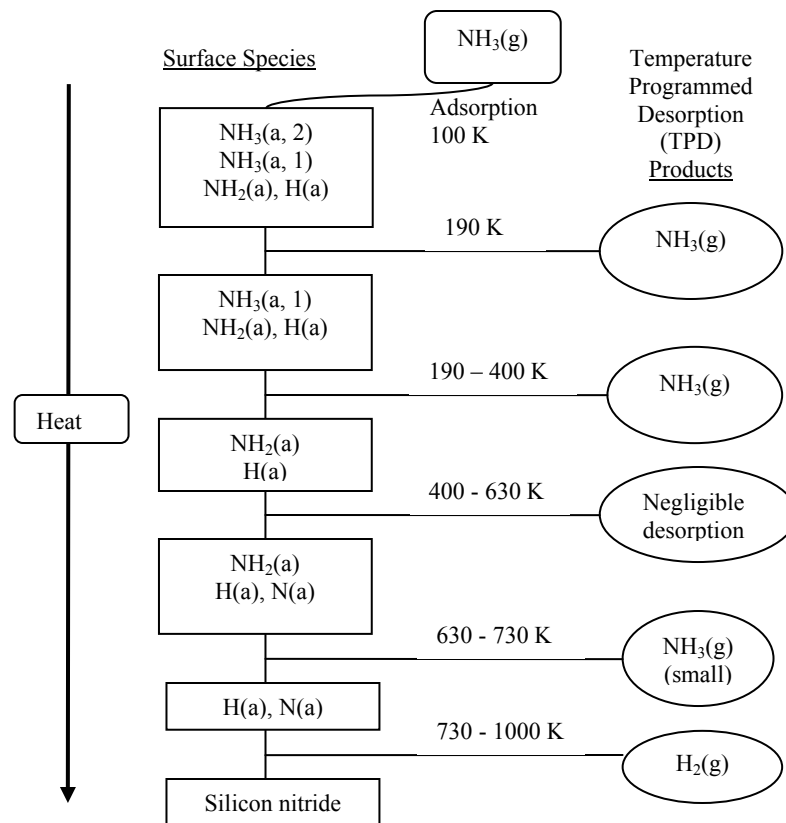


Figure 3-5 Surface species and desorption products from ammonia on $\text{Si}(100)$. (Data of Zhou et al. (54).)

Chen et al. (55) examined ammonia surface chemistry on two different surfaces, Si(111) – (7x7) and Si(100) – (2x1) using a high resolution electron energy loss spectrometer (HREELS) and TPD. On the Si(111) surface dissociative adsorption produced $\text{NH}_2(\text{a})$ and $\text{H}(\text{a})$, and between 300 and 600 K further dissociation occurred to produce $\text{NH}(\text{a})$. On the Si(100) surface, the $\text{NH}_2(\text{a})$ species remained thermally stable until approximately 600 K. The differing geometries of the two surfaces contributed to the species that were stable between 300 and 600 K. Figure 3-6 shows a ball and stick model of the two different surfaces, as well as the adsorption geometry of ammonia on the surface.

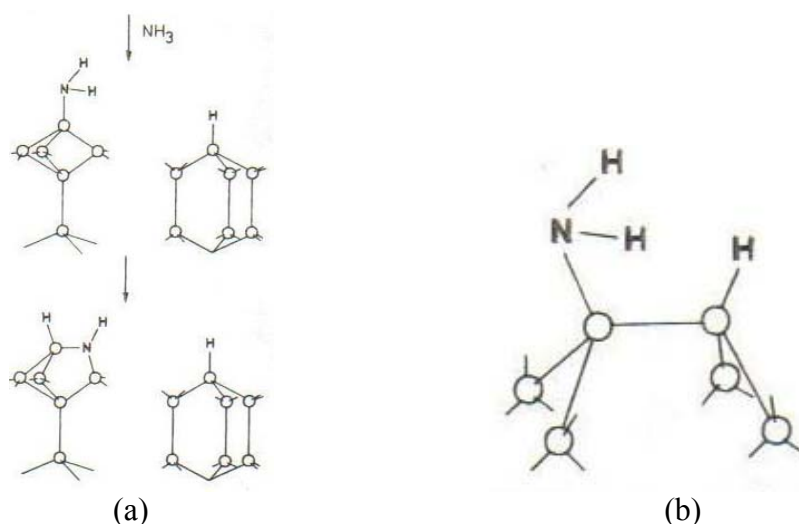


Figure 3-6 Ball and stick models for the adsorption geometry for -NH_2 and -H on two different surfaces: (a) Si(111) – (7x7) and (b) Si(100) – (2x1). (Data of Chen et al. (55).)

Siew et al. (56) used XPS to observe the adsorption and reaction of ammonia on a titanium/silicon surface (100). At low temperatures, 120 K, three N1s peaks emerged: 397.8 – 398.1, 400.5 – 400.8, and 402.2 – 402.6 eV, attributed to NH_X ($X = 1$ or 2), molecular NH_3 , and $\text{NH}_4^{\delta+}$, respectively. At room temperature more NH_3 molecules desorbed and $\text{NH}_4^{\delta+}$ disappeared indicating the species was not stable at room

temperature. Some conversion of the NH_x species occurred and the N diffused into the film. Figure 3-7 shows the spectra at 120 and 300 K.

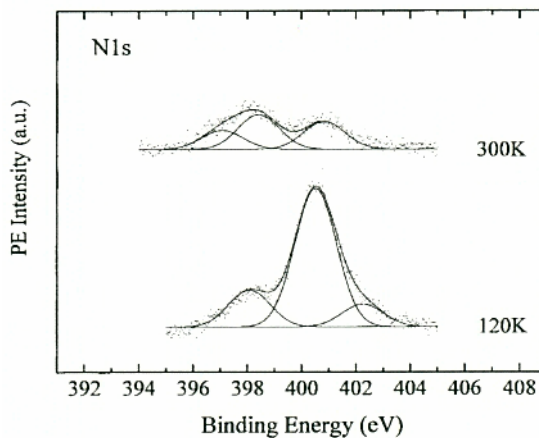
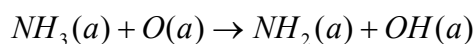


Figure 3-7 The XPS N 1s spectra of Ti/Si (100) surface at 120 and 300 K. (Data of Siew et al. (56)).

Abom et al. (43) used titanium nitride as part of a sensing layer of a field effect metal-insulator-semiconductor device. The three different layers investigated for responses to ammonia and hydrogen were: TiN, a double layer with platinum on top of TiN, and two-phase Pt – TiN films formed by co-sputtering. The sensor response to ammonia, hydrogen, propene, and acetaldehyde was measured and it was found that devices containing platinum were responsive to all gases. Devices without platinum did not respond to any of the test gases. Abom et al. (43) indicated that the change in signal of the sensor was due to an interaction with hydrogen. It was assumed that only atomic hydrogen diffused through the film and that atomic hydrogen was only created when Pt was present. From the results it was apparent that the response to ammonia was due to dissociation of ammonia molecules and detection of atomic hydrogen.

Laksono et al. (57) studied the adsorption of NH_3 on clean and oxygen pre-treated nickel (111) surfaces at room temperature using XPS. Without oxygen on the nickel

surface, no adsorption of ammonia was observed. Similarly, the surface reactivity was strongly linked to the presence of adsorbed oxygen; it increased with increasing adsorbed oxygen coverage. Two N – adspecies were detected from N1s core level peak: 399.8 (molecular) and 397.8 (dissociated). Looking at the O1s core level peak revealed that at low ammonia exposures, the hydroxyl component increased, while the main feature at 529.9 eV decreased. Laksono et al. (57) found that the concurrent transformation of both peaks indicates that hydrogen is removed from ammonia by the adsorbed oxygen to produce OH and NH_x. Quantitative treatment of the XPS offered the following stoichiometry for the reaction:



Additionally, the experiments indicated that the kinetics of desorption were faster than the kinetics of dissociation.

Molecular Adsorption

This last piece of evidence leads into the next mechanism, molecular adsorption of ammonia. While dissociation of ammonia was seen on many surfaces, it is possible that in the present study the rate of ammonia desorption is faster than the rate of dissociation.

Diebold and Madey (58) investigated adsorption and electron stimulated desorption of NH₃ on TiO₂(110) by XPS and low-energy ion scattering (LEIS). Three different surfaces were studied: (1) a stoichiometric surface, (2) a thermally treated, slightly oxygen deficient surface, and (3) a sputtered, highly oxygen deficient surface. Ammonia was seen to adsorb molecularly on all three surfaces and the saturation coverage was governed by repulsive interactions between the molecules. Diebold and

Madey (58) proposed a model in which ammonia adsorbs at titanium cation sites and where lateral repulsion between the ammonia molecules along one-dimension limits the saturation coverage. For the stoichiometric surface, ammonia appeared to desorb in molecular form, whereas for the highly oxygen deficient surface electron stimulated dissociation of ammonia was seen. The final product of this dissociation process was atomic nitrogen. The previous experiments were done at 160 K. On the highly oxygen-deficient surface, heating the surface to 395 K desorbed all nitrogen-containing species from the surface, with no evidence of thermally induced dissociation. Therefore, it was concluded that ammonia was adsorbed as an intact molecule.

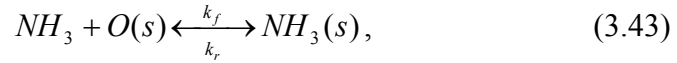
Karthigeyan et al. (59) studied an iridium oxide thin film integrated HSGFET which was selectively sensitive to ammonia at room temperature. An increase in sensor signal for ammonia at higher temperatures was seen, but the nature of the response to ammonia was unchanged from room temperature to 100°C. A possible reaction mechanism for ammonia on the sensing layer was based on the sharing of lone donor bond to positively charged vacancies by chemisorption. The sensor showed no response to concentrations of hydrogen up to 10,000 ppm. Additionally, the signal response was negligible to CO, SO₂, Cl₂, and NO₂.

Karthigeyan et al. (59) indicated that in the classical model, a charge transfer between adsorbed molecules and the surface of the sensitive layer and/or dipole moments of adsorbed molecules on the surface create a surface dipole layer which causes a work function change. A decrease in the work function upon ammonia adsorption indicates that there is a net electron transfer from ammonia to cation sites on the surface. The strong nature of the ammonia reaction is further indicated by the effect of temperature on

the reaction and recovery properties seen in the transient response of the sensor. The increase of the work function signal with temperature came from diffusion of the ammonia molecule into the film. Diffused molecules attached to cation sites lying underneath the surface. The desorption was complicated by residual gases in the measurement chamber and changes in bonding nature of adsorbed molecules before adsorption, i.e. surface diffusion to alternative bonding sites, lateral interactions between ammonia molecules, or immediate compound formation due to ammonia dissociation.

Reaction Kinetics

Based on the preceding evidence, molecular adsorption of ammonia on the titanium nitride surface was chosen as the reaction mechanism for the model. Therefore the reaction mechanism was described as follows,



where $O(s)$ is an open surface site and $NH_3(s)$ represents ammonia adsorbed on the surface. For the rate of the forward reaction or adsorption the forward and reverse reactions were considered together as,

$$\begin{aligned} \frac{d[NH_3(s)]}{dt} &= k_f p_{NH_3} [O(s)] - k_r [NH_3(s)] \\ &= k_f [NH_3(g)] ([S]_{s.s.} - [NH_3(s)]) - k_r [NH_3(s)] \end{aligned} \quad (3.44)$$

Upon integration,

$$[NH_3(s)] = \frac{[S]_{s.s.} \left(1 - e^{(-k_f [NH_3(g)] + k_r)t}\right)}{1 + \frac{k_r}{k_f [NH_3(g)]}} \quad (3.45)$$

where $[S]_{s.s.}$ is the total concentration of sites on the surface where the ammonia can adsorb at steady-state. This is different than total site density, Γ , because $[S]_{s.s.}$ varies

with the free stream gas concentration. For example, the number of sites the analyte occupied was less at a lower analyte free stream concentration than at a higher analyte concentration.

For the reverse reaction the analyte was removed by forced flow rather than by diffusion thereby quickly forcing the ammonia out of the free stream, which caused the first term on the right hand side of Eq. 3.44 to be negligible compared with the reverse reaction. Therefore, the rate of the reverse reaction or desorption is

$$\frac{d[NH_3(s)]}{dt} = -k_r[NH_3(s)]. \quad (3.46)$$

Integration leads to

$$[NH_3(s)] = [S]_{s.s.} \exp(-k_r t). \quad (3.47)$$

At equilibrium,

$$[NH_3(s)] = [S]_{s.s.} \frac{Kp_{NH_3}}{1 + Kp_{NH_3}}, \quad (3.48)$$

where $K = k_f/k_r$. Also at equilibrium,

$$\begin{aligned} K &= \exp(-\Delta G / RT) \\ &= \exp(\Delta S / R) \exp(-\Delta H / RT) \end{aligned} \quad (3.49)$$

The rate equations were made dimensionless to allow them to be used in other applications where the physical parameters, such as the area of the sensing film, may be different. The dimensionless variables were as follows,

$$\Theta = \frac{[NH_3(s)]}{[S]_{s.s.}}, \quad (3.50)$$

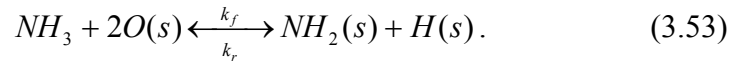
and

$$\tau = \frac{Dt}{W \cdot L}, \quad (3.51)$$

where D is the diffusion coefficient and W and L are the width and length of the sensitive film. Equation 3.44 in dimensionless form now becomes,

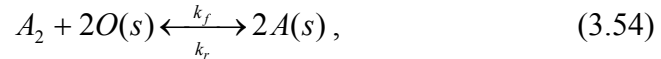
$$\frac{d\Theta}{d\tau} = (k_f[NH_3(g)](1 - \Theta) - k_r\Theta)\frac{W \cdot L}{D}. \quad (3.52)$$

As noted above, molecular adsorption was the focus of this study, however since dissociation was not ruled out as a possible reaction mechanism, the rate equations for dissociation were formulated and integrated. The reaction mechanism for ammonia dissociation on a titanium nitride surface was as follows,



The dissociative adsorption was assumed to require two open surface sites and the adsorption and breaking-apart of the molecule were taken to occur in a single step.

Assuming that $NH_2(ad)$ and $H(ad)$ adsorb and desorb at the same rate on the surface, Eq. 3.53 was simplified as follows



where A_2 represents NH_3 and $2A$ signifies the two surface sites that $NH_2(s)$ and $H(s)$ occupied. The rate of the forward reaction was given as

$$\begin{aligned} \frac{d[A(s)]}{dt} &= k_f[A_2][O(s)]^2 - k_r[A(s)]^2 \\ &= k_f[A_2]([S]_{s.s.} - [A(s)])^2 - k_r[A(s)]^2 \end{aligned} \quad (3.55)$$

Integrating the rate equation and applying the initial condition, $t = 0, [A(s)] = 0$, provides,

$$[A(s)] = \frac{(k_f k_r [A_2])^{1/2} [S]_{s.s.} \tanh\left\{(k_f k_r [A_2])^{1/2} [S]_{s.s.} t\right\}}{k_r - k_f [A_2]}. \quad (3.56)$$

The rate of the reverse reaction or desorption was considered without the forward reaction because the analyte was removed by forced flow rather than by diffusion thereby preventing the particles from adsorbing to the surface again. Hence the gas phase concentration $[A_2]$ was assumed to be negligible, yielding Eq. 3.57 from Eq. 3.55. The rate of the reverse reaction or desorption was

$$\frac{d[A(s)]}{dt} = -k_r [A(s)]^2. \quad (3.57)$$

Integrating using the initial condition, $t = 0, [A(s)] = [S]_{s.s.}$, led to

$$[A(s)] = \frac{1}{k_r t + 1/[S]_{s.s.}}. \quad (3.58)$$

Summary

The foundation for the theoretical modeling of the ammonia sensor was laid in this chapter by first presenting the relationship between thermodynamic properties and reaction kinetics. Then adsorption theory and surface reaction rate expressions were discussed, followed by a literature review of mechanisms that led to the choosing of molecular adsorption as the mechanism for the model. Finally, the reaction kinetics for molecular adsorption were mathematically formulated to be used with the experimental results presented in the next chapter.

CHAPTER 4 RESULTS AND DISCUSSION

The results from the experimental portion of this study are presented in this chapter. Throughout the course of this project, the sensor developers were continuously upgrading the performance of the field effect transistors; resultantly, three generations of sensors were used in testing. The latest versions were always utilized in the experiments. For the ammonia sensor, first presented are the response times fitted to the model to obtain rate information. Then, the performance and feasibility of the sensor for use in a laboratory animal environment are discussed. Detector reliability and sensitivity limited the useful data obtained from the carbon dioxide sensor. Consequently, for the carbon dioxide sensor, only a calibration curve, response times of the sensor, and cross-sensitivity to humidity are reported. Experiments for modeling purposes were not completed with the carbon dioxide sensor.

Drift Tests

Prior to conducting any tests with the analyte gases, the carbon dioxide and ammonia sensors were tested for drift of the baseline signal. The sensors were exposed to air at a flow rate of 2 L/min for over 40 hours. The results of these tests can be viewed in Figure 4-1. Each sensor had two channels of output offering the same signal with different amplification factors. Table 4-1 lists the rates of the signal drift. The carbon dioxide sensor had a negative drift rate, while the ammonia sensor drift rate was positive. The magnitude of the drift rate for the carbon dioxide sensor was slightly larger than for

the ammonia sensor. For both sensors the drift rate was much higher in the first five hours than for the rest of the test, which shows that the stability of the baseline increased with time. Therefore, for the following tests the sensor was turned on at least one hour before each experiment to help stabilize the baseline signal.

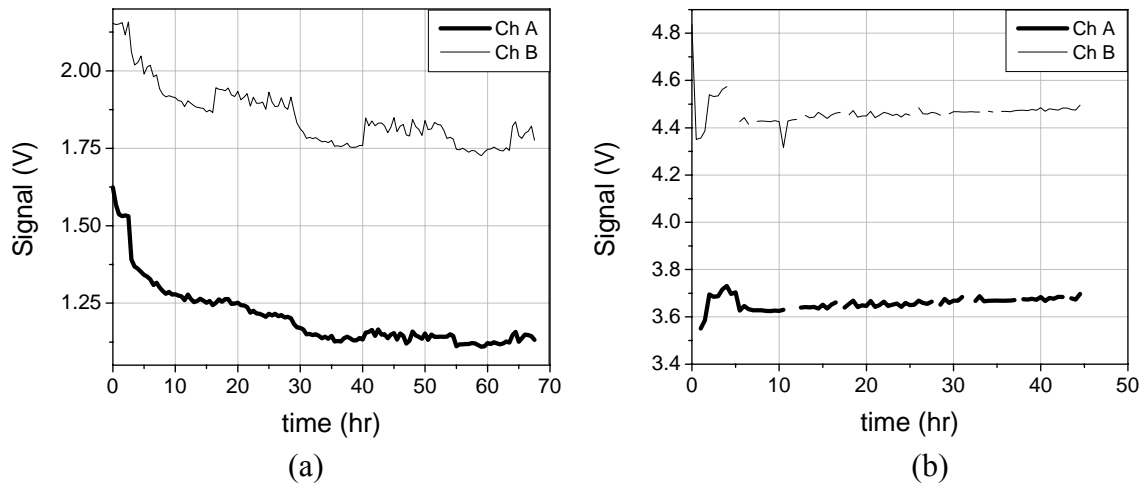


Figure 4-1 Long-term drift test results (sample size, $N = 1$) for the (a) carbon dioxide and (b) ammonia sensors. Signal output recorded every 30 minutes.

Table 4-1 Rates of baseline signal drift for the carbon dioxide and ammonia sensor exposed to air at 2 L/min for over 40 hours.

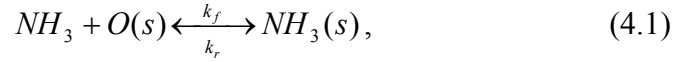
Sensor	Slope (mV/hr)	
	Channel A	Channel B
Carbon dioxide	-7.3	-5.5
Ammonia	1.8	2.6

Ammonia Sensor Results

For the ammonia sensor, first presented are the time response tests fitted to the model to obtain rate constants, the equilibrium constant, and Gibbs free energy. Second, the role of diffusion is discussed along with the presentation of time response results in the diffusion box. Third, results from tests for temperature dependency and the resulting Arrhenius parameters are presented. Finally, the performance and feasibility of the sensor for use in a laboratory animal environment are discussed.

Sensor Response and Mechanism

The reaction mechanism selected for the ammonia sensor model was molecular adsorption of ammonia on the titanium nitride surface,



where $O(s)$ is an open surface site and $NH_3(s)$ represents ammonia adsorbed on the surface. The Langmuir adsorption isotherm was used when developing the mechanism.

In conjunction with the Langmuir model, the assumptions made were

- Adsorption does not proceed beyond single layer,
- All sites are equivalent and the surface is uniform,
- Ability of a molecule to adsorb at a given site is independent of the occupation of neighboring sites.

The forward and reverse reactions were considered together to determine the rate of the forward reaction,

$$\begin{aligned} \frac{d[NH_3(s)]}{dt} &= k_f p_{NH_3} [O(s)] - k_r [NH_3(s)] \\ &= k_f [NH_3(g)] ([S]_{s.s.} - [NH_3(s)]) - k_r [NH_3(s)] \end{aligned} \quad (4.2)$$

where k_f and k_r are the forward and reverse rate constants, respectively, $[NH_3(s)]$ and $[NH_3(g)]$ are the concentrations of ammonia on the surface and in the gas phase, respectively and $[S]_{s.s.}$ is the total concentration of sites on the surface where the ammonia can adsorb at steady-state. This is different than total site density, Γ , because $[S]_{s.s.}$ varies with the free stream gas concentration. For example, the number of sites the analyte occupied was less at a lower analyte free stream concentration than at a higher analyte concentration. Solving Eq. 4.2 by integration using the initial condition: $t = 0$, $[NH_3(s)] = 0$, led to the following,

$$[NH_3(s)] = \frac{[S]_{s.s.} \left(1 - e^{(-k_f[NH_3(g)] + k_r)t}\right)}{1 + \frac{k_r}{k_f[NH_3(g)]}}. \quad (4.3)$$

The rate of the reverse reaction or desorption was considered without the forward reaction because the analyte was removed by forced flow rather than by diffusion thereby, preventing the particles from adsorbing to the surface again. Hence the gas phase concentration, $[NH_3(g)]$, was assumed to be negligible, yielding Eq. 4.4 from Eq.

4.2. The rate of the reverse reaction or desorption is

$$\frac{d[NH_3(s)]}{dt} = -k_r[NH_3(s)]. \quad (4.4)$$

Integrating using the initial condition: $t = 0$, $[NH_3(ad)] = [S]_{s.s.}$, provided the following

$$[NH_3(s)] = [S]_{s.s.} \exp(-k_r t). \quad (4.5)$$

To solve for the rate constants, the dimensionless concentration, or the fractional surface coverage, Θ , was used,

$$\Theta = \frac{[NH_3(s)]}{[S]_{s.s.}}. \quad (4.6)$$

To experimentally determine Θ , the sensor was exposed to air for 10 minutes, then 100 ppm ammonia for 10 minutes, and then air again for 10 minutes. The surface coverage for the forward reaction was calculated by dividing all data points from when gas was introduced into the system until it was removed by the maximum voltage signal. Hence the signal was normalized, yielding a scale from 0 to 1, with 1 being maximum surface coverage. Similarly for the reverse reaction, Θ was determined by dividing all data points from when gas was removed from the system by the maximum voltage signal.

The rate constants for the forward and reverse reactions were solved by curve fitting the experimental data. The reverse reaction rate constant was analyzed first because the forward reaction is a function of the reverse rate constant. For the reverse reaction the surface coverage, Θ , was plotted versus time and the following equation was used for the curve fit,

$$\Theta = ae^{bt}, \quad (4.7)$$

where the fitting parameter b yields the rate constant, $b = -k_r$. For the normalized data, ideally $a = 1$. This was typically the nominal value, (see Table 4-2) although the curve fit was not forced to a pre-exponential of unity. The desorption data with the curve fit can be seen in Figure 4-2. Based on the curve fit, the reverse reaction rate constant, k_r , is $6.43 \times 10^{-3} \text{ s}^{-1}$. The coefficients, R-squared values, and rate constants for both adsorption and desorption are listed in Table 4-2.

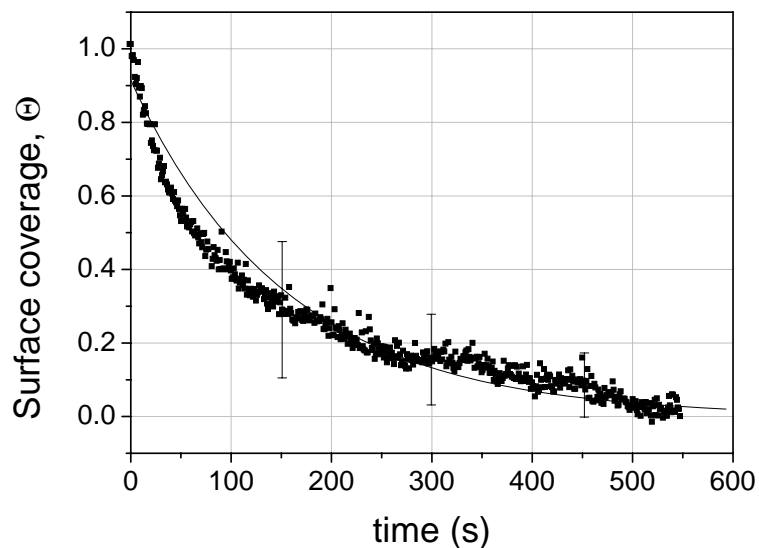


Figure 4-2 Average desorption data and curve fit for 100 ppm desorption tests. The error bars represent ± 1 standard deviation at selected data points ($N=5$).

For the forward reaction, Θ was also plotted versus time with the following equation used for the curve fit,

$$\Theta = a(1 - e^{-bt}). \quad (4.8)$$

where again a is a pre-exponential constant and $b = k_f[NH_3(g)] + k_r$. The curve fit for the adsorption data can be seen in Figure 4-3. The constant b was used to solve for k_f as follows,

$$\begin{aligned} k_f &= \frac{b - k_r}{[NH_3(g)]} \\ &= \frac{(0.04335 - 0.00643)s^{-1}}{100 \text{ ppm} \times \frac{1 \text{ mgNH}_3/L}{1 \text{ ppm}} \times \frac{1 \text{ gNH}_3}{1000 \text{ mgNH}_3} \times \frac{1 \text{ mol}}{17 \text{ gNH}_3}} \\ &= 6.28 \text{ L/mol} \cdot \text{s} \end{aligned} \quad (4.9)$$

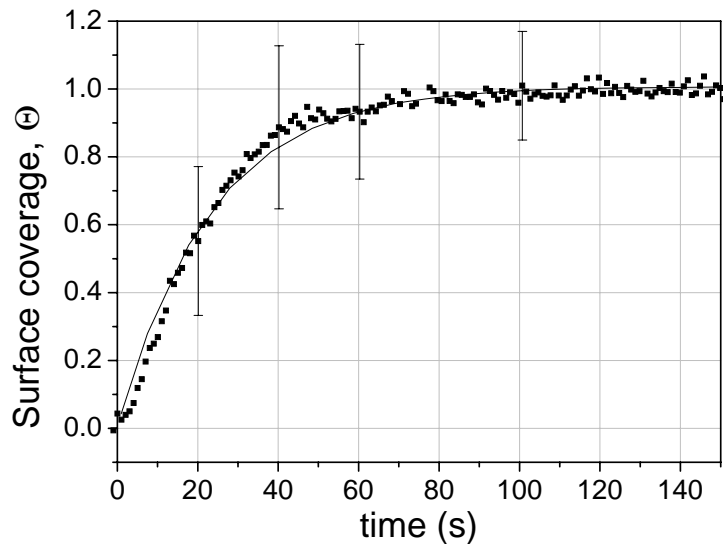


Figure 4-3 Average adsorption data and curve fit for 100 ppm adsorption tests. The error bars represent ± 1 standard deviation for 6 runs at selected data points.

Table 4-2 Curve fit coefficients, R-squared values, and rate constants for desorption and adsorption of 100 ppm ammonia on sensor.

	a	b	R ²	k
Desorption	0.915	-0.00643	0.96	$6.43 \times 10^{-3} \text{ s}^{-1}$
Adsorption	1.01	0.04335	0.99	6.28 L/mol*s

Time response experiments were also conducted at 50 ppm, where the sensor was exposed to ammonia for 10 minutes with 10 minutes of air before and after the exposure. The rate constants calculated using 100 ppm data were then used to predict the adsorption

and desorption curves at 50 ppm ammonia. The actual and predicted curves for desorption and adsorption are depicted in Figure 4-4 and Figure 4-5, respectively.

Percent error between the actual and predicted curves was calculated as follows,

$$\%Error = \frac{|Actual - Predicted|}{Predicted} \times 100\% . \quad (4.10)$$

For the desorption curve, the average percent error was 27%, where the error significantly increased as the predicted curve approached zero, which was the limit of the exponential curve fit. Neglecting the error at the limit, the average percent error from 0 – 450 seconds was 10%. The percent error for the adsorption curve was 38%, which is expected when comparing the two curves in Figure 4-5. The actual curve for 50 ppm adsorption has large standard deviations at the representative points, which may contribute to the large error seen between the actual and predicted curves. It is noted that the detection limit for the ammonia sensor is roughly 100 ppm (see below); therefore the 50 ppm data must be considered in this context.

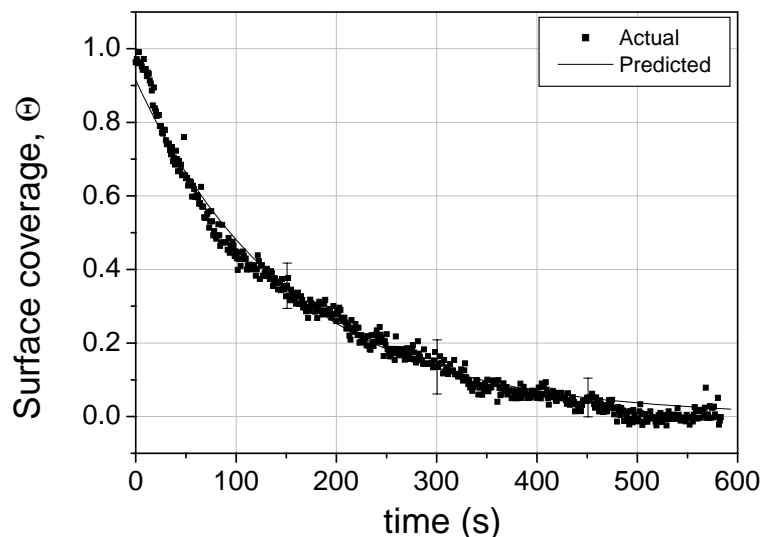


Figure 4-4 Actual 50 ppm average ($N=5$) desorption curve plotted along with the predicted curve based on the rate constant determined from 100 ppm curves. Error bars represent ± 1 standard deviation for selected data points.

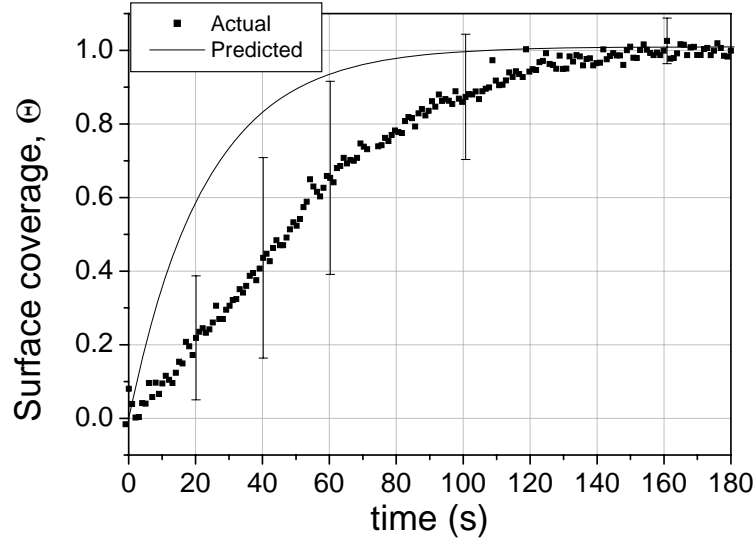


Figure 4-5 Actual 50 ppm average ($N=6$) adsorption curve plotted along with the predicted curve based on the rate constants determined from 100 ppm curves. Error bars represent ± 1 standard deviation for selected data points.

Once k_r and k_f were determined, the equilibrium concentration constant, K_c , was determined from the following,

$$\begin{aligned}
 K_c &= \frac{k_f}{k_r} \\
 &= \frac{6.28 \text{ L/mol} \cdot \text{s}}{6.43 \times 10^{-3} \text{ s}^{-1}} \\
 &= 976.7 \text{ L/mol}
 \end{aligned} \tag{4.11}$$

The equilibrium constant, K , can be calculated from the equilibrium concentration constant by,

$$\begin{aligned}
 K &= K_p \left(\frac{1}{p^o} \right)^v = K_c \left(\frac{RT}{p^o} \right)^v \\
 &= K_c \left(\frac{p^o}{RT} \right) \\
 &= \frac{976 \text{ L}}{\text{mol}} \times \frac{1 \text{ m}^3}{1000 \text{ L}} \times 1.01 \text{ bars} \times \frac{10^5 \text{ N/m}^2}{1 \text{ bar}} \\
 &\quad \times \frac{\text{mol K}}{8.315 \text{ J}} \times \frac{1}{304 \text{ K}} \times \frac{1 \text{ J}}{1 \text{ N} \cdot \text{m}} \\
 &= 39.04
 \end{aligned} \tag{4.12}$$

where p° is standard pressure and $\nu = -1$ for molecular adsorption. Also at equilibrium,

$$K = \exp(-\Delta_r G^\circ / RT) \quad (4.13)$$

where $\Delta_r G^\circ$ is the standard Gibbs energy of reaction, R is the ideal gas constant, and T is the surface temperature of the sensor. Therefore, $\Delta_r G^\circ$ was calculated as follows,

$$\begin{aligned} \Delta_r G^\circ &= -RT \ln K \\ &= -8.31 \frac{J}{mol \cdot K} \times 304K \times \ln 39.04. \\ &= -9.26 kJ/mol \end{aligned} \quad (4.14)$$

In comparison, the standard Gibbs energy of reaction for ethylene hydrogenation on platinum is -148.2 kJ/mol and for ammonia synthesis on iron it is 62.0 kJ/mol (60).

The Gibbs energy of reaction predicts the direction of spontaneous change of a reaction at constant temperature and pressure. The reaction Gibbs energy is also defined as the slope of the graph of the Gibbs energy plotted against the extent of the reaction, ξ :

$$\Delta_r G = \left(\frac{\partial G}{\partial \xi} \right)_{p,T}, \quad (4.15)$$

and it is further derived as the difference between the chemical potentials, μ , of the reactants and products at the composition of the reaction mixture,

$$\Delta_r G = \mu_{products} - \mu_{reactants}. \quad (4.16)$$

Due to the fact that the chemical potentials vary with the composition, the slope of the plot of Gibbs energy against extent of reaction varies as the reaction continues (Figure 4-6). Further, because the reaction proceeds in the direction of decreasing G , it is apparent that the forward reaction is spontaneous when $\mu_{reactants} > \mu_{products}$ or $\Delta_r G < 0$. The reverse reaction is spontaneous when $\mu_{products} > \mu_{reactants}$, $\Delta_r G > 0$, whereas the system is at equilibrium when $\mu_{products} = \mu_{reactants}$, $\Delta_r G = 0$. Since $\Delta_r G < 0$ for the reaction of

ammonia on the titanium nitride surface, the forward reaction, ammonia adsorption, is spontaneous.

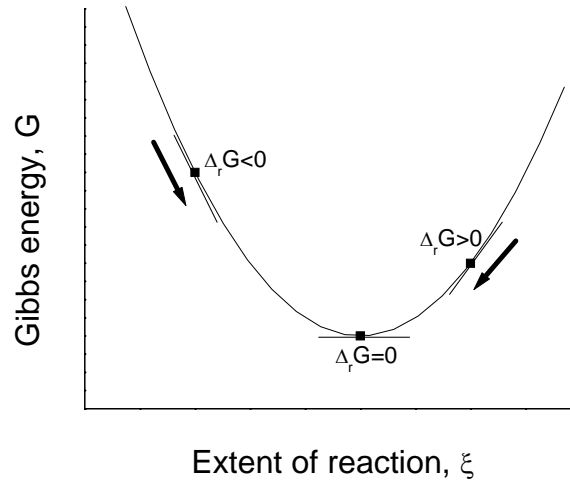


Figure 4-6 The slope of the Gibbs energy changes as the reaction proceeds. The arrows indicate the direction in which the reaction spontaneously proceeds. The reaction is at equilibrium when the curve is at its minimum.

Diffusion

Time response tests were also completed in the diffusion box to aid in understanding the role diffusion played in the sensor's response to ammonia. In the forced flow case, the ammonia in the gas phase was a constant because the distance from the surface to the free stream was not large enough to create a space or time gradient. However, the diffusion case can be modeled as a semi-infinite medium, as illustrated in Figure 4-7, which allows the gas phase ammonia to be a function of x and t .

The mathematical formulation of the gas phase ammonia is given as

$$[NH_3(g)] = f(x, t) \quad \text{in} \quad 0 < x < \infty, \quad t > 0, \quad (4.17)$$

with the following boundary conditions:

$$[NH_3(g)] = [NH_3]_{in} \quad \text{as} \quad x \rightarrow \infty, \quad t > 0, \quad (4.18)$$

$$\frac{\partial [NH_3(ad)]}{\partial t} = k_f [S] \frac{\partial}{\partial t} \left(\frac{\partial [NH_3(g)]}{\partial x} \right) - k_r [NH_3(ad)] \quad \text{at} \quad x = 0, \quad t > 0. \quad (4.19)$$

The second boundary condition, at $x = 0$, describes the overall rate of the surface reaction described in Eq. 4.1, for the diffusion case. The rate of the overall reaction now becomes a partial derivative due to the presence of the space and time gradients with respect to the ammonia gas. The solution cannot be obtained analytically due to the coupled nature of the equation; numerical methods such as finite difference must be employed to solve this problem. The solution of Eq. 4.1 was not within the scope of this investigation, but was considered because the main mode of mass transfer in a laboratory animal cage will be diffusion.

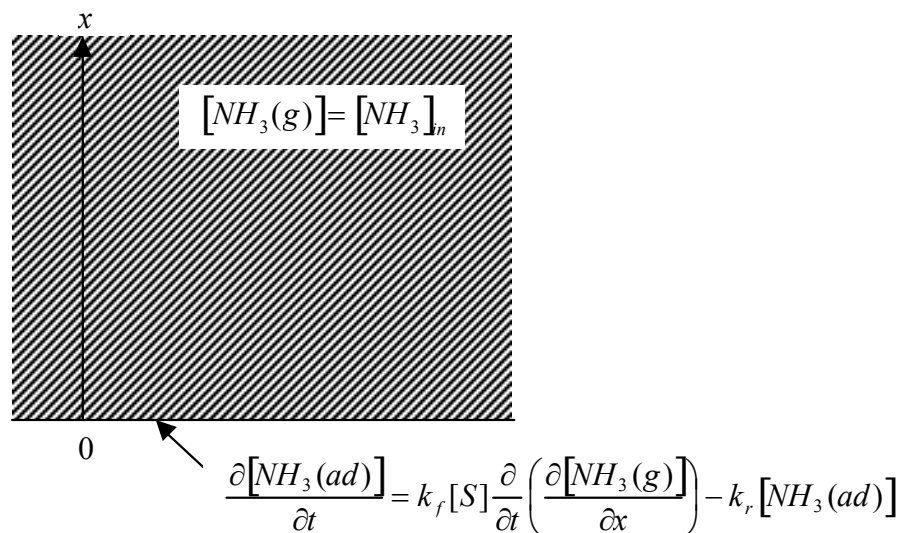


Figure 4-7 Diffusion of ammonia in a semi-infinite region.

To determine the time response for the diffusion case, the sensor was exposed to 100 ppm ammonia for 10 minutes, with 10 minutes of air before and after exposure. The desorption and adsorption results are plotted along with the forced curves in Figure 4-8 and Figure 4-9, respectively.

The time constants for the diffusion case are listed in Table 4-3. As is evident from Figure 4-8 and Figure 4-9, the diffusion time constants were much greater than for the

forced flow regime. For desorption, the percent difference in time constants relative to the forced condition was 27%. In the case of adsorption, the percent difference was 67%.

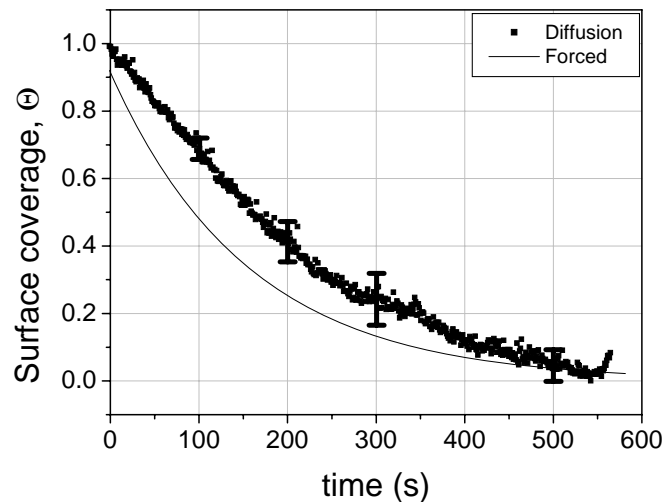


Figure 4-8 Average ($N=6$) desorption curve for the diffusion case compared with the forced curve fit for 100 ppm data. Error bars represent ± 1 standard deviation for select data points.

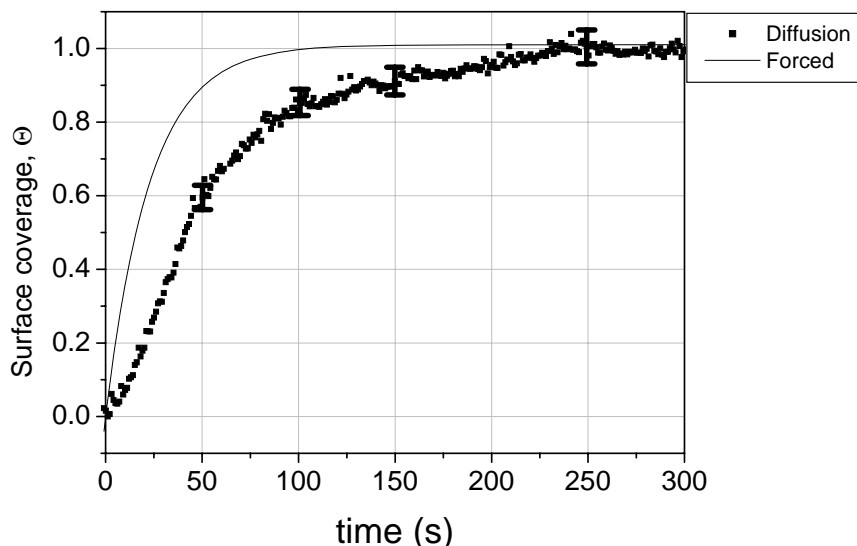


Figure 4-9 Average ($N=6$) adsorption curve for the diffusion case compared with the forced curve fit for 100 ppm data. Error bars represent ± 1 standard deviation for select data points.

Temperature Effects

The sensor was exposed to ammonia for 10 minutes at 31°C (1.0 V), 39°C (2.0 V) and 52°C (3.0 V), where the voltage corresponded to a calibrated temperature – voltage

curve and was altered by a DC power supply. The adsorption and desorption time response plots for 31°C (1.0 V) were shown previously in Figure 4-4 and Figure 4-5, respectively. The rate constants calculated from 100 ppm data were established as the accepted rate constants at 1.0 V.

Table 4-3 Adsorption and desorption time constants for the ammonia sensor using forced and diffusion flow regimes.

Reaction	Flow	a	b	R ²	Time Constant, $\tau = 1/b$ (s)
Adsorption	Forced	1.01	0.043	0.99	23.3
	Diffusion	1.02	0.014	0.95	71.4
Desorption	Forced	0.915	0.00643	0.96	156
	Diffusion	1.00	0.00465	0.98	215

The results and respective curve fits for 39°C (2.0 V) and 52°C (3.0 V) data are plotted in Figure 4-10. Rate constants for 39°C (2.0 V) and 52°C (3.0 V) data were determined from curve fits, where the equations used for curve fitting desorption and adsorption plots were $\Theta = ae^{bt}$ and $\Theta = a(1 - e^{-bt})$, respectively. The curve fit coefficients, R-squared values, rate constants, and equilibrium concentration constants for all three temperatures are compiled in Table 4-4. For both the forward and reverse reactions the rate constants decreased with increasing temperature. The equilibrium concentration constant increased with increasing temperature. From the Langmuir adsorption model this result is counterintuitive. The desorption rate is expected to increase with increasing temperature. In the experiments, Θ was defined as $[NH_3(s)]/[S]_{s.s.}$, when to compare temperature effects the fractional surface coverage should really be $[NH_3(s)]/[S]_{max}$ where $[S]_{max}$ is the absolute number of sites where ammonia can adsorb for a particular isotherm. If the latter fractional surface coverage is used, a result which follows the Langmuir model may be found.

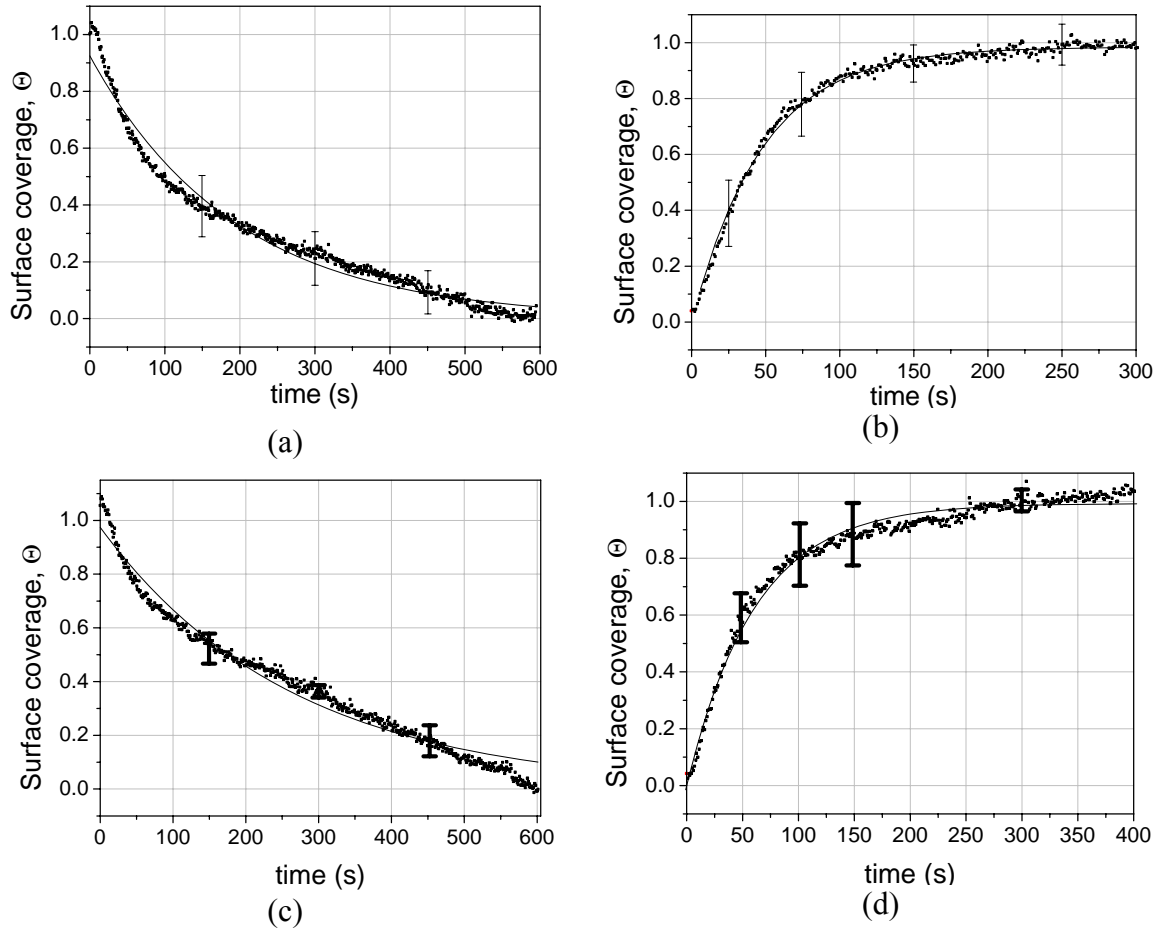


Figure 4-10 Average desorption and adsorption curves at 50 ppm ammonia for heater voltages of (a) – (b) 2 V ($N=10$) and (c) – (d) 3 V ($N=7$ and $N=8$). Error bars represent ± 1 standard deviation for select data points.

Table 4-4 Curve fit coefficients, R-squared values, and rate constants for desorption and adsorption of ammonia on sensor at varying surface temperatures.

Reaction	Temp. (K)	Heater Voltage (V)	Curve fit coefficients			k_f (L/mol*s)	k_r (s^{-1})	K_c (L/mol)
			a	b	R^2			
Desorption	304	1.0	0.915	-0.00643	0.96		6.43×10^{-3}	976
	312	2.0	0.925	-0.00521	0.97		5.21×10^{-3}	1032
	325	3.0	0.974	-0.00378	0.97		3.78×10^{-3}	1132
Adsorption	304	1.0	1.01	0.04335	0.99	6.28		
	312	2.0	0.984	0.02104	0.99	5.38		
	325	3.0	0.993	0.01638	0.98	4.28		

Sensor Performance

Single analyte tests, where air and ammonia were the only gases in the flow stream, were conducted on the ammonia sensor to establish a calibration curve. Seeing as the ammonia threshold limit value for a laboratory animal cage is 25 ppm, the sensors were

tested at concentrations of 25, 50, 75, and 100 ppm. The sensor was exposed to the set concentration for 10 to 20 minutes with a minimum of 10 minutes of air between analyte exposures. For the forced flow case, 10 minutes of purging with air was a sufficient amount of time to remove ammonia from the system.

Figure 4-11 shows a sample of single analyte tests with six exposures to 100 ppm and three exposures to 50 ppm ammonia. From the raw signal, Figure 4-11(a), it was difficult to determine the magnitude of the response due to the significant drift of the baseline signal. To correct for the baseline drift, the average of 30 data points before gas introduction into the system and 30 data points after gas removal were used to determine a slope for baseline drift. Then the slope was subtracted from every data point along the curve to give the baseline corrected data in Figure 4-11(b). From Figure 4-11(a), it is evident that the sensor responds to ammonia, but Figure 4-11(b) illustrates that the magnitude of the signal was not consistent. For the 100-ppm pulses the response varied from 20 to 50 mV. Additionally, four of the 100-ppm pulses were of the same magnitude as the 50-ppm pulses.

The calibration curve for all of the single analyte tests can be seen in Figure 4-12. The average response and respective standard deviation to exposures of 25, 50, 75, and 100 ppm along with a linear fit is plotted. The linear fit has an R-squared value of 0.85. Although the R-squared value is statistically high, the error bars for the 75 and 100-ppm data are greater than the slope of the linear fit. For this concentration range, the sensor cannot accurately predict the ammonia concentration. From Figure 4-12 a level of detection (LOD) was calculated in order to determine if the testing was completed in the sensor's operating range. The LOD was calculated as follows,

$$LOD = \frac{2\sigma}{m}, \quad (4.20)$$

where σ is the standard deviation and m is the slope of the linear curve fit. With a standard deviation of 0.005 and a slope of 7.78×10^{-5} , the level of detection for the ammonia sensor was found to be approximately 100 ppm.

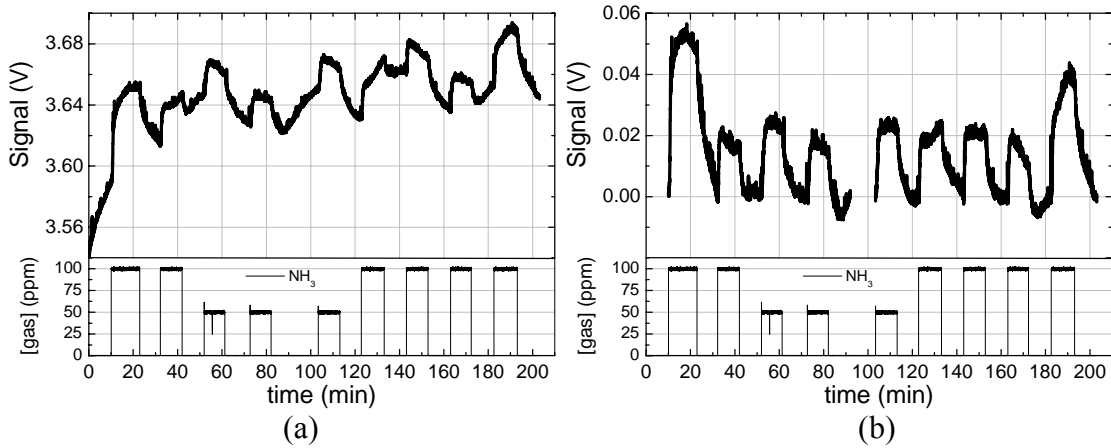


Figure 4-11 Single analyte test results ($N=1$) for the ammonia sensor: (a) raw data and (b) baseline corrected.

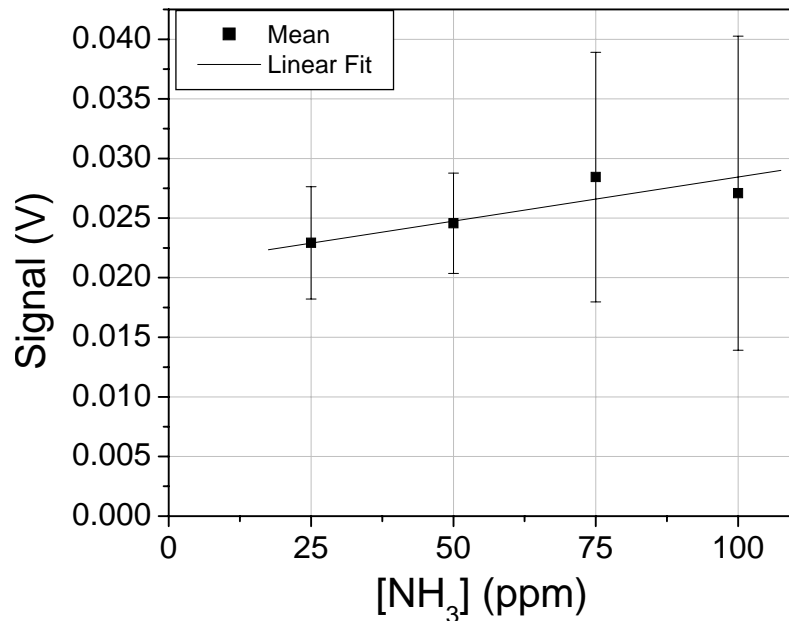


Figure 4-12 Calibration curve and linear fit for ammonia sensor. The error bars represent \pm one standard deviation for two to six runs.

Gradual ramping tests

While the single analyte tests in forced flow were useful to obtain response data, in actual operation the sensor will not have sudden increases and decreases in ammonia concentration. Therefore, to imitate the gradual changes seen in the cage environment tests were conducted where the ammonia concentration was ramped up or down at five-minute intervals.

The gradual ramping tests completed in the diffusion box are depicted in Figure 4-13. Figure 4-13(a) illustrates the response to 200 ppm ammonia, followed by a gradual decrease to zero concentration, and then back to 200 ppm. Figure 4-13(b) depicts a gradual ramp to 200 ppm and then a gradual decrease back to 0 ppm. Local maximums and minimums are labeled on the curves in Figure 4-13 and the slopes for the signal change over concentration change for each segment are tabulated in Table 4-5. Segments A – B and E – F, where the concentrations were increasing, have comparable slopes, 0.25 and 0.23 mV/ppm, respectively. The slope for segment C – D was expected to be similar to the aforementioned slopes, however it's slope of 0.15 mV/ppm was closer to the slopes for the decreasing ramps. The decreasing ramps, segments B – C and F – G, had slopes of 0.11 and 0.13 mV/ppm, respectively. These two smaller slopes indicate that the ammonia may not have completely diffused out of the box to the desired input concentration. Therefore when more ammonia was added it increased the concentration that was already in the box. To better estimate the concentration at point C, the voltage difference from B – C was divided by the slope from A – B. This resulted in a difference of 80 ppm from B – C or a total concentration of 120 ppm at point C. The same theory was applied to better estimate the concentration at point D. The change in concentration from C – D was calculated as 116 ppm and adding it to 120 ppm from point C resulted in

a concentration of 236 ppm at point D. Since the segment C – D directly followed a decrease in concentration the slope may have been affected by residual ammonia left in the system.

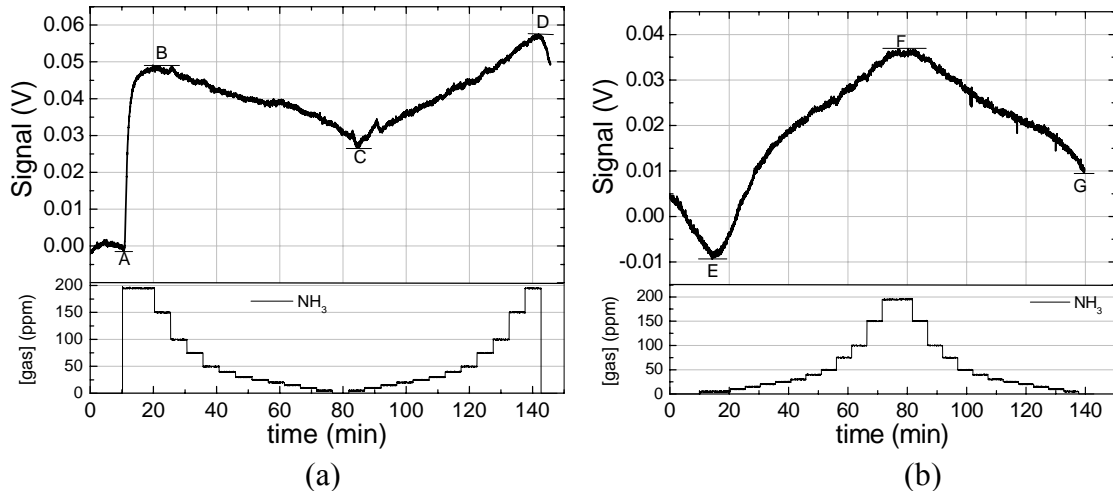


Figure 4-13 Ammonia concentration ramped up and down with ammonia sensor in diffusion box (a) average ($N=6$) ramp down and (b) average ($N=6$) ramp up. The local maximums and minimums are labeled on each curve as (A) – (G).

Further proof of the slow diffusion process is that there was a five-minute lag time at lower concentrations in both Figure 4-13(a) and Figure 4-13(b). The five-minute lag is more apparent in Figure 4-13(b) where the sensor does not respond to ammonia until 20 minutes of testing when the concentration is increased from 5 to 10 ppm. Two conclusions can be drawn from these results; either the sensor does not respond to concentrations less than 10 ppm or the exposure time of 10 minutes was not long enough for the sensor to respond to the low concentration. Given the LOD, it is concluded that 20 ppm is not a valid level statistically. Based on earlier tests, 10 minutes should be sufficient time.

Baseline drift was significant for both tests. If an observer did not know what the concentration of ammonia was, the changes in voltage could be from 1) changes in

ammonia concentration, 2) baseline drift, or 3) changes in relative humidity, as will be shown next.

Table 4-5 Slopes for ramp down and ramp up curves completed in diffusion box.

Graph Segment	Signal (mV)		[NH ₃] (ppm)		Slope (mV/ppm)
	1	2	1	2	
A – B	0	47.8	0	195	0.25
B – C	47.8	27.5	195	5	0.11
C – D	27.5	56.6	5	195	0.15
E – F	-8.8	35.4	5	195	0.23
F – G	35.4	10.3	195	0	0.13

Cross-sensitivity to humidity and carbon dioxide

The ammonia sensor was tested for cross-sensitivity to humidity through two different experiments. In the first set of experiments the sensor was exposed to humidified air in the absence of ammonia. The humidity was increased to 40 – 60% rh three times for 20 minutes each with 20 minutes of dry air between each cycle. For the second set of experiments, the ammonia was increased to 50 or 100 ppm ammonia in dry air, followed by the same cycle in humidified air. The results of both experiments are illustrated in Figure 4-14 and Figure 4-15, respectively.

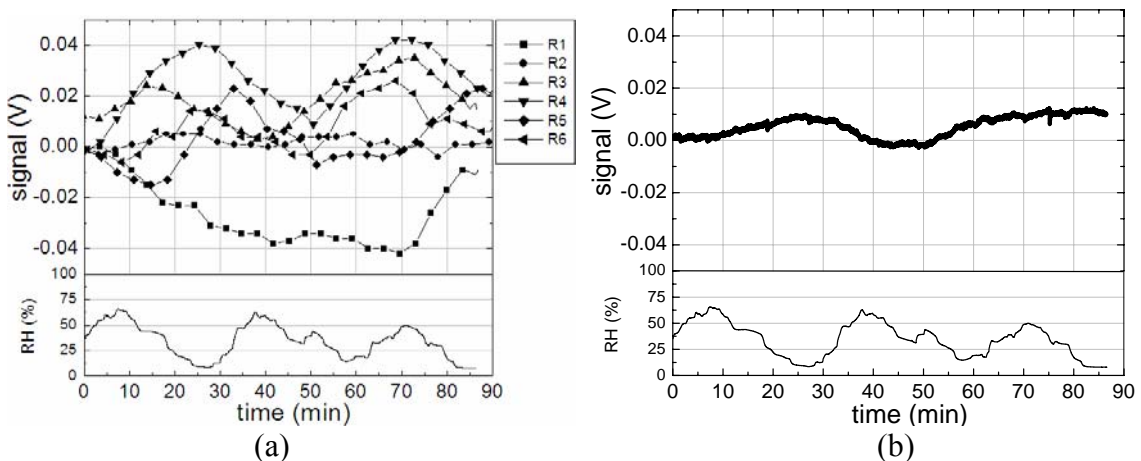


Figure 4-14 Ammonia sensor tested for cross-sensitivity to humidity (a) six individual tests and (b) average of 6 runs. Tests were completed in the absence of ammonia.

Figure 4-14(a) shows the results of all six tests completed in the absence of ammonia. The average response is shown in Figure 4-14(b). From these six tests it is evident that there was no correlation between signal response and changes in relative humidity. Any changes in signal were from sensor instability and drift of the baseline.

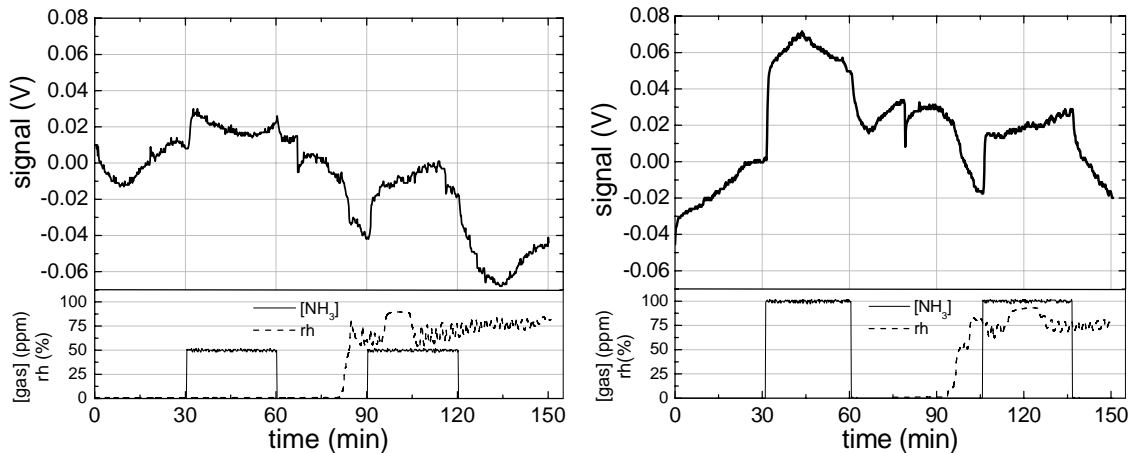


Figure 4-15 Ammonia sensor tested for cross-sensitivity to humidity with ammonia in the system at two different concentration levels: (a) 50 ppm and (b) 100 ppm.

Figure 4-15(a) and Figure 4-15(b) depict the cross-sensitivity to humidity at 50 and 100 ppm ammonia, respectively. The magnitudes of the sensor response to changes seen in Figure 4-15 are listed in Table 4-6. A response to changes in ammonia for both dry and humid air was seen. The magnitudes for adsorption varied from 12 to 60 mV. For desorption, the magnitudes varied from -13 to -55 mV. The magnitude of the response was not dependent on the relative humidity of the air. The sensor also responded to an increase in relative humidity with a decrease in signal of -30 to -40 mV. This response was similar in magnitude and direction to the ammonia desorption response.

Since the sensor responded to relative humidity only when ammonia was recently in the system, the change in signal could be attributed to the water molecules removing residual ammonia from the surface. This competition between water and ammonia for available surface sites provides further evidence to rule out the ammonia and hydroxide

mechanism where the water acted as the vehicle for the sensor to respond to the ammonia. Notably, above 10% the sensor does not respond with the same magnitude as when the humidity increases from 2 to 50%. The relative humidity operating range in a laboratory animal cage is between 30 to 70% (18). Therefore the work function change seen when going from dry to humid air should not hinder the sensor in detecting ammonia.

Table 4-6 Magnitude of signal response for changes in ammonia concentration and relative humidity.

Description	Signal Change (mV)
0 to 50 ppm, dry air (2% rh)	+12
0 to 50 ppm, humid air (50% rh)	+32
0 to 100 ppm, dry air	+60
0 to 100 ppm, humid air	+36
100 to 0 ppm, dry air	-43
100 to 0 ppm, humid air	-37
50 to 0 ppm, dry air	-13
50 to 0 ppm, humid air	-55
0 to 60% rh with previous exposure to 50 ppm NH ₃	-30
0 to 80% rh with previous exposure to 100 ppm NH ₃	-40

Next the ammonia sensor was tested for cross-sensitivities to humidity and carbon dioxide with ammonia in the system. The introduction of each new parameter was at least 10 minutes after the last change in experimental conditions to ensure that the effect on the sensor was from the intended parameter. Figure 4-16 illustrates the average results of this test. The sensor responded to ammonia similarly to previous tests in dry air.

Upon the introduction of carbon dioxide, at 35 minutes, the signal experienced a sudden spike. At 90 minutes, when the carbon dioxide increased from 3000 to 5000 ppm, the signal again spiked. No change in response was apparent when the carbon dioxide concentration decreased at 150 minutes. The sensor responded to humidity as previously

discussed, where the signal decreased when the humidity went from dry to humid. Additionally, the signal increased when the air went from humid to dry, which further supports the theory that water and ammonia are competing for sites on the sensor surface.

Carbon Dioxide Sensor Results

Single analyte (i.e. carbon dioxide in dry air), time response, and cross-sensitivity to humidity tests were completed for the carbon dioxide sensor. For the single analyte tests, at each concentration level the sensor was exposed to the specified carbon dioxide concentration for 10 to 30 minutes and the signal was collected every 10 seconds. Raw data for one of the single analyte tests, where the sensor was exposed to 300, 1000, 2500, and 5000 ppm of carbon dioxide, can be seen in Figure 4-17.

When creating the calibration curve, the baseline of each signal was set to 1.00 thereby normalizing the curve to ensure that the signal responses were comparable. To eliminate the transient response from the calibration, the first two minutes of data were not used when calculating the averages shown in Figure 4-18.

The carbon dioxide sensor responded to changes in gas concentration with a decrease in voltage. For concentrations of 300 and 1000 ppm, the signal changed by 60 and 74 millivolts (mV), respectively. There was a 130 mV change in signal for a change in gas concentration at 2500 ppm. The change in signal at 3000 ppm was 90 mV, which was less than the response at 2500 ppm. These data were taken from a different channel than the others and consequently the amplification of the signal was slightly less than the others. At 5000 and 7100 ppm, the signal changed by 150 and 200 mV, respectively. A linear fit of the data was conducted with an R-squared value of 0.88.

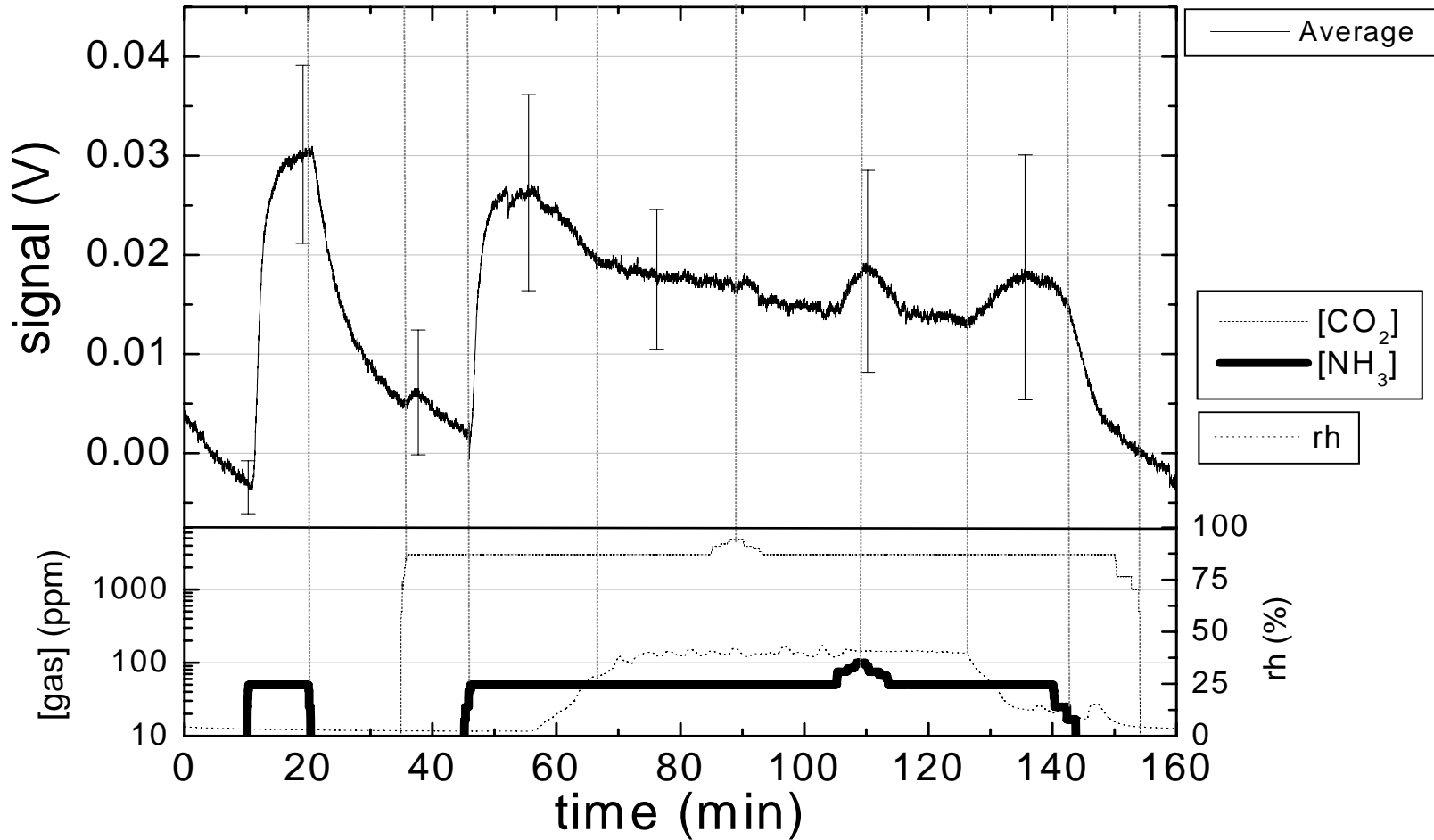


Figure 4-16 Average (N = 6) ammonia sensor response to humidity, carbon dioxide, and ammonia concurrently. Error bars represent ± 1 standard deviation for select data points.

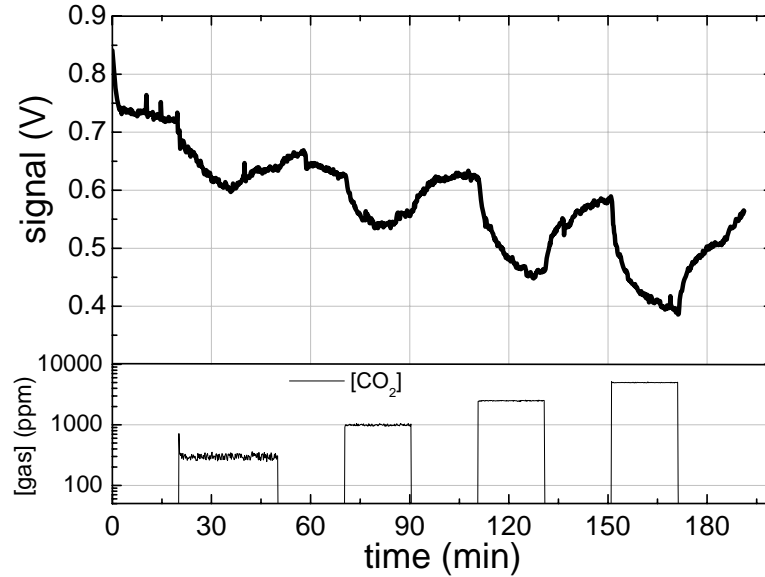


Figure 4-17 Raw data ($N=1$) from carbon dioxide single analyte test, where baseline drift has not been eliminated. Signal was collected every 10 seconds.

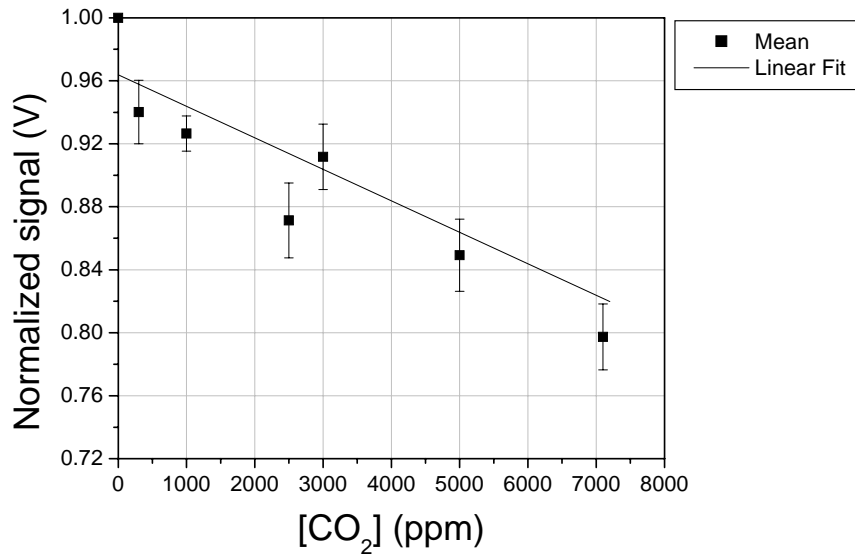


Figure 4-18 Calibration curve for carbon dioxide sensor. The error bars represent \pm one standard deviation.

Figure 4-19 depicts the transient response of the sensor to introduction and removal of gas from the flow stream. Each curve is an average of four tests with the standard deviation plotted at several points along the curve. For each test the baseline was established for 30 minutes by running dry air through the system, then the sensor was exposed to 3000 ppm of carbon dioxide for 30 minutes, and finally the system was

flushed out with dry air for 15 minutes. The curves have been normalized on a scale from zero to 1.00, where zero is the baseline and 1.00 is the maximum change in signal for the sensor. For the introduction of gas, or adsorption process, the sensor reaches 95% of the maximum in 16.4 minutes. When the carbon dioxide is removed, or desorption process, the sensor returns to 5% of the baseline signal in 8 minutes.

A similar time response test was completed in a humidified air stream and the results are shown in Figure 4-19(c)-(d). The average response of the sensor to the introduction of gas into the humidified air stream reaches a maximum of 90% in 15 minutes. Each individual curve reaches 1.00 at some point, but even after 30 minutes, the average does not stabilize to the normalized maximum. For the desorption process, the sensor reaches 5% of the baseline signal in 9.5 minutes.

A curve fit was conducted for each of the plots in Figure 4-19. The equation used to curve fit the adsorption plots was $\Theta = a(1 - e^{-bt})$, where Θ is the normalized signal and $1/b$ is the time constant, τ . For the desorption plots, the equation $\Theta = ae^{-bt}$ was used. The time constants for the adsorption and desorption graphs are listed in Table 4-7 and Table 4-8, respectively. Also listed in Table 4-7 and Table 4-8 for comparison are time constants for the ammonia sensor. The adsorption time constant in 50% relative humidity, 83.3 s, was smaller than for dry air at 200 s. However, with a lower R-squared value of 0.79 the uncertainty of the humid adsorption time constant is higher. For desorption, the humid time constant is greater than in dry air, but the two values are closer to each other than were the adsorption time constants. The time constants for the carbon dioxide and ammonia sensors are on the same order of magnitude.

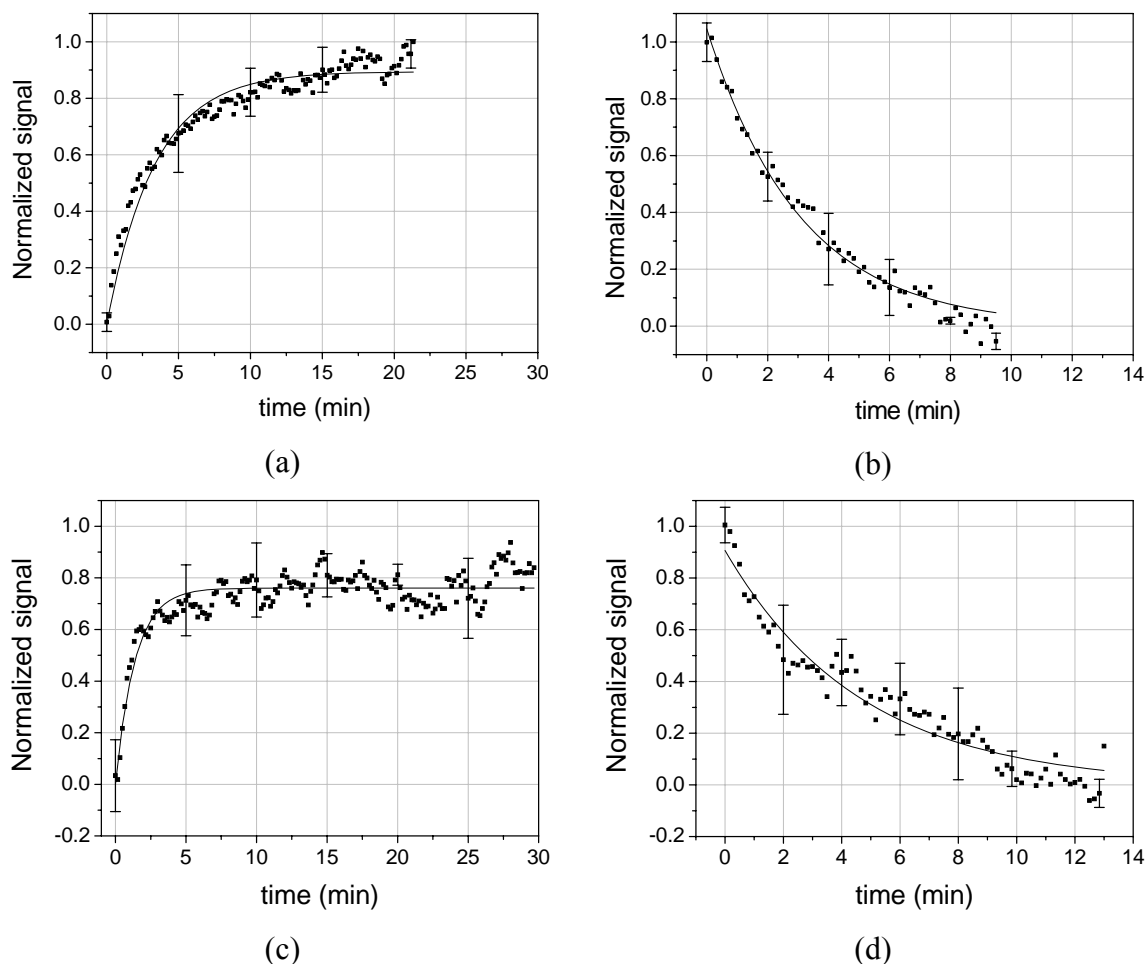


Figure 4-19 The average ($N=4$) response time and respective curve fits of the carbon dioxide sensor to (a) adsorption and (b) desorption in dry air, < 2% relative humidity, (c) adsorption and (d) desorption in humid air, 50% rh. The error bars represent ± 1 standard deviation for selected data points.

Figure 4-20 illustrates the test for cross-sensitivity to humidity. Three tests were used to establish the mean curve. For each test the procedure was as follows: 30 minutes dry air, 30 minutes of 3000 ppm carbon dioxide, 15 minutes dry air, 15 minutes humid air, 30 minutes of 3000 ppm carbon dioxide in a humid air stream, and 30 minutes of humid air. Under dry conditions the maximum change in signal to 3000 ppm carbon dioxide was 140 mV, while in humid air the signal only changed by 80 mV. Another important result is that when the relative humidity changed from less than 10% (dry) to 60% (humid), the sensor registered a 230 mV increase; it responded as if the carbon

dioxide concentration was decreasing. The same phenomenon was seen with the ammonia sensor and can be attributed to residual analyte on the surface, where when the humidity is increased the water molecules compete with the analyte for adsorption sites. The change in signal is due to the water molecules removing the residual analyte from the surface.

Table 4-7 Adsorption time constants. Equation used for curve fitting was $\Theta = a(1 - e^{-bt})$.

Sensor	Flow	Relative Humidity (%)	Gas concentration (ppm)	a	b	R ²	Time Constant, $\tau = 1/b$ (s)
CO ₂	Forced	2	3000	0.89	0.005	0.95	200
CO ₂	Forced	50	3000	0.76	0.012	0.79	83.3
NH ₃	Forced	2	100	1.01	0.043	0.99	23.3
NH ₃	Diffusion	2	100	1.02	0.014	0.95	71.4

Table 4-8 Desorption time constants. Equation used for curve fitting was $\Theta = ae^{-bt}$.

Sensor	Flow	Relative Humidity (%)	Gas concentration (ppm)	a	b	R ²	Time Constant, $\tau = 1/b$ (s)
CO ₂	Forced	2	3000	1.04	0.00543	0.98	184
CO ₂	Forced	50	3000	0.91	0.00350	0.93	286
NH ₃	Forced	2	100	0.915	0.00643	0.96	156
NH ₃	Diffusion	2	100	1.00	0.00465	0.98	215

Fortunately above 10%, for minor fluctuations in humidity, the sensor does not respond with the same magnitude as when changing from dry to humid air. Since the guideline for laboratory animal cage relative humidity levels is between 30 to 70%, the significant work function change seen when going from dry to humid air should not hinder the sensor in detecting carbon dioxide.

Summary

Experimental results for the carbon dioxide and ammonia sensors were presented and discussed in this chapter. The theoretical model was used with the experimental

results to determine rate constants, the equilibrium constant, and Gibbs free energy for the molecular adsorption of ammonia on a titanium nitride surface. A mathematical formulation and experimental results for the diffusion flow regime were presented and found to be comparatively slower than for the forced flow.

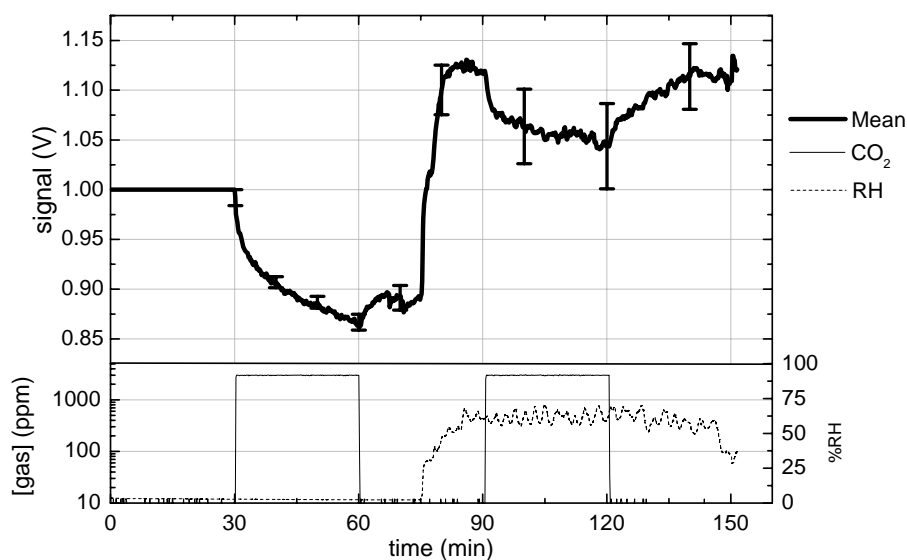


Figure 4-20 Carbon dioxide sensor tested for cross-sensitivity to humidity. The error bars represent ± 1 standard deviation for 3 runs at selected data points.

CHAPTER 5 SUMMARY AND CONCLUSIONS

Summary of Results

There were two main goals for this project. The first goal was to assess the feasibility of applying ammonia and carbon dioxide sensors for monitoring laboratory animal cages through single analyte, time-response, and cross-contamination experiments. The second goal was to theoretically model the chemical kinetics and heterogeneous chemistry of the reaction on the ammonia sensor by defining the reaction mechanism, determining adsorption and desorption rates and rate constants, determining the equilibrium constant, and exploring the role of diffusion.

Ammonia Sensor

Sensor response and mechanism

The mechanism that was best supported by the literature and the experiments was molecular adsorption of ammonia on a titanium nitride surface. Resulting adsorption and desorption reaction rate equations were formulated and time response tests were completed and compared with the model. Curve fits were completed for response time tests using 100 ppm ammonia in dry air (2% rh). From the experimental data, the forward and reverse rate constants were evaluated as $6.28 \text{ L mol}^{-1}\text{s}^{-1}$ and $6.43 \times 10^{-3} \text{ s}^{-1}$, respectively. The rate constants from the 100 ppm data were used to predict adsorption and desorption curves for 50 ppm data. Time response experiments were also conducted at 50 ppm, where the error between the actual and predicted curves for adsorption and desorption was 38% and 10%, respectively. The equilibrium concentration constant was

determined to be 976.7 L/mol. The equilibrium constant was calculated as 39.04, which was used to determine the standard Gibbs energy of reaction, -9.25 kJ/mol. From the equilibrium constants and the Gibbs energy of reaction it was determined that the forward reaction would occur spontaneously.

Time response tests were also completed using diffusion dominated delivery to aid in understanding the role diffusion played in the sensor's response to ammonia. The diffusion time constants were markedly more than for the forced flow regime. For desorption, the diffusion time constant was 67% more than the forced time constant, while for adsorption it was 27% more. The diffusion case was also mathematically formulated as a semi-infinite medium where the gas phase ammonia concentration was a function of space and time.

To examine temperature effects, time response experiments were completed at three different temperatures. For both the forward and reverse reactions the rate constants decreased with increasing temperature. The equilibrium constant increased with increasing temperature.

Performance and feasibility

The ammonia sensor responded to changes in ammonia concentration. However, the calibration curve for the ammonia sensor showed that standard deviation for the response to 100 ppm was comparably higher than the total slope of the calibration curve, essentially yielding a detection limit of approximately 100 ppm. In future applications, where the concentration is not pre-determined, it would be difficult to accurately predict the ammonia concentration at levels below 100 ppm. Further, when the sensor is used in a laboratory animal cage, where the air quality is unknown, changes in signal could be

from changes in ammonia concentration, changes in relative humidity, or drift of the baseline signal.

When the sensor was exposed to dramatic changes in relative humidity, from 2 to 60%, the sensor responded as though more ammonia was being desorbed from the system. This phenomenon only occurred when ammonia was present in the gas stream or if it had recently been in the system, approximately 10 minutes before humidity increased. If ammonia was not present, then the signal from the sensor did not change when the humidity increased. The sensor's cross-sensitivity to humidity not only played into feasibility of using the sensor for this application, but also offered insight into the mechanism for the model, where the ammonia and water compete for open surface sites. As for cross-sensitivity to carbon dioxide, it caused a transient spike in the signal when it was introduced into the system.

Carbon Dioxide Sensor

The carbon dioxide sensor responded to changes in carbon dioxide concentration with a decrease in voltage of 60 to 200 mV for concentration changes of 300 to 7000 ppm, respectively. A calibration curve of signal versus carbon dioxide concentration was established with a linear curve fit ($R\text{-squared} = 0.88$). If the concentration is unknown, as will be the case in actual operation in a laboratory animal cage, it would be difficult to accurately determine the absolute value of carbon dioxide concentration based on the established calibration curve.

The transient response of the sensor to addition and removal of analyte was evaluated in dry and humid air. Fifteen to sixteen minutes was the average response time to the introduction of the analyte, while 8 – 9 minutes was the average response time to removal of the analyte under forced flow conditions. For adsorption the signal was at

50% of the maximum at 2.8 minutes, while the half-life for desorption was 2 minutes. In a laboratory animal cage, these would be sufficient response times for two reasons. First, the cages are not expected to experience rapid increases in carbon dioxide concentration. If the concentration does increase it is expected to do so gradually over hours or even days. Therefore the sensor's response time of 15 – 16 minutes would give sufficient time to monitor gradual changes. Second, if the carbon dioxide concentration were to rapidly increase, such as in the case where a ventilated cage would lose its air supply due to a power failure, a 50% change would be seen in 2 – 3 minutes, which would provide ample time to react to the situation and prevent the animals from overexposure to carbon dioxide.

The carbon dioxide sensor was sensitive to changes in relative humidity, especially when the air went from dry (2%) to humid (50%). Additionally, the magnitude of the response to carbon dioxide was reduced when the air was humid with a 40% reduction in signal response between dry and humid air. According to the Guide (18), the cage must be held between 30 – 70% relative humidity, so the cage will not change rapidly from 2 – 50%. The cross-sensitivity to water vapor and the smaller response in humid air leads to the same conclusion as for the ammonia sensor, as noted above, the water vapor competes with the analyte for open surface sites.

Recommendations

At the current development stage, these sensors require further modifications before implementation into an animal cage. Adjustments recommended include:

- Eliminate drift of the baseline signal. In a laboratory animal cage, the ammonia and carbon dioxide concentrations are expected to gradually change over hours or days. Since the drift of the baseline and response to the gases were on the same order of magnitude, the signal drift may be mistaken for changes in ammonia or carbon dioxide.

- Increase sensitivity of the sensors. For example, the ammonia sensor's accuracy was not reliable until 200 ppm, which is not desirable for this application where the maximum ammonia concentration stated by the Guide (18) is 25 ppm.
- Amplify the signal, which would ensure that the magnitude of the signal is consistent and at a different level for each concentration.
- Couple each sensor with a humidity sensor. This coupling would allow for the gas sensor's response to adjust to changes in humidity. For example, if the sensor had a decrease in the work function signal, there should be a mechanism that would crosscheck with the humidity sensor to see if a change was registered there as well. If there was a response on the humidity sensor, then the sensor would output that no change was seen in the gas concentration.

Future Work

Further work with the field effect transistors includes:

- Implement the above sensor recommendations into the next generation ammonia and carbon dioxide sensors.
- Develop a theoretical model, similar to the ammonia model, for the carbon dioxide reaction on a surface that is selective to carbon dioxide such as barium carbonate (BaCO_3) or barium titanate (BaTiO_3). Additionally, more thorough single analyte, time-response, and cross-sensitivity experiments could be completed with the carbon dioxide sensor. Then the model could be compared with the limited experimental data completed in this project as well as with the more thorough experiments.
- Conduct single analyte experiments on the ammonia sensor at concentrations starting at 5 ppm and increasing until the sensing surface is saturated (the signal does not change with increasing ammonia concentration). From these experiments, two plots can be generated (1) $1/\Theta$ vs. $1/p_{\text{NH}_3}$ and (2) $1/\Theta$ vs. $1/p_{\text{NH}_3}^{1/2}$. If plot (1) is linear, then the reaction mechanism between ammonia and the titanium nitride surface can be ruled as molecular adsorption. If plot (2) is linear, then the mechanism could be ruled as ammonia dissociation.
- Apply numerical methods to solve the partial differential equations formulated for the diffusion flow regime.
- Examine the role of water on the sensitive layer of the sensor. Since the sensors will be used at room temperature with 40-70% relative humidity, it will be important to understand the water surface chemistry and investigate such items as whether the water adsorption follows a Langmuir model.
- Over a period of 2 days for static cages and 14 days ventilated cages analyze cage air samples for particulates. The particulate should be sized, counted, and

characterized (e.g., fibers and spores). With this information filters could be developed for protecting the sensors from contamination in a cage environment.

- Conduct a field study with the sensors in the laboratory rodent cages. The study would look at the optimal position in the cage for the sensors, evaluate the rodent's response and interaction with the sensors, and determine the overall performance of the sensor in the cage.

APPENDIX A
ENVIRONMENTAL STUDIES

Dependent Variable	Independent Variables												
	NH ₃	CO ₂	RH	Temp.	Cage ACPH	Room ACPH	Cage Air Velocity	Cage Type	Cage Population Size	Bedding Change Frequency	Bedding type	Mice (M), Rats (R)	Ref.
ACH								xx				M	(61)
ACH						xx						M	(31)
Airborne Allergens								xx			xx	M	(16)
Brain NH3					xx	xx			xx	xx		R	(25)
Breeding Performance					xx					xx		M	(35)
Physiological Changes	xx											R	(20)
CO2								xx	xx			M	(7)
CO2								xx				M	(34)
CO2											xx	M	(10)
CO2					xx					xx		M	(35)
CO2						xx						M	(31)
CO2						xx			xx	xx		M	(13)
CO2								xx				M	(62)
CO2								xx			xx	M	(63)
Differential pressure								xx				M	(34)
Dust content and Generation								xx				M	(17)
Dust content and Generation											xx	M	(21)
Histological Effects	xx											R	(24)
Histological Effects					xx					xx		M	(35)
Immune function					xx					xx		M	(35)
Light Intensity								xx				M	(61)
Microenv. Contaminants											xx	M	(10)

Dependent Variable	Independent Variables													Ref.
	NH ₃	CO ₂	RH	Temp.	Cage ACPH	Room ACPH	Cage Air Velocity	Cage Type	Cage Population Size	Bedding Change Frequency	Bedding type	Mice (M), Rats (R)		
Moisture Absorption											xx	M	(21)	
Moisture in Bedding					xx		xx					M,R	(64)	
NH3								xx	xx			M	(12)	
NH3								xx	xx			M	(7)	
NH3								xx				M	(17)	
NH3								xx				M	(34)	
NH3					xx	xx			xx	xx		R	(25)	
NH3			xx	xx					xx			R	(20)	
NH3											xx	M	(21)	
NH3											xx	M	(10)	
NH3					xx					xx		M	(35)	
NH3						xx						M	(31)	
NH3						xx			xx	xx		M	(13)	
NH3	xx										xx	R	(65)	
NH3								xx				M	(62)	
NH3								xx			xx	M	(63)	
NH3								xx				M	(66)	
NH3					xx		xx					M,R	(64)	
NH3						xx						M,R	(67)	
NH3 in different cages								xx	xx	xx		M	(68)	
NH3, CO2, Temp			xx										(63)	
NH3, CO2, Temp					xx(flow over cage)			xx				M	(69)	
NH3, Temp, RH								xx			xx	R	(70)	
Plasma cort.					xx					xx		M	(35)	

Dependent Variable	Independent Variables													Ref.
	NH ₃	CO ₂	RH	Temp.	Cage ACPH	Room ACPH	Cage Air Velocity	Cage Type	Cage Population Size	Bedding Change Frequency	Bedding type	Mice (M), Rats (R)		
Levels														
Preference					xx		xx						R (71)	
Rel. Hum.								xx	xx				M (12)	
Rel. Hum.								xx					M (17)	
Rel. Hum.								xx					M (61)	
Rel. Hum.											xx		M (10)	
Rel. Hum.					xx					xx			M (35)	
Rel. Hum.													M (30)	
Rel. Hum.									xx	xx			M (13)	
RH								xx					M (62)	
RH								xx			xx		M (63)	
Room ACH								xx					M (61)	
Sound levels								xx					M (61)	
Telemetry(heart rate)					xx		xx						R (71)	
Telemetry(heart rate)		xx											R (72)	
Temp								xx					M (17)	
Temp								xx					M (61)	
Temp											xx		M (10)	
Temp					xx					xx			M (35)	
Temp													M (13)	
Temp									xx	xx			M (13)	
Temp								xx			xx		M (63)	
Tracer Gas								xx					M (73)	
Weanling wt. And Growth					xx					xx			M (35)	

APPENDIX B
DETAILS OF FIELD EFFECT TRANSISTOR

While the primary focus of this study was the reaction between the analyte gas (ammonia or carbon dioxide) and the sensitive layer of the field effect transistor, it is important to provide additional details in schematic form (Figure B-1 and Figure B-2), photographs (Figure B-3 and Figure B-4), and electrical drawings (Figure B-5, Figure B-6, and Figure B-7).

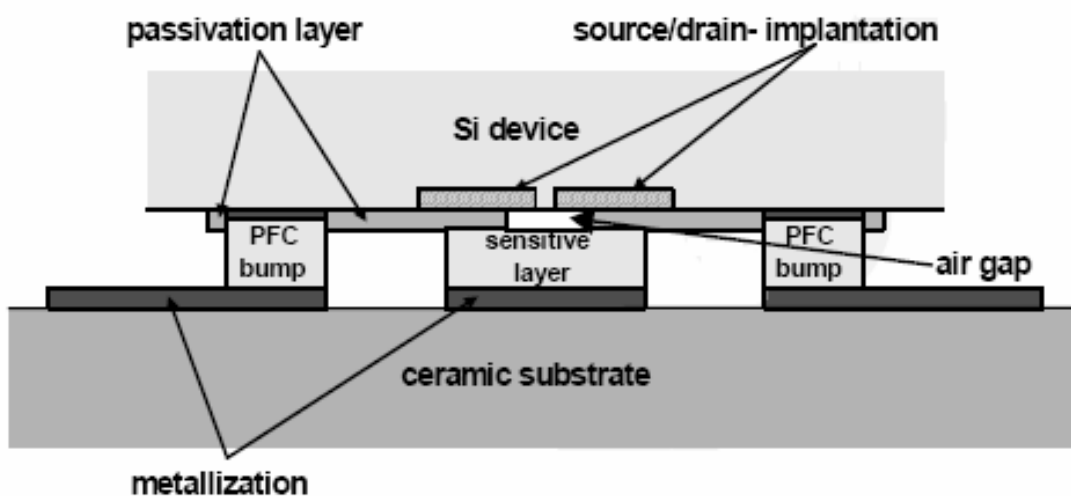


Figure B-1 Schematic section through a hybrid flip chip field effect transistor in a grossly enlarged vertical representation, where PFC indicates polymer flip chip and Si represents silicon. (Data of Pohle et al. (42).)

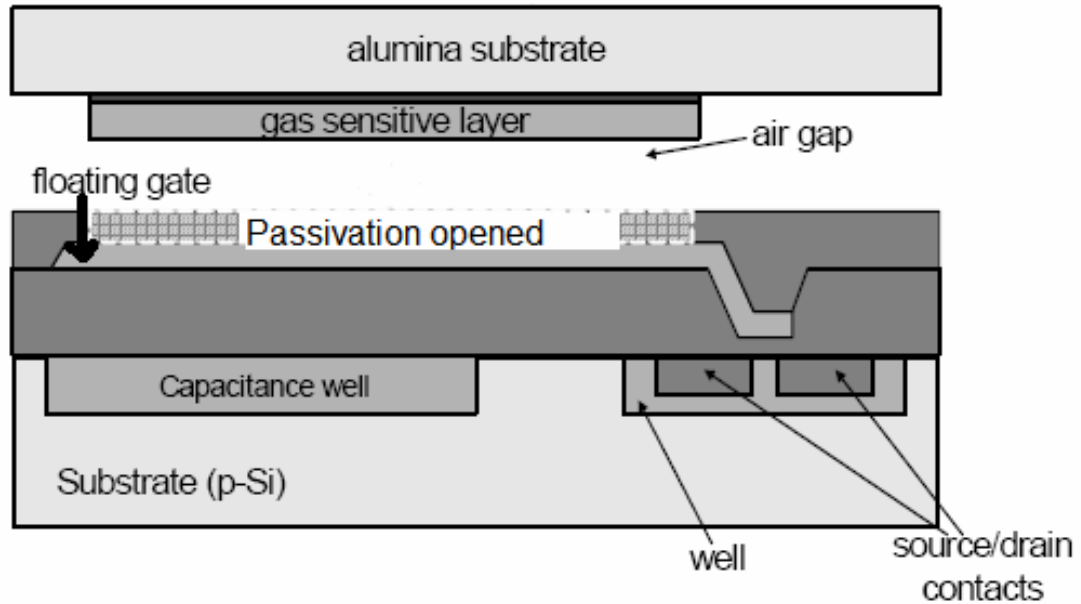


Figure B-2 Schematic cross-section of a suspended gate field effect transistor. (Data of Pohle et al. (42).)

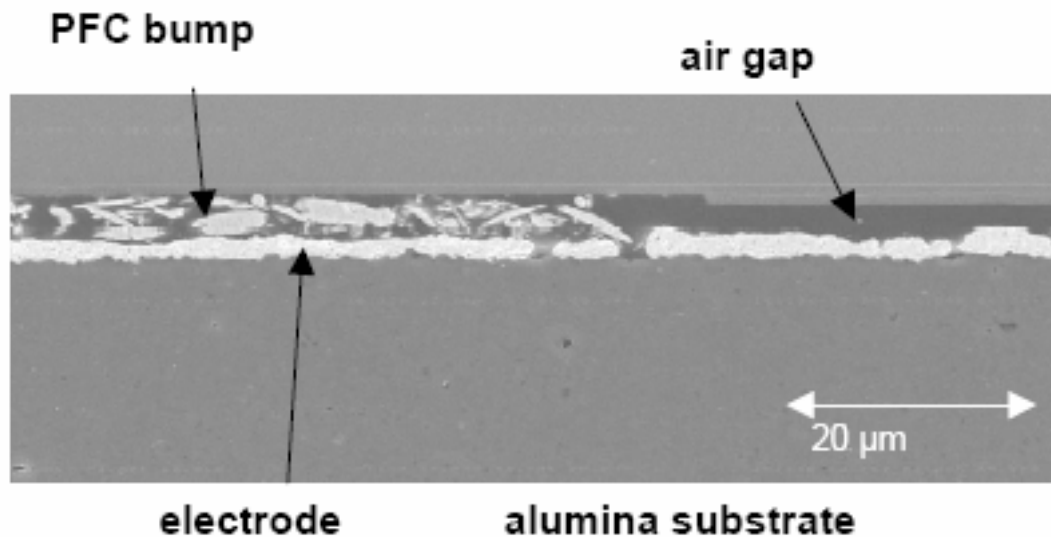


Figure B-3 Scanning electron microscope cross-section of a hybrid flip chip field effect transistor, where PFC indicates polymer flip chip. The air gap height is approximately 4 microns. (Data of Pohle et al. (42).)

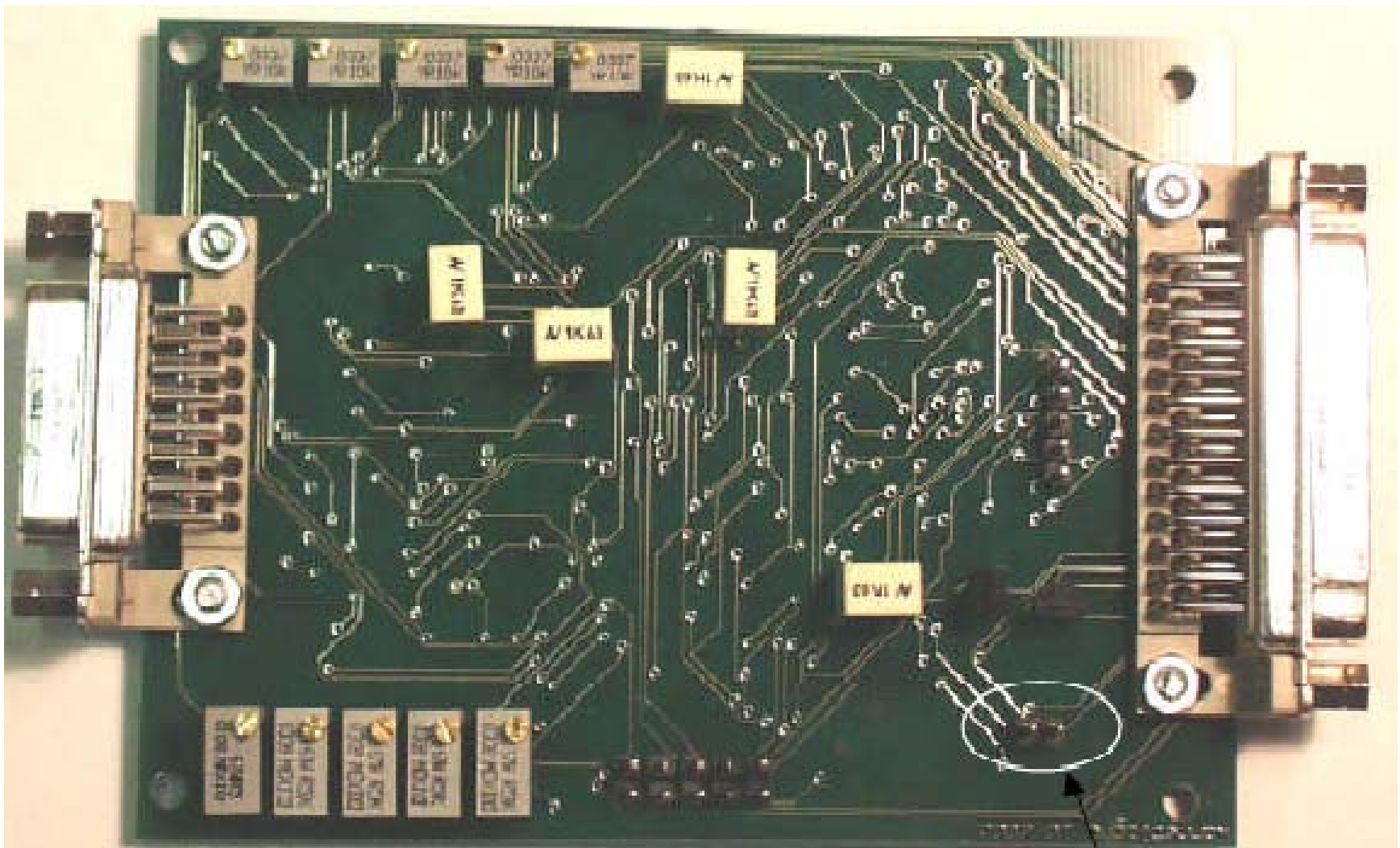


Figure B-4 Printed circuit board for the suspended gate field effect transistor.

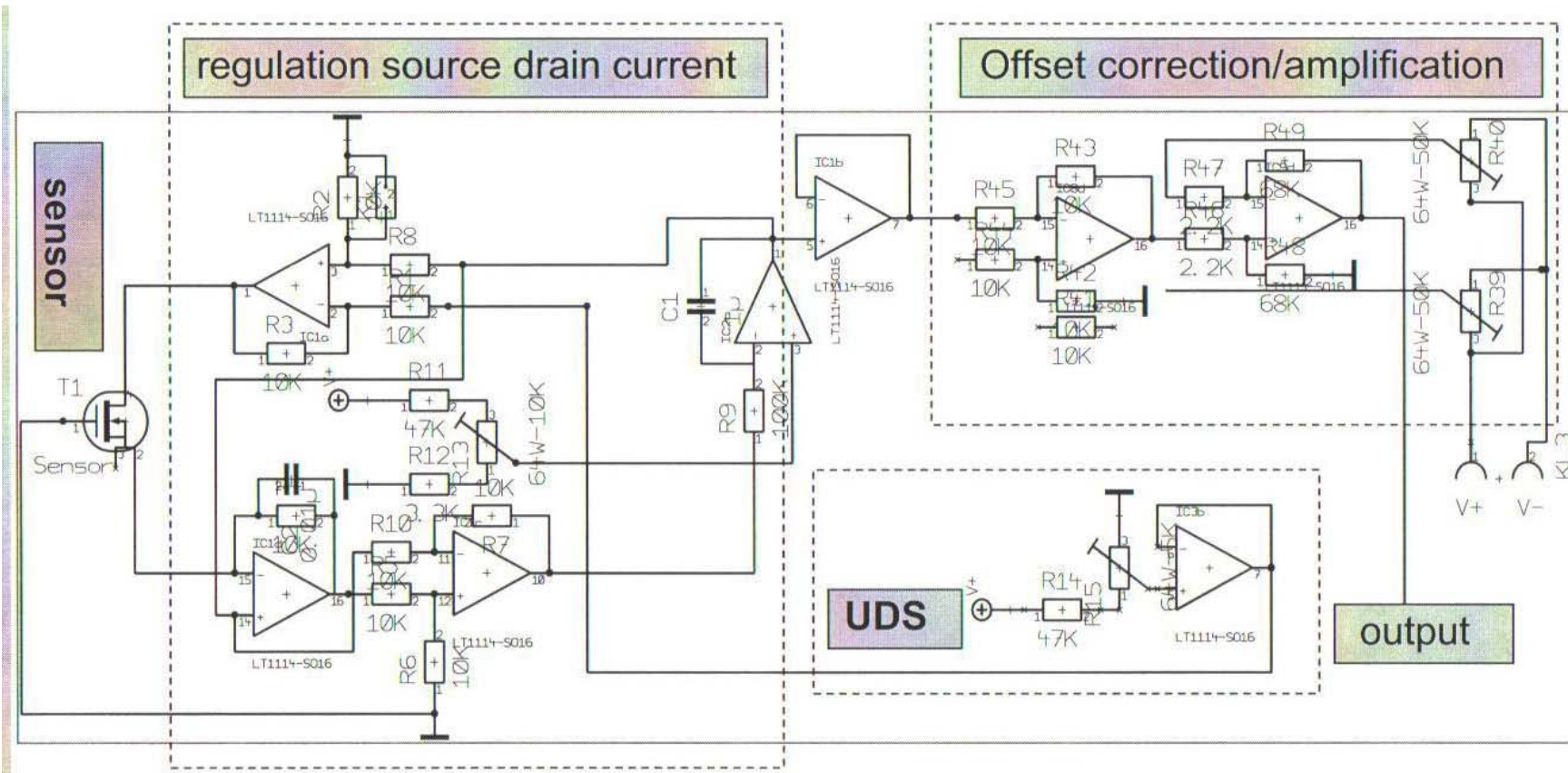


Figure B-5 Schematic for one channel of the suspended gate field effect transistor control board, where the drain to source voltage is indicated by UDS.

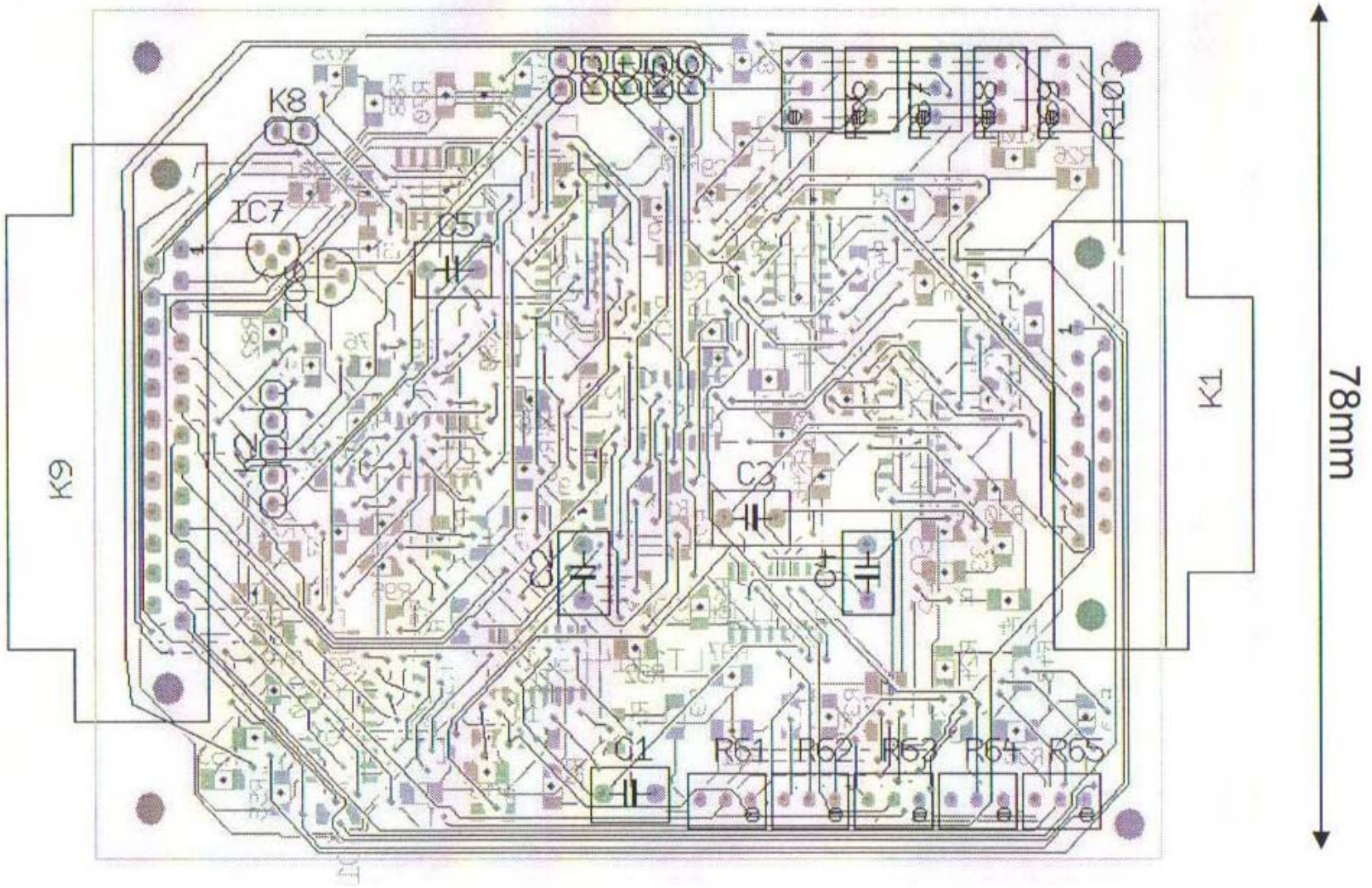


Figure B-6 Detailed drawing of the suspended gate field effect transistor control board.

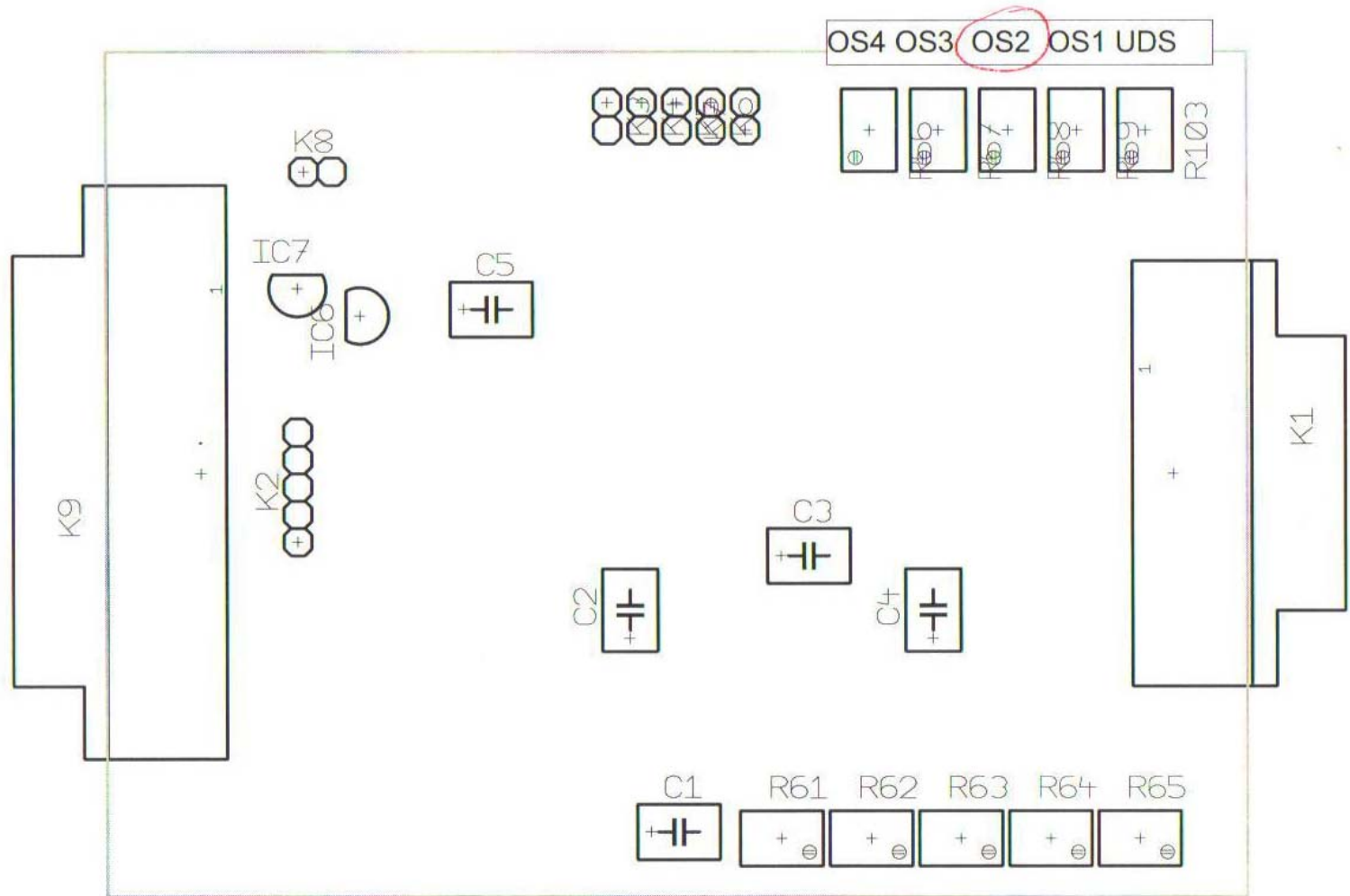


Figure B-7 Simple drawing of the suspended gate field effect transistor control board, where OS designates the potentiometers used to adjust the offset for the four channels and UDS indicates the drain source current, which can not be changed.

APPENDIX C
ANALYSIS OF EXPERIMENTAL UNCERTAINTY

The ammonia and carbon dioxide concentrations were determined by iteratively solving the following two equations,

$$[NH_3]_{out} = \frac{[NH_3]_{in} Q_{NH_3}}{Q_{air} + Q_{CO_2} + Q_{NH_3}} \quad (C.1)$$

and

$$[CO_2]_{out} = \frac{[CO_2]_{in} Q_{CO_2}}{Q_{air} + Q_{CO_2} + Q_{NH_3}}, \quad (C.2)$$

where Q_{NH_3} , Q_{CO_2} , and Q_{air} were the volumetric flow rates for ammonia, carbon dioxide, and air, respectively. $[CO_2]_{in}$ and $[NH_3]_{in}$ were the concentrations of the carbon dioxide and ammonia compressed gas cylinders, respectively. As an example, experimental uncertainties were analyzed for the experimental condition of 50 ppm ammonia, 3000 ppm carbon dioxide, and an air flow rate of 5 L/min. The first step was to estimate the uncertainty interval for each measured quantity. The accuracy specification for the flow controllers was $\pm 1\%$ of the full scale. The full scales for the ammonia, carbon dioxide, and air flow meters were 50 cc/min, 100 cc/min, and 5 L/min, respectively. The accuracy for the compressed gas cylinders was $\pm 2\%$ and $\pm 1.25\%$ for the ammonia and carbon dioxide cylinders, respectively. Therefore the error estimates for the measured flow rates were

$$Q_{NH_3} = 12.684 \pm 0.5 \text{ cc/min}$$

$$Q_{CO_2} = 60.729 \pm 1 \text{ cc/min}$$

$$\begin{aligned}
Q_{air} &= 5.000 \pm 0.05 \text{ L / min} \\
[NH_3]_{in} &= 20,000 \pm 400 \text{ ppm} \\
[CO_2]_{in} &= 250,000 \pm 12,500 \text{ ppm}
\end{aligned}$$

The relative uncertainties in measured quantities were

$$\begin{aligned}
u_{Q_{NH_3}} &= \pm \frac{0.5 \text{ cc / min}}{12.684 \text{ cc / min}} = \pm 0.0394 \\
u_{Q_{CO_2}} &= \pm \frac{1 \text{ cc / min}}{60.729 \text{ cc / min}} = \pm 0.0165 \\
u_{Q_{air}} &= \pm \frac{0.05 \text{ L / min}}{5.000 \text{ L / min}} = \pm 0.01 \\
[NH_3]_{in} &= \pm \frac{400 \text{ ppm}}{20,000 \text{ ppm}} = \pm 0.02 \\
[CO_2]_{in} &= \pm \frac{12,500 \text{ ppm}}{250,000 \text{ ppm}} = \pm 0.05
\end{aligned}$$

The uncertainty interval for the calculated ammonia concentration was determined from the following equation,

$$u_{[NH_3]_{out}} = \left[\left(\frac{Q_{NH_3}}{[NH_3]_{out}} \frac{\partial [NH_3]_{out}}{\partial Q_{NH_3}} u_{Q_{NH_3}} \right)^2 + \left(\frac{Q_{CO_2}}{[NH_3]_{out}} \frac{\partial [NH_3]_{out}}{\partial Q_{CO_2}} u_{Q_{CO_2}} \right)^2 + \left(\frac{Q_{air}}{[NH_3]_{out}} \frac{\partial [NH_3]_{out}}{\partial Q_{air}} u_{Q_{air}} \right)^2 + \left(\frac{[NH_3]_{in}}{[NH_3]_{out}} \frac{\partial [NH_3]_{out}}{\partial [NH_3]_{in}} u_{[NH_3]_{in}} \right)^2 \right]^{1/2} \quad (C.3)$$

The partial derivative terms were

$$\begin{aligned}
\frac{Q_{NH_3}}{[NH_3]_{out}} \frac{\partial [NH_3]_{out}}{\partial Q_{NH_3}} &= \frac{[NH_3]_{out}}{[NH_3]_{out}} \frac{Q_{air} + Q_{CO_2}}{Q_{air} + Q_{CO_2} + Q_{NH_3}} = 1 \\
\frac{Q_{CO_2}}{[NH_3]_{out}} \frac{\partial [NH_3]_{out}}{\partial Q_{CO_2}} &= -\frac{[NH_3]_{out}}{[NH_3]_{out}} \frac{Q_{CO_2}}{Q_{air} + Q_{CO_2} + Q_{NH_3}} = -0.01 \\
\frac{Q_{air}}{[NH_3]_{out}} \frac{\partial [NH_3]_{out}}{\partial Q_{air}} &= -\frac{[NH_3]_{out}}{[NH_3]_{out}} \frac{Q_{air}}{Q_{air} + Q_{CO_2} + Q_{NH_3}} = -1 \\
\frac{[NH_3]_{in}}{[NH_3]_{out}} \frac{\partial [NH_3]_{out}}{\partial [NH_3]_{in}} &= \frac{[NH_3]_{out}}{[NH_3]_{out}} = 1
\end{aligned} \quad (C.4)$$

Substituting into Eq. C.3 gave

$$u_{NH_3} = \left\{ \begin{aligned} & [(1)(0.0394)]^2 + [(-0.01)(0.0165)]^2 \\ & + [(-1)(\pm 0.01)]^2 + [(1)(\pm 0.02)]^2 \end{aligned} \right\}^{1/2} \quad (C.5)$$

$$u_{NH_3} = \pm 0.0452 \text{ or } 4.52\%$$

The uncertainty interval for the carbon dioxide concentration was determined in a similar fashion as the ammonia concentration. The uncertainty interval was calculated from

$$u_{[CO_2]_{out}} = \left[\begin{aligned} & \left(\frac{Q_{NH_3}}{[CO_2]_{out}} \frac{\partial [CO_2]_{out}}{\partial Q_{NH_3}} u_{Q_{NH_3}} \right)^2 + \left(\frac{Q_{CO_2}}{[CO_2]_{out}} \frac{\partial [CO_2]_{out}}{\partial Q_{CO_2}} u_{Q_{CO_2}} \right)^2 \\ & + \left(\frac{Q_{air}}{[CO_2]_{out}} \frac{\partial [CO_2]_{out}}{\partial Q_{air}} u_{Q_{air}} \right)^2 + \left(\frac{[CO_2]_{in}}{[CO_2]_{out}} \frac{\partial [CO_2]_{out}}{\partial [CO_2]_{in}} u_{[CO_2]_{in}} \right)^2 \end{aligned} \right]^{1/2}, \quad (C.6)$$

where the partial derivative terms were

$$\begin{aligned} \frac{Q_{NH_3}}{[CO_2]_{out}} \frac{\partial [CO_2]_{out}}{\partial Q_{NH_3}} &= -\frac{[CO_2]_{out}}{[CO_2]_{out}} \frac{Q_{NH_3}}{Q_{air} + Q_{CO_2} + Q_{NH_3}} = -0.003 \\ \frac{Q_{CO_2}}{[CO_2]_{out}} \frac{\partial [CO_2]_{out}}{\partial Q_{CO_2}} &= \frac{[CO_2]_{out}}{[CO_2]_{out}} \frac{Q_{air} + Q_{NH_3}}{Q_{air} + Q_{CO_2} + Q_{NH_3}} = 1 \\ \frac{Q_{air}}{[CO_2]_{out}} \frac{\partial [CO_2]_{out}}{\partial Q_{air}} &= -\frac{[CO_2]_{out}}{[CO_2]_{out}} \frac{Q_{air}}{Q_{air} + Q_{CO_2} + Q_{NH_3}} = -1 \\ \frac{[CO_2]_{in}}{[CO_2]_{out}} \frac{\partial [CO_2]_{out}}{\partial [CO_2]_{in}} &= \frac{[CO_2]_{out}}{[CO_2]_{out}} = 1 \end{aligned} \quad (C.7)$$

Substituting into Eq. C.6 gave

$$u_{CO_2} = \left\{ \begin{aligned} & [(-0.003)(\pm 0.0394)]^2 + [(1)(\pm 0.0165)]^2 \\ & + [(-1)(\pm 0.01)]^2 + [(1)(\pm 0.05)]^2 \end{aligned} \right\}^{1/2} \quad (C.8)$$

$$u_{CO_2} = \pm 0.0535 \text{ or } 5.35\%$$

For this example, the ammonia and carbon dioxide concentrations fell between the interval 47.75 – 52.25 ppm and 2840 – 3160 ppm, respectively.

LIST OF REFERENCES

1. Americans for Medical Progress. Medical Milestones. *Animal Research*. www.amprogress.org/Issues/IssuesList.cfm?c=10. (July 2005).
2. University of California Center for Animal Alternatives. The mouse in science. *Cancer Research*. www.vetmed.ucdavis.edu/Animal_Alternatives/cancer.htm. (May 2004).
3. Lam, M. Mice research useful for vitamin C update. *News and Views*. www.drlam.com/news_and_views/MiceResearchUsefulforVitaminCUpdate.cfm (July 2005).
4. The Jackson Laboratory. Research areas. *Research*. www.jax.org/research/research_areas.html. (July 2005).
5. Novak, G. & Sharpless, L. What's best for the mouse's house: selecting an individually ventilated caging system caging system. *Lab Anim. (NY)* **32(7)**, 41-47 (2003).
6. Lipman, N. Isolator rodent caging systems: a critical view. *Contemp. Top. Lab. Anim. Sci.* **38(5)**, 9-17 (1999).
7. Serrano, L. Carbon dioxide and ammonia in mouse cages. *Lab. Anim. Sci.* **21(1)**, 75-85 (1971).
8. Schulhof, J. Keeping clean with filter top and ventilated cages. *Lab Anim. (NY)* **19(1)**, 31-35 (1990).
9. Huerkamp, M. & Lehner, N. Comparative effects of forced-air, individual cage ventilation or an absorbent bedding additive on mouse isolator cage environment. *Contemp. Top. Lab. Anim. Sci.* **33(2)**, 58-61 (1994).
10. Perkins, S. & Lipman, N. Characterization and quantification of microenvironmental contaminants in isolator cages with a variety of contact bedding. *Contemp. Top. Lab. Anim. Sci.* **34(3)**, 93-97 (1995).
11. Lipman, N. Microenvironmental conditions in isolator cages: an important research variable. *Lab Anim. (NY)* **21(6)**, 23-27 (1992).

12. Choi, G., McQuinn, J., Jennings, B., Hassett, D. & Michaels, S. Effect of population size on humidity and ammonia levels in individually ventilated microisolation rodent caging. *Contemp. Top. Lab. Anim. Sci.* **33(6)**, 77-81 (1994).
13. Reeb, C., Jones, R., Bearg, D., Bedigian, H., Myers, D., & Paigen, B. Microenvironment in ventilated animal cages with differing ventilation rates, mice populations, and frequency of bedding changes. *Contemp. Top. Lab. Anim. Sci.* **37(2)**, 43-49 (1998).
14. Gordon, S., Fisher, S., & Ronald, R. Elimination of mouse allergens in the working environment: assessment of individually ventilated cage systems and ventilated cabinets in the containment of mouse allergens. *J. Allergy Clin. Immunol.* **108(2)**, 288-294 (2001).
15. Sharp, P. & LaRegina, M. *The Lab Rat*. (CRC Press, Boca Raton, 1998).
16. Sakaguchi, M., Inouye, S., Miyazawa, H., Kamimura, H., Kimura, M., & Yamazaki, S. Evaluation of countermeasures for reduction of mouse airborne allergens. *Lab. Anim. Sci.* **40(6)**, 613-615 (1990).
17. Murakami, H. Differences between internal and external environments of the mouse cage. *Lab. Anim. Sci.* **21(5)**, 680-684 (1971).
18. National Research Council. *Guide for the Care and Use of Laboratory Animals*. (National Academy Press, Washington, D.C., 1996).
19. Keller, L., White, W., Snider, M., & Lang, C. An evaluation of intracage ventilation in three animal caging systems. *Lab. Anim. Sci.* **39(3)**, 237-242 (1989).
20. Gamble, M. & Clough, G. Ammonia build-up in animal boxes and its effect on rat tracheal epithelium. *Lab. Anim.* **10**, 93-104, (1976).
21. Potgieter, F. & Wilke, P. The dust content, dust generation, ammonia production, and absorption properties of three different rodent bedding types. *Lab. Anim.* **30**, 79-87, (1996).
22. National Institute of Occupational Health and Safety. *Occupational Health Guideline for Ammonia*. 92-110, (1992).
23. Coon, R., Jones, R., Jenkins, L., & Siegel, J. Animal inhalation studies on ammonia, ethylene glycol, formaldehyde, dimethylamine, and ethanol. *Toxicol. Appl. Pharmacol.* **16(3)**, 646-655 (1970).
24. Broderson, J., Lindsey, J. & Crawford, J. The role of environmental ammonia in respiratory mycoplasmosis of rats. *Am. J. Pathol.* **85(1)**, 115-127 (1976).

25. White, W. & Mans, A. Effect of bedding changes and room ventilation rates on blood and brain ammonia levels in normal rats and rats with portacaval shunts. *Lab. Anim. Sci.* **34(1)**, 49-52, (1984).
26. Krohn, T. & Hansen, A. Carbon dioxide concentrations in unventilated IVC cages. *Lab. Anim.* **36**, 209-212, (2002). Krohn, T. & Hansen, A. Carbon dioxide concentrations in unventilated IVC cages. *Lab. Anim.* **36**, 209-212, (2002).
27. Krohn, T. & Hansen, A. The effects of and tolerances for carbon dioxide in relation to recent developments in laboratory animal housing. *Scand. J. Lab. Anim. Sci.* **27**, 173-181, (2000).
28. National Institute of Occupational Health and Safety. *Occupational Health Guideline for Acetic Acid*. 92-110, (1992).
29. National Institute of Occupational Health and Safety. *Occupational Health Guideline for Sulfur Dioxide*. 92-110, (1992).
30. Lipman, N. & Perkins, S. Macroenvironmental relative humidity and bedding in isolator cages. *Contemp. Top. Lab. Anim. Sci.* **39(6)**, 7 (2000).
31. Reeb, C., Jones, R., Bearg, D., Bedigian, H., & Paigen, B. Impact of room ventilation rates on mouse cage ventilation and microenvironment. *Contemp. Top. Lab. Anim. Sci.* **36(1)**, 74-79 (1997).
32. Besch, E. Environmental quality within animal facilities. *Lab. Anim. Sci.* **30**, 385-398, (1980).
33. Hasenau, J., Baggs, R. & Kraus, A. Microenvironments in microisolation cages using BALB/c and CD-1 mice. *Contemp. Top. Lab. Anim. Sci.* **32(1)**, 11-16 (1993).
34. Høglund, A. & Renström, A. Evaluation of individually ventilated cages for lab rodents. *Lab. Anim.* **35**, 51-57, (2001).
35. Reeb-Whitaker, C., Paigen, B., Beamer, W., Bronson, R., Churchill, G., Schweitzer, I., & Myers, D. Impact of reduced frequency of cage changes on the health of mice housed in ventilated cages. *Lab. Anim.* **35**, 58-73, (2001).
36. Agrawal, R. A model for minimizing cost for housing laboratory mice. Master's Thesis. University of Florida. 2003.
37. Oxner, E. *FET Technology and Application*. (Marcel Dekker Inc., New York, 1989).
38. Askeland, D. *The Science and Engineering of Materials*. (PWS Publishing Company, Boston, 1994).

39. Rizzoni, G. *Principles and Applications of Electrical Engineering*. (McGraw Hill, Boston, 2000).
40. Lesurf, J. Field effect transistor. *The First Eleven*. University of St. Andrews. 22 April 2004, www.st-andrews.ac.uk/~www_pa/Scots_Guide/first11/part7/page1.html.
41. Fleischer, M., Ostrick, B., Pohle, R., Simon, E., Meixner, H., Bilger, C., & Daeche, F. Low-power gas sensors based on work-function measurement in low-cost hybrid flip chip technology. *Sens. Actuators B Chem.* **80**, 169-173, (2001).
42. Pohle, R., Simon, E., Schneider, R., Fleischer, M. & Meixner, H. Improved CCFET and SGFET type gas sensors in hybrid flip chip technology: realization and characterization of a new sensor concept. Not yet published.
43. Abom, E., Hultman, L., Eriksson, M., & Tweston, R. Properties of combined TiN and Pt thin films applied to gas sensing. *J. Vac. Sci. Technol. A.* **20(3)**, 667-673, (2002).
44. Ostrick, B., Pohle, R., Fleischer, M., & Meixner, H. TiN in work function type sensors: a stable ammonia sensitive material for room temperature operation with low humidity cross sensitivity. *Sens. Actuators B Chem.* **68**, 234-239, (2000).
45. Ostrick, B., Fleischer, M., Meixner, H., & Kohl, C. Investigation of the reaction mechanisms in work function type sensors at room temperature by studies of the cross-sensitivity to oxygen and water: the carbon-carbon dioxide system. *Euroensors XIII*. 81-84, (1999).
46. Simon, E., Lampe, U., Pohle, R., Fleischer, M., Meixner, H., Frerichs, H.-P., & Lehmann, M. Novel carbon dioxide gas sensors based on field effect transistors. Not yet published.
47. Ostrick, B., Fleischer, M., & Meixner, H. The influence of interfaces and interlayers on the gas sensitivity in work function type sensors. *Sens. Actuators B Chem.* **95**, 271-274, (2003).
48. Atkins, P. *Physical Chemistry*. (W.H. Freeman and Company, New York, 1995).
49. Takagi-Kawai, M., Soma, M., Onishi, T., & Tamaru, K. The adsorption and the reaction of NH₃ and NO_x on supported V₂O₅ catalysts: effect of supporting materials. *Can. J. Chem.* **58(20)**, 2132-2137 (1980).
50. Shimanouchi, T. *Tables of Molecular Vibrational Frequencies*. (National Bureau of Standards, Washington, D.C., 1972).
51. Hlil, E., Kubler, L., Bischoff, J., & Bolmont, D. Photoemission study of ammonia dissociation on Si(100) below 700 K. *Phys. Rev. B., Condens. Matter.* **35(11)**, 5913-5916, (1987).

52. Bozso, F. & Avouris, P. Photoemission studies of the reactions of ammonia and N atoms with Si(100)-(2x1) and Si(111)-(7x7) surfaces. *Phys. Rev. B., Condens. Matter.* **38(6)**, 3937-3942, (1988).
53. Bischoff, J., Lutz, F., Bolmont, D. & Kubler, L. Use of multilayer techniques for XPS identification of various nitrogen environments in the Si/NH₃ system. *Surface Science.* **251/252**, 170-174, (1991).
54. Zhou, X., Flores, C., & White, J. Decomposition of NH₃ on Si(100): a SSIMS study. *Surface Science Letters.* **268**, L267-273, (1992).
55. Chen, P., Colaianni, M., & Yates, J. Silicon backbond strain effects on NH₃ surface chemistry: Si(111)-(7x7) compared to Si(100)-(2x1). *Surface Science Letters.* **274**, L605-610, (1992).
56. Siew, H., Qiao, M., Chew, C., Mok, K., Chan, L., & Xu, G. Adsorption and reaction of NH₃ on Ti/Si(100). *Applied Surface Science.* **173**, 95-102, (2001).
57. Laksono, E., Galtayries, A., Argile, C., & Marcus, P. Adsorption of NH₃ on oxygen pre-treated Ni(111). *Surface Science.* **530**, 37-54, (2003).
58. Diebold, U. & Madey, T. Adsorption and electron stimulated desorption of NH₃/TiO₂(110). *J. Vac. Sci. Technol. A.* **10(4)**, 2327-2335, (1992).
59. Karthigeyan, A., Gupta, R., Scharnagl, K., Burgmair, M., Sharma, S., & Eisele, I. A room temperature HSGFET ammonia sensor based on iridium oxide thin film. *Sens. Actuators B Chem.* **85**, 145-153, (2002).
60. Mhadeshwar, A., Wang, H., & Vlachos, D. Thermodynamic consistency in microkinetic development of surface reaction mechanisms. *J. Phys. Chem. B.* **107**, 12721 – 12733, (2003).
61. Clough, G., Wallace, J., Gamble, M., Merryweather, E., & Bailey, E. A positive, individually ventilated caging system: a local barrier system to protect both animals and personnel. *Lab. Anim.* **29**, 139-151, (1995).
62. Lipman, N, Corning, B., & Coiro, M. The effects of intracage ventilation on microenvironmental conditions in filter-top cages. *Lab. Anim.* **26**, 206-210, (1992).
63. Corning, B. & Lipman, N. A comparison of rodent caging systems based on microenvironmental parameters. *Lab. Anim. Sci.* **41**, 498-503, (1991).
64. Wu, D, Joiner, G., & McFarland, A. A forced-air ventilation system for rodent cages. *Lab. Anim. Sci.* **35**, 499-504, (1985).

65. Ishii, T., Yoshida, K., Hasegawa, M., Mizuno, S., Okamoto, M., Tajima, M., & Kurosawa, T. Invention of a forced-air-ventilated micro-isolation cage and rack system. Environment within cages: temperature and ammonia concentration. *Appl. Anim. Behav. Sci.* **59**, 115-123 (1998).
66. Keller, G., Mattingly, S., & Knapke, F. A forced-air individually ventilated caging system for rodents. *Lab. Anim. Sci.* **33**, 580-582, (1983).
67. Weissman, S., Beethe, R., & Redman, H. Ammonia concentrations in an animal inhalation exposure chamber. *Lab. Anim. Sci.* **30**, 974-980, (1980).
68. Eveleigh, J. Murine cage density: cage ammonia levels during the reproductive performance of an inbred strain and two outbred stocks of monogamous breeding pairs of mice. *Lab. Anim.* **27**, 156-160, (1993).
69. Corning, B., & Lipman, N. The effects of a mass air displacement unit on the microenvironmental parameters within isolator cages. *Lab. Anim. Sci.* **42**, 91-93, (1992).
70. Hirsjarvi, P. & Valiaho, T. Microclimate in two types of rat cages. *Lab. Anim.* **21**, 95-98, (1987).
71. Krohn, T., Hansen, A., & Dragsted, N. The impact of cage ventilation on rats housed in IVC systems. *Lab. Anim.* **37**, 85-93, (2003).
72. Krohn, T., Hansen, A., & Dragsted, N. The impact of low levels of carbon dioxide on rats. *Lab. Anim.* **37**, 94-99, (2003).
73. Keller, L., White, W., Snider, M., & Lang, C. An evaluation of intra-cage ventilation in 3 animal caging systems. *Lab. Anim. Sci.* **39**, 237-241, (1989).

BIOGRAPHICAL SKETCH

Karen (Timm) Supan grew up in Stoughton, Wisconsin. She received her bachelor's degree in mechanical engineering from Minnesota State University, Mankato, in May 2000. A summer internship with the Institute of Paper Science and Technology in Atlanta, Georgia, while still an undergraduate led her to pursue a master's degree in pulp and paper science. She completed her master's degree in 2002 and returned to mechanical engineering by entering the doctorate program at the University of Florida. Karen and her husband, Brian, were married in 2002 and currently reside in Tampa, Florida.